Unburned Hydrogen Emissions of a Hydrogen-Diesel Dual Fuel Engine

by

Edward Werner Sperling

A thesis submitted in partial fulfillment of the requirements for the degree of

Master of Science

Department of Mechanical Engineering
University of Alberta

Abstract

Despite increasing pressure from other energy conversion systems, the internal combustion engine is likely to remain dominant in the transportation sector. Hydrogen has long been considered as a zero-carbon motor fuel, and has the potential to become a front runner. Hydrogen-Diesel Dual-fuel (HDDF) operation with port-injected hydrogen is an attractive option during a time of transition, allowing practical retrofits and the option of switching between diesel and hydrogen according to supply constraints. However, global warming potential of unburned hydrogen emissions (H_2 slip) has been reported at a factor of 11.6 times CO_2 on a mass basis. Understanding and controlling port-injected HDDF engine operation as it pertains to a retrofit production diesel, with the aim of reducing carbon dioxide and unburned hydrogen emissions, is the focus of this thesis.

To measure hydrogen emissions in engine exhaust, an inexpensive sensor operating on the catalytic combustion principle is tested for cross-sensitivities using a high-accuracy flow bench. A minimum oxygen content of 8 vol% is required to measure hydrogen up to 4 vol%. Cross-sensitivity to carbon monoxide is found at 0.392 H_2%/CO% and the engine results corrected for this effect. A sensor deadband is found where results under 0.047 H_2% are rounded to zero. Above this level, and after correction for carbon monoxide, measurements of real exhaust match gas chromatography to 0.02% and the sensor is deemed suitable for the present work.

A port-injected retrofit HDDF engine was operated in naturally-aspirated condition. Emissions of unburned hydrogen were strongly dependent on volume fraction of hydrogen fuel in intake air (H2int). As H2int is increased, unburned hydrogen emissions increase and peak near H2int=3–5%. Diesel Start of Injection (SOI) has a significant effect from H2int=2–7% and less effect with higher H2int. Maximum Pressure Rise Rate (MPRR) is strongly dependent on SOI, peaking near SOI=-14 Crank Angle Degrees (CAD). Constant loads of 3, 4, and 6 bar Indicated Mean Effective Pressure (IMEP) were tested at varying Hydrogen Energy Share (HES) from 41–87%. Increasing HES monotonically decreased total CO_2 equivalent emissions, both through decreasing unburned H_2 emissions and decreasing diesel use and asscociated CO_2 emissions. SOI had the largest effect at IMEP=3 bar, and unburned hydrogen contributed up to 38% of total CO_2 equivalent emissions. Maximizing HES through use of minimum DOI at IMEP 2, 3, 4, and 6 bar found that unburned hydrogen is strongly dependent on H2int (and therefore load) and also dependent on SOI. MPRR was strongly dependent on SOI and weakly dependent on load.

Heat release curves are calculated at several operating points covering loads of 2, 3, 4, and 6 bar IMEP. For SOI near Top-Dead-Centre (TDC) and operation at 2, 3, and 4 bar IMEP the combustion is found to progress in five stages. For higher loads and/or earlier injection timing, the stages combine together.

At all tested constant-load and varying-HES points, maximizing Hydrogen Energy Share minimized unburned hydrogen emissions, minimized CO_2 equivalent emissions, and reduced MPRR.

Preface

This thesis is an original work by Edward Sperling. This work was performed at the University of Alberta campus Engine Lab in Edmonton, Alberta. Funding has been provided by Future Energy Systems research grant from the Canada First Research Excellence Fund.

Some parts of this thesis have been previously published in conference proceedings.

- *Edward Sperling, Hossein Mehnatkesh, Javad Kheyrollahi, Charles Robert Koch and David Gordon, "Hydrogen Slip Measurement in a Hydrogen Diesel Dual-Fuel Engine", Proceedings of Combustion Institute - Canadian Section, May 2024*
- *Ed Sperling, David Gordon, and C. R. Koch, "Low-Cost Commercial Sensor for Measuring Unburned Hydrogen in Engine Exhaust", Proceedings of the Canadian Society for Mechanical Engineering International Congress, May 2025*
- *Ed Sperling, David Gordon, and C. R. Koch, "Heat Release Characteristics of a Hydrogen-Diesel Dual Fuel Engine for varied hydrogen energy and pilot diesel injection timing", Proceedings of the Canadian Society for Mechanical Engineering International Congress, May 2025*

Acknowledgements

A great thanks to my supervisor Bob Koch, without whom I would have never made the jump to grad studies, who made many suggestions to this work, and professor David Gordon, whose knowledge and energy were essential to this success.

To my parents and siblings, who were always a sympathetic ear to lean on.

To the past and present members of the lab, Jakub whose work this builds on, Hossein for informative conversations on machine learning, and many others who have shared this journey.

Table of Contents

List of Tables

List of Figures

List of Symbols

Variables

$\Delta\mathrm{X}$	Change in X
η_{H2}	Hydrogen Combustion Efficiency
η_{th}	Thermal Efficiency
η_{v}	Volumetric Efficiency
γ	Specific Heat ratio
ω	Engine speed
ϕ	Fuel Equivalence Ratio relative to a stoichiometric mixture
dQ	Rate of heat release
dQ_{AHR}	Apparent Heat Release rate, not including wall loss
dQ_{w}	Rate of heat loss to cylinder walls
E	Energy
M	Molecular Weight
n	Number of mols
Q	Heat released
R	Ideal gas constant
T	Temperature
t	Time
V	Instantaneous Cylinder Volume
V_{d}	Displacement Volume of one cylinder
W	Work
CA10	Crank angle at which 10% of fuel has burned, taken as onset of combustion
CA50	Crank angle at which 50% of fuel has burned

CA90	Crank angle at which 90% of fuel has burned, taken as end of combustion
H2exh	Volume fraction of hydrogen in exhaust gas air, $\frac{V_{\mathrm{H2}}}{V_{\mathrm{Total}}}$
H2int	Volume fraction of hydrogen in intake air, $\frac{V_{\mathrm{H2}}}{V_{\mathrm{H2}}+V_{\mathrm{Air}}}$

Subscripts

evap	evaporative
exh	exhaust
int	intake

Superscripts

$\dot{\mathrm{X}}$	Derrivative of X with respect to time
$\overline{\mathrm{X}}$	Normalized value of X

Abbreviations

AHR Apparent Heat Release.

aTDC After Top Dead Center.

bTDC Before Top Dead Center.

CAD Crank Angle Degree.

CR Compression Ratio.

DAQ Data Acquisition.

DI Direct Injection.

DOI Duration of Injection.

ECU Engine Control Unit.

EVO Exhaust Valve Opening.

FEP Fluoridated Ethylene Propylene plastic.

FET Field Effect Transistor.

FMEP Frictional Mean Effective Pressure.

GHG Greenhouse Gas.

H2exh Exhaust Hydrogen.

H2int Intake Hydrogen.

HDDF Hydrogen-Diesel Dual-Fuel.

HES Hydrogen Energy Share.

ICE Internal Combustion Engine.

IMEP Indicated Mean Effective Pressure.

IVC Intake Valve Closing.

LHV Lower Heating Value.

MABX Micro AutoBox controller.

MPRR Maximum Pressure Rise Rate.

PC Personal Computer.

PID Proportional-Integral-Derivative.

PTFE Poly Tetra Fluoro Ethylene (Teflon$^{\circledR}$).

RC Resistor-Capacitor.

RMS Root-Mean-Square.

SCCM Standard Cubic Centimetres per Minute.

SI Spark Ignition.

SOI Start of Injection.

TDC Top Dead Center.

Chapter 1

Introduction

1.1 Introduction

In the search to reduce worldwide greenhouse gas emissions, alternative carbon-free methods of powering economies and industries are being sought in jurisdictions including Canada [1], USA [2] and the European Union [3]. While advances have been made in battery-electric and fuel cell technology, challenges remain [4, 5]. Internal Combustion Engines (ICEs) running on a chemical fuel are likely to remain dominant in the transportation industry [6]. In this role, the role of the chemical fuel can be considered as mainly a source of energy (biofuels and hydrogen produced from fossil fuels) or an energy carrier for other sources (E-fuels or hydrogen created using renewable sources). Currently, hydrogen is considered as a likely front-runner zero-carbon fuel for transportation applications [7].

Since the early days of internal combustion engines, hydrogen has been considered as a motor fuel. Examples include the DeRevaz engine [8] from 1804. Many early engines ran on coalgas or watergas [9], which contains hydrogen and carbon monoxide produced from coal. Today watergas would be termed syngas, and in a modern context much is produced from methane [10]. Hydrogen fuel has recently seen a revival of interest as a way to reduce carbon dioxide emissions [7]. The energy in the fuel can come from several sources. One potential energy source is conventional fossil fuels, including already developed natural gas wells. Using several methods, the carbon would be stripped from these fuels and sequestered as carbon black or as carbon dioxide, with the product often termed Blue Hydrogen [10]. Intermittent sources of power (wind, solar) can also be used to manufacture hydrogen via electrolysis, which is then stored. The resulting fuel can be used to support the electrical grid during high demand times or would be available for other uses including motor fuel. Hydrogen produced by renewable energy is often termed Green Hydrogen [11]. Other sources of electrical energy such as nuclear (Purple Hydrogen) can be used. Again hydrogen fuel can be produced during off-peak hours and stored until use. Geological sources of hydrogen (White Hydrogen) have also been found. These sources were often ignored in the past due to difficulty in detecting and quantifying the hydrogen content and low demand for the product [12]. Deposits were also found, sometimes as a hazard, during other activities such as water well drilling [12, 13] or mining [12]. Currently exploration is underway for geological sources of hydrogen [14].

1.2 Hydrogen Usage in Reciprocating Engines

Within a reciprocating, cyclic internal combustion engine the hydrogen fuel must ignite at the right time. Several methods have been explored in the literature.

1.2.1 Hydrogen as the Sole Fuel

Much work has used spark-ignition, either with port-fuel injection [15, 16] or direct-injection [17, 18]. This is an area of active research, but not the focus of the present thesis.

For an HCCI engine operated on a blend of n-heptane and iso-octane, intake air temperature was important in reducing cyclic variation, with hotter intake temperatures reducing variation [19, 20]. A more fuel-rich mixture likewise reduced combustion variability [19, 20]. For hydrogen, a numerical study determined that free-piston HCCI operation should be possible at an intake temperature of 27 °C [21]. An engine with a 20:1 compression ratio was operated in HCCI mode using hydrogen at equivalence ratios of 0.15 and 0.37, with intake air heated to 80 °C or 100 °C [22]. Minimum intake air temperature for hydrogen was found to depend on both fuel ratio and compression ratio [23]. Another numerical study simulated HCCI operation at 20:1 compression ratio and determined that intake air heating was dominant in controlling ignition in the case of hydrogen fuel, and more significant than equivalence ratio [24]. Temperature inhomogeneities were also found to be significant to the combustion. Using direct-injected hydrogen and a compression ratio of 29:1, ignition was only achieved using external means [18]. The authors of that study hypothesize that in other studies where auto-ignition was reported at lower compression ratios (such as 18.6), the ignition was due to cylinder hot spots.

The autoignition characteristics of hydrogen jets has also been studied [25]. Below 1100K the autoignition delay could be predicted using the Arrhenius equation, and near 1100K the ignition delay was similar to conventional diesel fuels [25]. Using intake air heating to a minimum of 80 °C, a 17:1 compression ratio engine was run with direct-injected auto-ignited hydrogen [26].

Hydrogen ignition via glow-plug in the fuel jet has also been demonstrated [18]. A vehicle has been demonstrated, using a direct-injection 2-stroke hydrogen engine where a hot platinum wire acted as a glowplug [27].

1.2.2 Hydrogen-Diesel Dual Fuel

Dual-fuel operation, where the autoignition of an injected high-reactivity fuel (such as diesel) is used to ignite a lower-reactivity hydrogen fuel (such as hydrogen), is another area of active research. Hydrogen can be injected into the intake air, where it mixes and forms a homogeneous mixture ignited by a diesel pilot injection (for example, Port-Fuel Injection). Stratified charge [28] and direct-injection techniques [29] can also be used to modify burn rate of the charge. This can be extended to the use of crossed-jet injectors [30]. Injection of hydrogen as a cryogenic liquid has also been considered [27, 31]. At 1600 bar, fast cryogenic liquid injector response gives the potential to shape the heat release profiles though multiple injections [31].

Port-injected dual fuel mode is attractive for the current transportation industry. This technology can be retrofit to existing diesel vehicles [32]. With over 1.2 million medium and heavy-duty trucks in Canada in 2022 [33], replacing every truck engine would incur large economic cost. When retrofitting an existing production diesel, adding a second direct injector for hydrogen to the cylinder head can have challenges, making port-fuel injection more attractive [34]. Using port-fuel injection (rather than dual or coaxial injectors [35–37]) means that the stock injectors can be kept in place, which allows easily switching back to diesel-only operation at any time. With limited availability of hydrogen fueling infrastructure (but ubiquitous diesel service stations), this can be expected to reduce range anxiety and improve market uptake, providing a market for hydrogen fueling infrastructure. Understanding and controlling dual-fuel engine operation as it pertains to a production diesel retrofit with hydrogen port-fuel injectors, with an aim of maximizing hydrogen energy utilization and reducing unburned hydrogen emissions, is the focus of this thesis. Additionally, to achieve this goal, an inexpensive hydrogen sensor is quantified for service in measuring exhaust gas from these engines.

1.3 Dual-Fuel Hydrogen

Many works have studied the effects of co-combusting hydrogen in diesel engines. Common operational concerns are high pressure rise rate and pre-ignition.

Using a stock controller and diesel injection timing, then adding hydrogen fuel premixed in intake air, is a method used by several studies. One such study found improvements in efficiency due to advanced combustion phasing in high power operation [38]. Hydrogen addition can increase NO_x and can markedly decrease soot and

CO [39], however it is possible to increase soot from diesel via displacement of air by hydrogen [32]. Advanced injection timing (30–60 bTDC) can be used to reduce both NO_x and smoke, but can result in unstable combustion timing [40]. In that study, advanced timing also resulted in longer and slower heat release compared to usual diesel timings, with earlier injection timing resulting in later and slower heat release. A diesel injection strategy with two injections, consisting of a small pilot at variable timing (7.5-20 bTDC) followed by a variable diesel injection at TDC, was investigated [41]. Hydrogen combustion efficiency could not be measured, but was estimated from analysis of hydrocarbon, CO_2 and water vapour in the exhaust stream to be 20-100% depending on operating point.

Autoignition is a problem often encountered in hydrogen-diesel dual fuel studies. Greater than 8% hydrogen in intake air (H2int>8%) in a heavy-duty engine, or H2int>20% in a light-duty engine could auto-ignite before the diesel injection and cause unwanted knock [42]. This discrepancy was attributed to the heavy-duty engine having a cast iron piston, which was expected to run hotter and therefore have a greater chance of autoignition compared to the light-duty engine with an aluminum piston [42].

To reduce carbon dioxide emissions, the usage of diesel fuel should be reduced thereby increasing hydrogen energy share (HES). Often, the use of port-injected hydrogen is associated in the literature with higher peak heat release, but this depends on operating point. Heat release in diesel engines [9, 43, 44] and dual-fuel engines [40, 42, 45, 46] has been shown to progress in several stages. These stages are referenced in Chapter 5. In one study, H2int was swept between 0–6 vol% at a constant load [45]. The authors divided the heat release into 3 stages, with the first and third stage attributed to diesel diffusion combustion, and the middle stage attributed to a combination of hydrogen and diesel. At 70% total engine load (HES≈31%), this middle stage was found to be significantly increased by hydrogen addition. However, at 30%

total engine load the peak heat release was similar with and without hydrogen addition, and at 15% load (HES≈77%) hydrogen peak heat release was lower when more hydrogen was used. A naturally-aspirated single-cylinder 0.573L engine was experimentally tested at 7 bar IMEP and HES from 2-40% [47]. Injection timing of 20 bTDC and diesel fuel pressure of 210 bar was used. They found higher Maximum Pressure Rise Rate (MPRR) associated with higher HES.

An increase of peak heat release rate was predicted to occur with larger diesel injection duration in a computational study [48]. Advancing pilot injection timing from 10 to 30 bTDC was predicted to increase peak heat release. However, further advancing diesel pilot injection timing from 30 to 50 bTDC was predicted to reduce peak heat release and peak pressure.

Engine knock was numerically modelled for intake air charges of H2int>5% and found to occur in the piston bowl and piston crown areas [49]. Applying this study to the engine used in this thesis, the combustion chamber shape above the piston crown is different at different points in the stroke as the piston is closer or further from the cylinder head. This may affect metrics such as Maximum Pressure Rise Rate (MPRR). Another study ran an engine with SI hydrogen, and found intake temperature to be the most important factor in knocking [50]. A zero-dimensional reactor simulation was found to be suitable to predict the occurrence of knocking, but not for predicting the resultant pressure trace or exact timing of the event [51].

In an engine with a compression ratio of 9, hydrogen-air mixtures could not be driven into end-gas autoignition [50]. Adding argon to increase the heat capacity ratio, which increased the temperature generated by compressing the end gas, achieved autoignition and knock [50].

The presence of hydrogen affects the ignition delay of diesel injections [45, 52–54]. At 5.32 bar IMEP, ignition delay was found to increase approximately 2 CAD with hydrogen compared to diesel-only, while increasing with advancing SOI from

SOI=-20 to -32 CAD [53]. This delay period has been modeled relative to reduced oxygen in the cylinder [52]. As HES is increased 0–50%, ignition delay tends to peak near HES=25%, dependent on load, and reduce as HES increases to 50% [52]. This effect on combustion auto-ignition delay has also been proposed as a means to control HCCI combustion phasing [55, 56].

Some studies have used Exhaust Gas Recirculation (EGR) to modify hydrogen and diesel-hydrogen combustion [39, 42, 57]. But, measurement of the rate of recirculated exhaust gas vs fresh air has some difficulties, as intake CO_2 based measurement no longer makes sense. Oxygen based EGR measurement is recommended in [58] and a correlation with existing Air-Fuel sensors can be used [59].

1.4 Hydrogen Slip

Incomplete combustion of hydrogen fuel has been reported for port-fuel-injected spark ignition engines [16], direct-injected spark ignition engines [17, 60], and dual-fuel diesel engines [39, 45, 61, 62]. This is not unique to combustion engines. A hydrogen fuel cell required controls [63] to keep exhaust gas concentration below UN regulations for fuel cell vehicles, which are 4% average and 8% peak [64]. Techniques were developed to keep fuel cell exhaust under 2% during warm up [65]. Purge routines at startup and shutdown also cause significant hydrogen to be emitted from fuel cells [66]. Co-generation by burning solid oxide fuel cell exhaust has been proposed [67–69]. Whether in fuel cells or ICEs (which are the focus of the present work) hydrogen emissions will need to be controlled to realize the full GHG-reduction potential of this fuel [70, 71].

While molecular hydrogen is not acutely toxic, and is even being investigated in animals at levels of 4 vol% in breathing air to increase liver health and reduce lipogenesis [72], the global warming potential of hydrogen emissions due to effects on methane and ozone has been reported. A study from 2001 calculated the warming potential of 1kg of unburned hydrogen to be 5.8 times that of 1kg of carbon dioxide, over a 100-year timescale [70]. More recently in 2023, a value of 11.6±2.8 times has been reported on the same time scale [71].

With the primary motivation of switching to hydrogen fuel being the reduction of global warming through reduction in carbon dioxide, large emissions of unburned hydrogen can reduce the advantages of this fuel. The lower heating value (LHV) of hydrogen has been reported as 119.6 MJ/kg [73] and diesel as 42.5 MJ/kg [74]. Using the 11.6 factor of CO_2 equivalency above [71], a hydrogen engine with a 22% of hydrogen fuel remaining unburned will emit 25% as much GHG potential as a diesel engine if both are operating at the same overall thermal efficiency, thus underscoring the importance of characterizing and managing unburned hydrogen emissions. These emissions, and effect on CO_2 equivalent totals, will be described in detail in Chapter 4.

However, unburned H_2 can also enhance catalyst performance in NO_x reduction. Reformer gas ($CO+H_2$) was fed into an engine and the differing exhaust composition (presumed to contain unburned hydrogen) was found to enhance catalyst activity [75]. Testing was also performed with hydrogen added separately to the exhaust gas at 0.1% and 0.3% by volume, with benefit to catalyst activity [75]. The use of urea as a reducing agent produces carbon dioxide as a byproduct, which adds to tailpipe CO_2 emissions, while hydrogen does not [76, 77]. With hydrogen, catalysis is effective at lower temperatures compared to other methods [76, 77]. Logistically, this method has no need of a separate urea or ammonia tank. While the present thesis focuses on reduction of hydrogen slip, an understanding of this phenomenon could be used to optimize a correct amount of unburned hydrogen into a NO_x aftertreatment system.

To date, relatively few studies focus on H_2 slip. One study, on a spark-ignition engine, found that hydrogen-air fuel ratio was the dominating factor [16]. For H2int=5%, up to H2exh=2.5% was found, representing 50% combustion efficiency. Combustion efficiency increased with H2int, reaching η_{H2} =99.5%.

In another study, a diesel engine was operated with a stock controller, and hydrogen added to the intake. Peak H2exh=1.4% was observed at H2int=6% [61]. Again on a diesel engine with stock controller, H2int=4% resulted in H2exh=1% [62]. In that study, methane was also tested. Hydrogen combustion efficiency was similar to but slightly better than that of methane [62].

Combustion efficiency was studied on a turbocharged 10.8L engine running in dual-fuel mode [45]. At 70% overall load (15 bar BMEP), when H2int=6% (HES≈31%), hydrogen combustion efficiency was η_{H2}=98%. At this load, reducing H2int to 1% (HES≈5%) resulted in η_{H2}=93%.

Emissions, including unburned hydrogen, were experimentally tested for 0–80% hydrogen energy fraction [39]. That study varied several factors including EGR, timing (-10 to +10 CAD), and equivalence ratio of H_2 (0.10 to 0.20, corresponding to H2int= 4% and 8% respectively). The authors concluded that EGR is effective in reducing unburned hydrogen but increases soot. Advancing diesel injection timing reduces unburned H_2 but increases NO_x, and an advanced CA50 near TDC is associated with reduced H_2 emissions. Diesel post-injection had mixed results, where $\eta_{\mathrm{H2}} <$90% for most tested points.

For a single cylinder, 2 litre displacement, diesel engine operating at at 1200 RPM and 9.5 bar IMEP, hydrogen addition resulted in a 1-1.5% drop in thermal efficiency [78]. Based on comparison of the thermal efficiency obtained, the authors also speculate that the high diesel injection pressure used (2,000 bar) promoted good combustion of the hydrogen fraction and through increased entrainment/mixing, but lacked the instrument to measure H_2 slip directly. They indicate that diesel injection pressure may have an effect on hydrogen combustion efficiency.

Lean hydrogen flames exhibit thermo-diffusive instability, which is unusual [7, 79]. Rather than a flame front advancing through a pre-mixed and largely stationary mixture (where any control volume is equivalent, so combustion within the flame is assumed to have near perfect efficiency and all slip is due to effects such as crevice volume and wall quenching), the hydrogen molecules in lean mixtures (ex. $\phi_{H2} = 0.3$ equivalent to H2int=13%) can diffuse faster than heat. This results in areas that are too lean to burn, and a fractal [79] progression of the flame front. Remaining hydrogen in these lean areas would then contribute to slip. A similar process can lead to spiral patterns for combustion under rich conditions [80]. This mass transfer effect, where fuel moves to the flame, can lead to flame propagation through narrow gaps [81], with the reaction paths compared to the propagation of starving micro-organisms [81].

Exhaust emissions of hydrogen are not limited to dual-fuel operation. Small amounts from hydrocarbon-fuelled engines have been measured [9], with one study finding up to 200ppm from diesel engines during cold starts and some acceleration phases [82] or up to 1500 ppm from gasoline engines [83]. The referenced studies also found a link between H_2 and CO production, where higher CO was associated with higher H_2, with wide variance in the H_2/CO ratio. Other studies running with rich (up to AFR=8) combustion in carburated engines have found up to H2exh=0.33% [84], up to H2exh=4% [85] and up to H2exh=8% [86] and a relatively constant H_2/CO ratio of about 2—4 [84–86]. Although rich combustion in carburated engines is a different condition to the globally-lean combustion in diesel engines at low load, the agreement in literature of a link between CO and H_2 production is worrysome. Many hydrogen sensors have cross-sensitivity to CO [87], therefore it is important to distinguish between CO cross-sensitivity and real hydrogen when measuring engine exhaust.

1.5 Outline of Thesis

Minimizing unburned hydrogen emissions is important to achieve the maximum global warming reduction potential of hydrogen fuel. This thesis looks to quantify slip in hydrogen-diesel dual-fuel engines at low-load and mid-load points, and investigates injection strategies (timing and duration) to ameliorate slip encountered in low load operation. Heat release curves are calculated and discussed for these test points and observed patterns reported on.

In order to accurately measure hydrogen emissions, a commercial sensor is characterized using a high-accuracy gas mixing rig. This investigation forms Chapter 3 of this document.

A retrofit engine is run at low-to-mid-load in port-injected hydrogen-diesel dual-fuel mode with a single diesel injection of varying timing and duration. During all tests fuel pressure is kept constant at 993 bar and engine speed is kept at 1500 RPM. The engine is run naturally aspirated and without exhaust gas recirculation. Unburned hydrogen in exhaust and maximum pressure rise rate are measured. The global warming potential of the unburned hydrogen is calculated and compared with that of the associated carbon dioxide emissions. This investigation forms Chapter 4 of this document.

Heat release curves are calculated for the above engine operating points and the observed patterns are discussed. This investigation forms Chapter 5 of this document.

Main contributions of this thesis include:

- Characterization of a commercial hydrogen sensor for the ”off-label” purpose of measuring dual-fuel engine exhaust
- Detailed measurements of unburned hydrogen at a variety of low-load points, in a series of controlled experiments with diesel injection timing and duration varied
- Calculation of the impact of unburned hydrogen to global warming potential of this engine, and the effect of operating parameters on this total
- Calculation of heat release rates, and discussion of phases observed in the combustion and how these are affected by operating parameters

Chapter 2

Engine Setup

2.1 Overview

This research is performed on a 4-cylinder common-rail diesel engine of 4.5L displacement. Details on the mechanical assembly are given in Section 2.2, and modifications to add port-injected hydrogen are given in Section 2.3. Process input and outputs are represented in Section 2.5.

To measure unburned hydrogen, exhaust is sampled and cooled before passing through a carbon monoxide sensor and hydrogen sensor. The carbon monoxide measurement is used to compensate the hydrogen reading due to cross-sensitivity of the sensor to carbon monoxide. The gas sampling system is discussed in Section 2.8.

A view of the engine setup is shown in Fig. 2.1. Engine controls and data aquisition are located to the left of the engine, labelled “ECU/DAQ”. The engine is fed diesel fuel from a tank located near the engine, which is periodically re-fuelled using portable containers. Hydrogen fuel is stored in a ventilated cabinet, located off-camera. At the flywheel end of the engine, a damper assembly reduces torsional vibrations before a shaft couples the torque to the dynamometer.

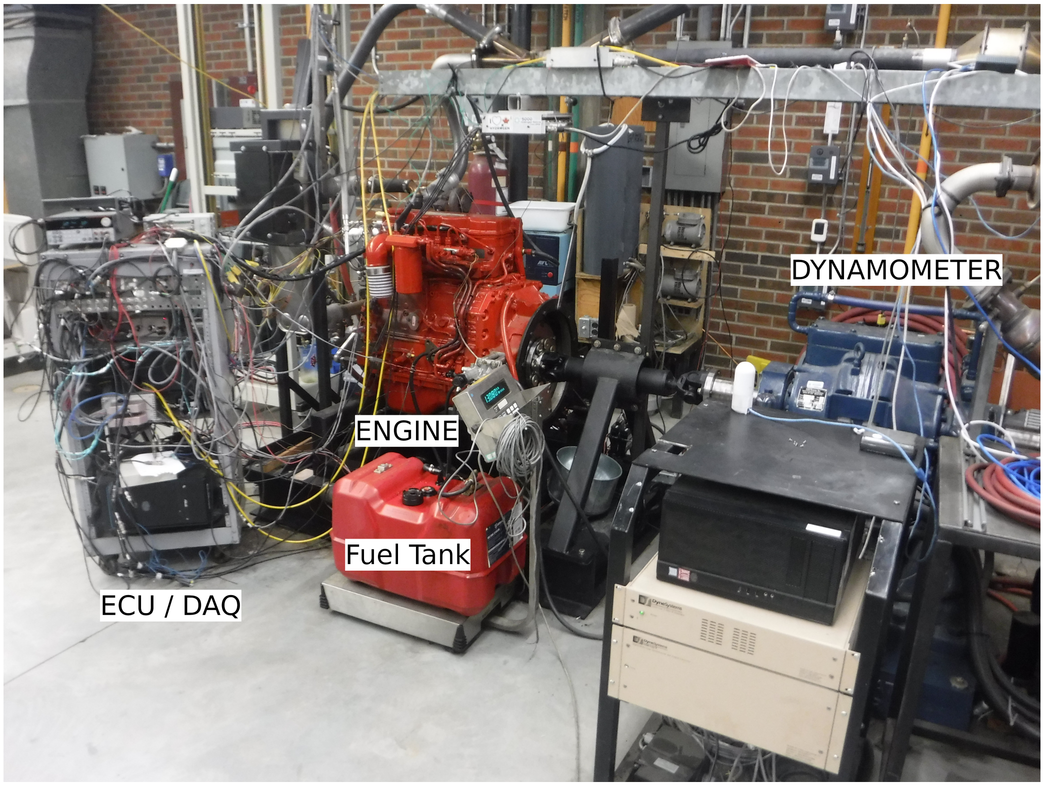

Figure 2.1: Overview Photo of Engine and Dynamometer Setup, Showing Controls Rack with Engine Controller (ECU) and Data Aquisition (DAQ), Engine, and Dynamometer

The engine is controlled using a dSpace MicroAutoBox2 (MABX) system, with RapidPro power drivers. The controller user interface is implemented with a dSpace ControlDesk program running on a separate computer. There are two data acquisition systems. Low-speed (1kHz) data is collected using the ControlDesk interface. High-speed data (0.1 CAD resolution or 90 kHz at 1500 RPM) is aquired with a data acquisition card running on a separate computer. Engine Controls and data aquisition are discussed in Section 2.7, with high-speed in-cylinder pressure measurement and logging discussed in Section 2.6. Analysis of the resulting in-cylinder pressure trace is discussed in Section 2.9.

2.2 Engine Mechanical Assembly

The test engine is based on a Cummins QSB 4.5L Tier 3 engine (Fig. 2.2), with nominal power output 160HP (119kW) at 2500 RPM. This was designed for stationary applications such as generators or water pumps. Details of the engine geometry is given in Table 2.1. Of the four cylinders, one is converted to dual-fuel by the addition of a hydrogen injector in the intake runner. Compared to converting all 4, this reduces the amount of hydrogen fuel that must be stored. The turbocharger has been removed, due to the exhaust of one cylinder being separated, and thus this engine is naturally aspirated. This engine has been the subject of several other studies [41, 88, 89] focussed on HDDF operation.

MANUFACTURED BY CUMMINS INC.
Assembled in the USA ®
5287983
Date of Mfg: 07-29-14
WARNING: Injury may result and warranty is voided if fuel rate, rpm or altitudes exceed published maximum values for this model and application. For Constant Speed Use Only.
C.I.D./L 272 / 4.5
CPL 8725
Engine Serial No. 73717711
Family ECEXL0275AAG
Cust Spec. U OF A QSB4.5 ENGINE
Model QSB4.5
FEL
EPA
NOx+NMHC 4.0
PM 0.30
Valve Lash Cold Inch 0.010 Int. 0.020 Exh.
MM 0.254 Int. 0.508 Exh.
Timing – T.D.C.
Fuel Rate at Rated HP 116 mm3 / stroke
Firing Order 1 3 4 2
FR FR91601
Low Idle RPM 750
Gross Rated HP/KW 160 / 119 at 2500 RPM
ECS DDI ECM TC CAC
IMPORTANT ENGINE INFORMATION: In the U.S. this engine may be used only in stationary emergency applications in accordance with requirements of 40 CFR Part 60 and is excluded from the of 40 CFR Part 89 and 1039. Installing or using this engine in any other application may be a violation of U.S. Federal Law subject to civil penalty. THIS ENGINE IS CERTIFIED TO OPERATE ON DIESEL FUEL.

WARNING
Do not open high pressure fuel system with engine running.
Engine operation causes high fuel pressure.
High pressure fuel spray can cause serious injury or death.
4938452

Figure 2.2: Engine Nameplate Showing Model and Serial Numbers, and Nominal Rated Power

Four valves (2 intake plus 2 exhaust) are present per cylinder. The stock head contains cast-in intake runners, the middle 3 of which split to feed one valve for

Table 2.1: Engine Parameters

Parameter	Value
Total Displacement	4.460 L
Number of Cylinders	4
Bore	107 mm
Stroke	124 mm
Connecting Rod Length	192 mm
Compression ratio	17.2:1
Piston Protrusion	0.43 mm
Headgasket Thickness	1.6 mm
Valve train	Pushrod
No. of valves (In/Ex)	2/2
No. of Camshafts	1
Max. valve lift (In/Ex)	8 mm/8 mm
Valve angle (In/Ex)	0 ◦ /0 ◦
Valve diameter (In/Ex)	33 mm/33 mm
Combustion Chamber	Bowl in Piston
Injection Pressure	300-1500 bar
Spray Angle	124 ◦
Injector Pattern	8 Holes
Injection Plane	Single
Injector Actuation	Solenoid

each of two cylinders (Fig. 2.3). Therefore, the intake system for any one cylinder cannot be separated without extensive head modifications or blocking one intake valve (modifying volumetric efficiency and swirl pattern away from stock). This presents issues in measuring airflow into the converted cylinder. Exhaust, however, can be isolated for the one separated cylinder.

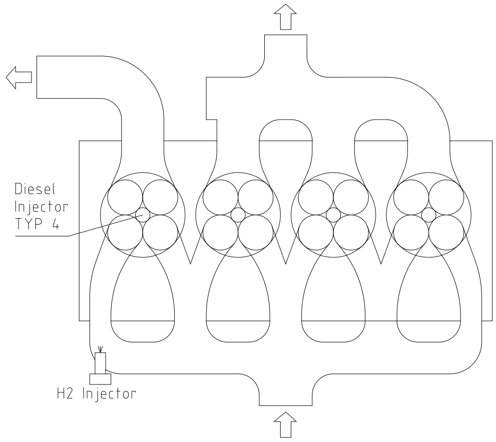

Figure 2.3: Cylinder Head and Runner Layout

While measuring exhaust mass flow would theoretically be possible, several difficulties present themselves. The pulsating nature of the flow creates errors in orifice or venturi meters due to the square-root dependence of flow on pressure differential, and temperature and composition change the density and viscosity of the exhaust stream [90]. This engine does not have intake or exhaust mass flow measurement, and instead the following work uses gas analysis and assumed volumetric efficiency to estimate fuel and air flows respectively.

Volumetric efficiency was measured using hydrogen as a trace gas while motoring. This was found to be 0.91 at 1500 RPM. This compares to another study on this engine, which found 0.85 when the injector was firing [41]. That study had a more restrictive intake explaining the discrepancy.

The common-rail diesel fuel system remains pressurized by the stock Bosch CP3S3 fuel pump assembly. The first stage of this assembly is a gear pump, which pressurizes the fuel to approximately 14 bar. From here, this is passed through a variable restrictor orifice, controlled by a solenoid to vary fuel flow. This is given a duty-cycle signal from a PID controller to keep pressure constant. From the variable orifice, fuel passes to the high pressure triplex piston pump. In all tests the fuel pressure is held constant at 993 bar, although this can be varied between approximately 300—1500 bar. A relief valve set to 1700 bar protects from overpressure.

2.3 Hydrogen Injector System

Hydrogen is injected into one intake runner of cylinder number 1 as shown in Fig. 2.3. The injectors used are Hanna H2200A model, originally manufactured for natural gas and propane service [91]. Two screws hold the injector into a custom machined block, with hydrogen fuel entering through the side of the injector and exiting out the end. A RapidPro power module is used to provide a 24V, peak-and-hold power profile to the solenoid. Fig. 2.4 shows the injector mounted on the intake manifold.

Due to the intake runner configuration, hydrogen must be injected during the suction stroke to avoid spilling over into the next cylinder, which would invalidate the hydrogen flow rate measurement. Timed injection also reduces the amount of flammable mixture in the intake, reducing the consequences of backfire. Timing of these injection events is represented in Fig. 2.5.

Hydrogen is delivered in K-size bottles with a capacity of 200 Standard Cubic Feet at 2000 PSI, amounting to 450 grams hydrogen. In-use bottles are stored in a ventilated cabinet. From the bottle, the pressure is reduced to 100 PSI with a standard diaphragm-actuated regulator. A surge tank is placed before the injector, to reduce pressure pulsations that would cause inaccuracies in measuring hydrogen flow. Hydrogen flow rate is measured by an OMEGA FMA-1611A mass flow meter, using differential pressure across a laminar flow element.

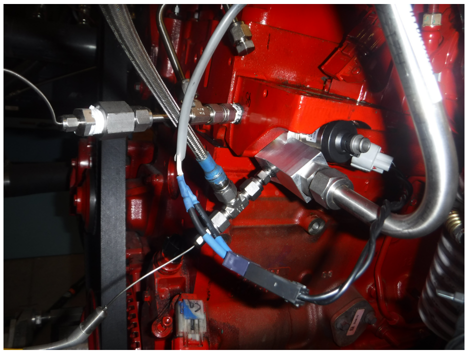

Figure 2.4: Hydrogen Injector, Mounted on Intake Manifold

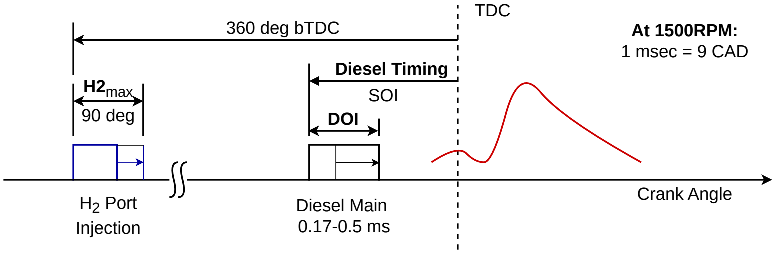

Figure 2.5: Injection Timing Diagram for Hydrogen and Diesel

2.4 Dynamometer

Torque is applied with a Taylor model 1014 250HP eddy-current dynamometer. A Taylor Inter-Lok V controller uses PID control to regulate the dynamometer in constant-speed mode, and the setpoint can be adjusted using an operator panel or analogue input from the dSpace control system. Equipment nameplate is shown in Fig. 2.6, showing model and manufacturer.

Figure 2.6: Nameplate of Dynamometer Used to Load Engine For Testing

2.5 Process Inputs, Outputs and States

Several main inputs to this engine are varied during operation, as shown in Fig. 2.7. Hydrogen fuel is added via an injector located in the intake port, where duration of injection (DOI H2) determines the quantity per stroke. This injection is timed to start near the beginning of the intake stroke, and timing is fixed. Diesel is direct-injected, with DOI determining the quantity. The start of injection (SOI) is varied during these tests. In this thesis, engine speed is held constant at 1500 RPM.

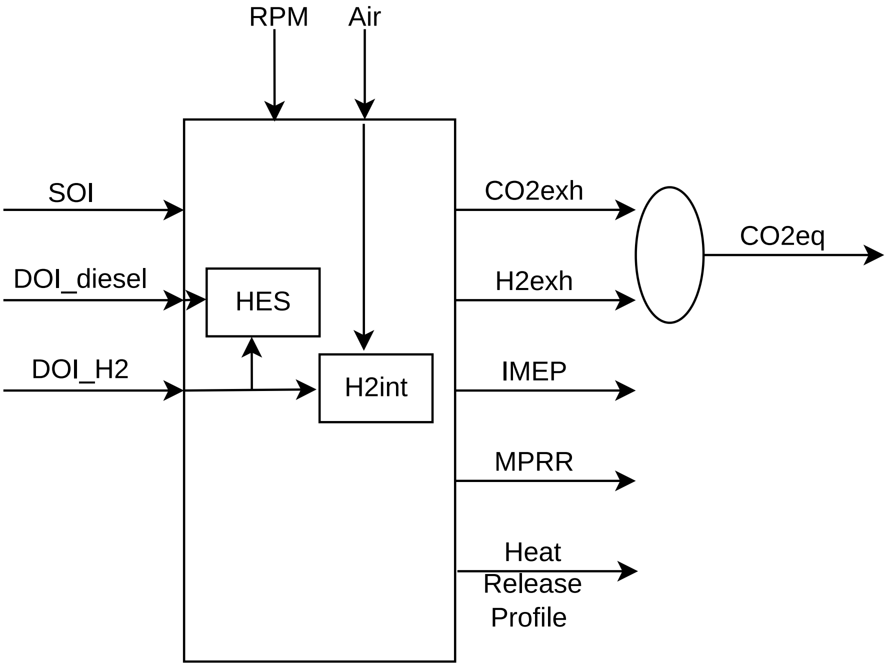

Figure 2.7: Engine Inputs and Outputs

H2int, the volume fraction of hydrogen in intake air, is defned as:

$$\text{H2int} = \frac{\dot{V}_{\text{H2}}}{\dot{V}_{\text{air}} + \dot{V}_{\text{H2}}} \tag{2.1}$$

where $\dot{V}_{\text{H2}}$ refers to the (measured) volumetric flow rate of hydrogen, and $\dot{V}_{\text{air}}$ the volumetric flow rate of air.

Eqn. 2.1 requires the flow rate of air. The combined volumetric flow rate of air and hydrogen fuel, $\overset{\bullet}{V}_{\mathrm{air}} + \overset{\bullet}{V}_{\mathrm{H2}}$, is calculated from

$$\overset{\bullet}{V}_{\mathrm{air}} + \overset{\bullet}{V}_{\mathrm{H2}} = \frac{\eta_{\mathrm{v}} V_{\mathrm{d}} \omega}{60 \frac{\mathrm{seconds}}{\mathrm{minute}} 2 \frac{\mathrm{strokes}}{\mathrm{revolution}}} \tag{2.2}$$

where η_{v} is volumetric efficiency, V_{cyl} is cylinder swept volume, ω is engine speed in RPM, and the factor of 2 is due to four-cycle operation.

From here the flow rate of hydrogen can be subtracted to obtain $\overset{\bullet}{V}_{\mathrm{air}}$.

HES or Hydrogen Energy Share refers to the proportion of total fuel energy made up of hydrogen fuel.

$$\mathrm{HES} = \frac{\overset{\bullet}{m}_{H2} \mathrm{LHV}_{\mathrm{H2}}}{\overset{\bullet}{m}_{\mathrm{H2}} \mathrm{LHV}_{\mathrm{H2}} + \overset{\bullet}{m}_{\mathrm{DFO}} \mathrm{LHV}_{\mathrm{DFO}}} \tag{2.3}$$

Where $\overset{\bullet}{m}_{H2}$ refers to the mass flow rate of hydrogen (calculated using measured $\overset{\bullet}{V}_{\mathrm{H2}}$ and ideal gas laws), $\mathrm{LHV}_{\mathrm{H2}}$ refers to the Lower Heating Value of hydrogen of 119.6 MJ/kg [73], $\overset{\bullet}{m}_{\mathrm{DFO}}$ is the flow rate of diesel fuel oil (obtained using exhaust gas analysis) and $\mathrm{LHV}_{\mathrm{DFO}}$ is the Lower Heating Value of diesel fuel taken to be 42.5 MJ/kg [74].

The CO_2 concentration in exhaust gas (CO2exh)is measured and used to calculate CO_2 emissions. Hydrogen exhaust concentration (H2exh) is also measured. The greenhouse potential of hydrogen is combined with that of CO_2, to calculate a CO_2-equivalent emissions metric (CO2eq). Details are given in Section 2.8.

Indicated Mean Effective Pressure, a measure of normalized engine torque before frictional losses, is calculated using the recorded pressure trace. Maximum Pressure Rise Rate (MPRR) is calculated as a measure of rough or noisy combustion. The in-cylinder pressure profile is used to calculate the heat release profile. Details are given in Section 2.9.

Total diesel fuel mass is calculated based on measured CO_2 and CO concentrations, however it is considered an intermediate calculation and is not included in the above diagram. CO is measured however is only used for CO_2 equivalent calculation and to correct the hydrogen sensor readings for cross-sensitivity.

2.6 In-Cylinder Pressure Measurement

Each of the four cylinders contains an in-cylinder pressure sensor. This allows calculation of combustion metrics such as burn rate, burn duration and Indicated Mean Effective Pressure. Having all cylinders instrumented is useful to calculate frictional losses (FMEP) and to check that hydrogen is not escaping the test cylinder into the other cylinders.

Choosing a good in-cylinder pressure sensor location is important for measurement accuracy and to reduce false ringing. However, good locations often conflict with structures such as valvetrain components and oil passages, and often must pass through coolant channels and/or intake runners. In this engine, where the bore passes through intake runners and coolant passages, a sleeve is installed to seal these features. The location of the cylinder pressure tap within the combustion chamber (pressure sensor has been removed) is seen in the lower left of Fig. 2.8, between exhaust and intake valves and near the edge of the cylinder.

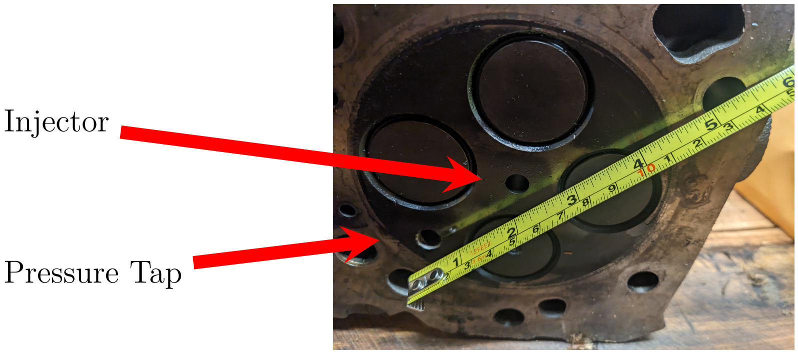

Figure 2.8: Location of Cylinder Pressure Tap

Cylinder 1, due to an expectation of higher pressure combustion using hydrogen, uses a cylinder pressure transducer rated to 350 bar. The other three use a sensor rated to 300 bar. Uncooled sensors are used as this reduces the diameter of the sensor (no need for separate cooling water channels), reduces logistics around providing distilled water for cooling, and eliminates risk of damage from a failed coolant pump.

Natural frequency of the Cylinder 1 sensor is 65 kHz. These traces are recorded at 0.1 CAD intervals, which corresponds to 90 kHz at 1500 RM engine speed or a 45 kHz Nyquist limit for this testing. Cylinder ringing has been observed in operation on the order of 2, 4 and 7 kHz, which this sample rate and sensor natural frequency can faithfully replicate, although heavy knock events have shown signs of exceeding this bandwidth. Operating points in this thesis are chosen to avoid knock events. Specifics of the pressure sensors used on this engine are given in Table 2.2. To convert the low level output from this sensor, which takes the form of a small charge difference on the order of 10 nano-coulombs at full-scale, a Kistler 5064C amplifier is used. This also has the function of stabilizing voltage on the measurement leads, reducing the effect of stray capacitance that can be changed by bending the coaxial cables leading to the sensors. Drift of this inherently differential-based sensor is corrected by pegging (setting to a known value) the pressure reading during each intake stroke in post-processing.

A National Instruments (NI) PCIe-6351 Data Aquisition card is used to record the data for all four cylinders. To start recording the operator uses a Matlab script to load parameters into the card. This card is capable of outputting a voltage profile while making input measurements, which is used to start the MABX system recorder thus synchronizing the high-speed and low-speed data. The output buffer is loaded with a profile first consisting of low voltage for several cycles (times 7200 datapoints per cycle), then high voltage for the number of cycles that are to be recorded, then a low voltage to stop the MABX recording. A 3600 pulse-per-revolution encoder with index channel, attached to the crankshaft, is used as an external clock of the NI card to trigger. Once the parameters are set via the Matlab script, the next index pulse from the encoder starts the process. This ensures that the high-speed recording always starts at a consistent crank angle. Further details on data collection are found in Section 2.7.

Table 2.2: In-Cylinder Pressure Sensors with ω_0 being natural frequency of the sensor and P_{max} being maximum allowable pressure

Cylinder	Kistler Model	ω_0 (kHz)	P_{max} (bar)
1	6124a	65	350
2,3,4	6125c	70	300

2.7 Control and Data Collection

2.7.1 Overview

Control and data collection requires several interlinked systems, as presented in Fig. 2.9. Real-time control of the engine is accomplished with a dSpace MicroAutoBoxII (MABX). Most of the sensors, including hydrogen slip and coolant temperature are recorded here. Custom firmware for the MABX, written in Simulink, is uploaded using a Personal Computer (PC) and data is collected using the same computer. Higher speed data collection, including high-resolution cylinder pressure, is accomplished with a PCI-connected data acquisition card, running in a headless PC. Another PC remotes to this data collection computer. The dynamometer speed is controlled by a separate system, as discussed above.

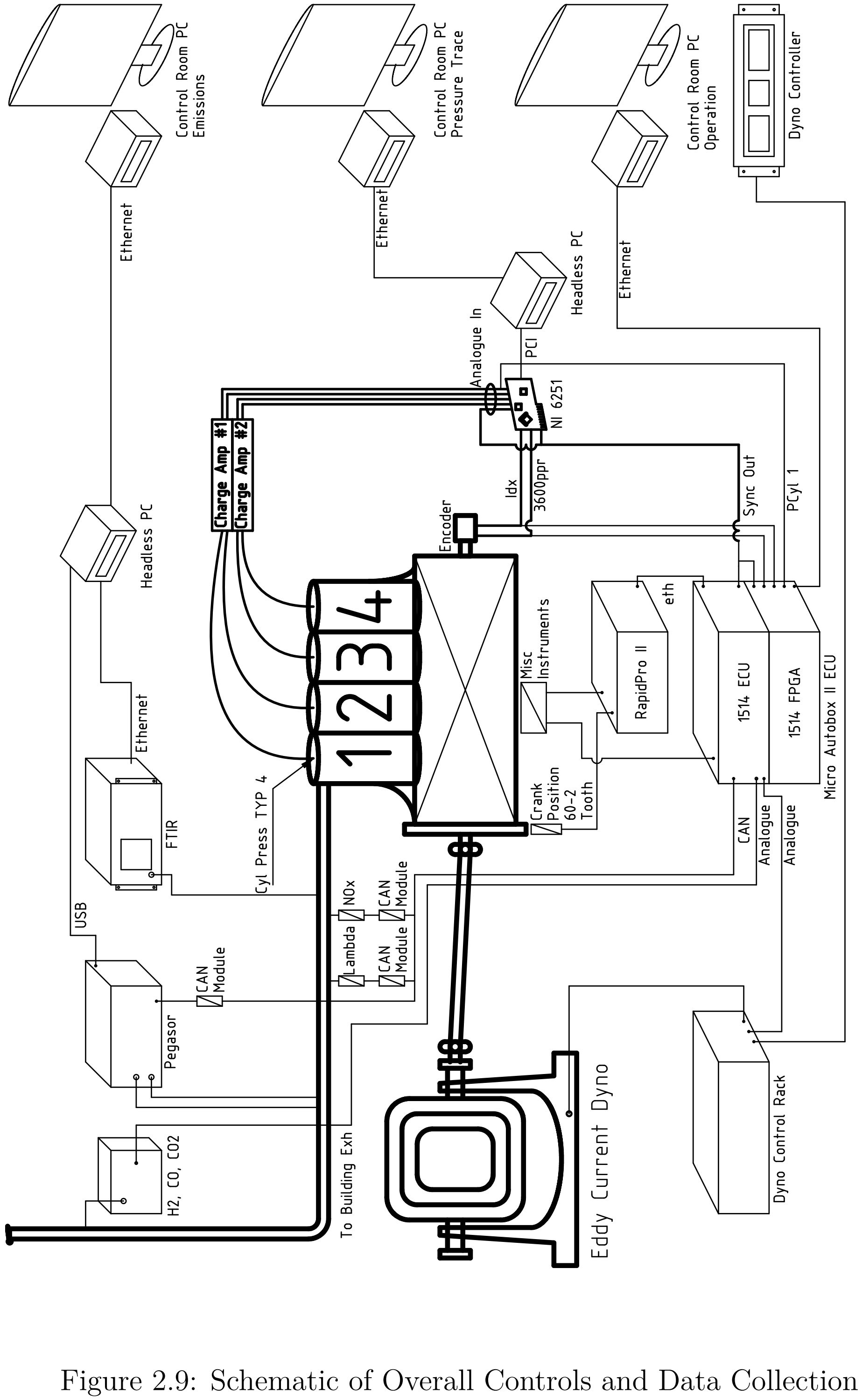

Figure 2.9: Schematic of Overall Controls and Data Collection

2.7.2 Engine Control Hardware

The engine controller, a MicroAutoboxII (MABX), is programmed in Simulink allowing fully custom control over injection timing and duration of up to three diesel injections and one hydrogen injection per engine cycle. During warmup and for the three non-research cylinders, a dual-injection diesel strategy is used with speed-load maps based on the factory ECU [41]. For this research, an injection angle and duration is prescribed. A dSpace RapidPro contains injector drivers, which use the stock flywheel and flywheel position sensor to time injections. The simulink model runs on CPU, a 32-bit IBM PPC-750GL with one core, at a constant rate for the whole program of 1kHz.

The MABX system also contains a module with a Xilinx Kintex-7 Field Programmable Gate Array (FPGA). Here it is configured to perform all calculations in parallel, allowing the execution of simple calculations at a high speed. This unit is used to calculate combustion metrics such as IMEP and MPRR. These values are updated every 0.1 CAD, which at 1500 RPM corresponds to a 90 kHz. The updated value is passed to the Simulink model and saved at that model's sample rate.

2.7.3 Pressure Trace Encoder Calibration

Accurate determination of the position of Top-Dead Centre (TDC) is important, and small angular errors can introduce large errors in further calculation of combustion metrics such as IMEP and heat release [92–94].

When an engine is motored, the peak pressure occurs before the real TDC position, with the delay termed the Thermodynamic Loss Angle. This is due to transfer of heat out of the cylinder, and blow by transferring mass out of the cylinder. This angle is dependent on engine model and condition and varies according to operating point. Determination of true TDC position and peak pressure relative to true TDC has been the focus of many studies. In general, this angle should be between 0.0–2.0 CAD, and values outside that range mean that the setup should be checked [95].

Thermodynamic loss angle has been measured on two spark-ignition engines of compression ratio (CR) 9.4 and 9.7 motoring at 1000–2500 RPM [93]. Thermodynamic loss angle increased with slower RPM, and took on values between 0.4–1.5 CAD [93]. Values of 0.67–0.82 CAD were found between 1500–3000 RPM in a 4-cylinder SI engine of 1242 cc displacement [96]. Another study found 0.3–0.5 CAD was reasonable for spark-ignited engines [94]. 0.8–0.95 was measured as intake pressure varied 0–800 mmHg [97]. For wide-open throttle at a compression ratio of 10, varying RPM from 1000 to 3000 changed the measured value from 0.8–0.45 CAD [98]. For two SI engines of compression ratio 9.4 and 9.7, coolant temperature was found to have an effect [93]. Paradoxical to the idea of being driven by heat loss, a higher coolant temperature was found to increase the loss angle, with the authors speculating that differential thermal expansion increased ring end gap and thus blowby.

Simulating a diesel engine with compression ratio of 22, resulted in loss angles of 0.88,0.62, and 0.63 CAD depending on the wall heat loss models used [98]. In an engine with 16.2 compression and 160mm x 160mm bore x stroke, loss angle of 0.9–1.2 CAD was experimentally determined [99]. In a larger engine of 886 kW maximum power, 0.86 CAD was measured [100]. In a smaller 4-cylinder, 44 kW engine 0.4 CAD was measured [101].

For further analysis in this thesis, a procedure detailed in the literature is used to calibrate encoder position [94]. The engine is motored and a combination of Linear Least Squares regression and nonlinear optimization is used to predict an appropriate value of heat capacity ratio, heat transfer coefficient, and encoder offset. The base assumption is that wall heat transfer rate (dQ/dt) is constant in a small region around TDC.

The observed thermodynamic loss angle for this engine, while warm (coolant temperature = 84C) and at 1500 RPM, is 0.4 CAD. This is at the low end of the results discussed above matching prior literature on the topic [94, 101]

2.8 Emissions Measurement

Measurement of unburned hydrogen emissions is a main contribution of this work. To accomplish this a commercial hydrogen sensor, RKI Industries part number 752-04, is used. CO and CO_2 emissions are measured by a Siemens Ultramat 6, model 7MB123-1B23-0C1Z, using the long-wave infrared absorption principle.

The overall process flow used for measurement of hydrogen, CO, and CO_2 in exhaust is depicted in Fig. 2.10. First, the raw exhaust is drawn through a heat exchanger, which serves to cool the gas and condense the water present. This heat exchanger consists of approximately 10 feet of 1/4" OD x 0.035" wall copper tube, submerged in an ice bath. The tube is coiled in the vertical direction to allow condensate to flow out of the exchanger. This ice bath serves three functions. First, the sensing equipment is protected from high temperature and the effect of condensation. Second, temperature is kept consistent, minimizing a possible source of error. Third, water vapor will always be present during engine operation. Cooling to a low temperature both removes the majority of the water, and keeps it at a constant level, equal to the vapour pressure near 4° C. Condensed water is stored in a container of $\approx$30mL volume, which must be emptied every 10,000 engine cycles depending on load. While a larger volume container would require less frequent service, the small volume reduces time for the system to reach steady state. The sampling setup has both transport delay and lag behavior, requiring approximately 200 cycles to reach steady-state. Most operating points are run for 1,000 cycles which was observed to be enough time for the gas analysis equipment, cylinder liner temperature, etc to reach steady state. Data from the last 200 cycles of the operating point are averaged for use in the analysis.

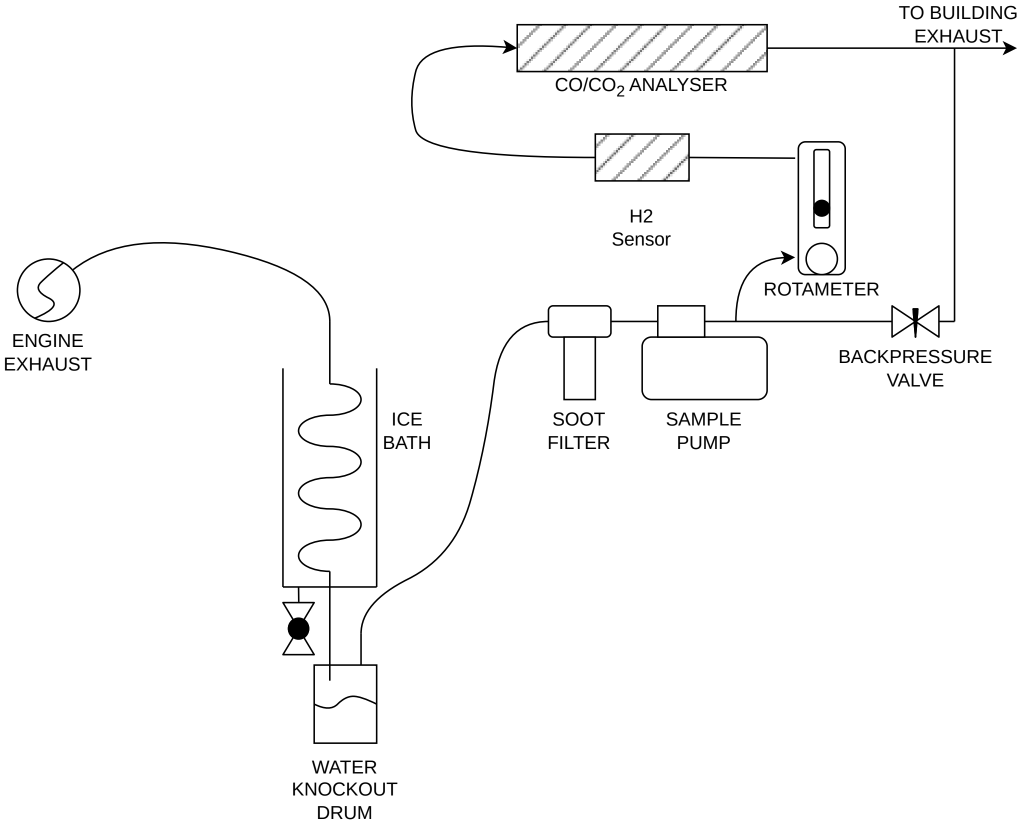

Figure 2.10: Exhaust Sampling System for CO, CO_2, and H_2 Measurement

A small sample pump is used to draw the cooled gas through the exchanger. The discharge of this pump is throttled to provide backpressure. From this higher pressure gas, a sample at constant flow rate (measured and adjusted by a rotameter) is passed through the sensing equipment.

CO and CO_2 concentration is measured by a Siemens Ultramat 6, model 7MB123-1B23-0C1Z, based on long-wave infrared absorption. This instrument was also calibrated using the gas calibration rig described in Chapter 3.

The output of the hydrogen sensor is a 0.5–4.5V analogue signal. Noise, approximately 30 mV in amplitude and with a ≈20 kHz sawtooth form, was observed on the output. A filter was added to reduce this noise by at least 60 dB. The CO and CO_2 instrument output is a 4–20 mA current, converted to 1–5 V using a 250Ω, 0.1% tolerance resistor.

Total number of mols of gas flowing through the engine per cycle, n_i, is calculated based on the ideal gas law:

$$n_\mathrm{i} = \eta_\mathrm{v} \frac{P_\mathrm{i} V_\mathrm{d}}{R T_\mathrm{i}} \tag{2.4}$$

Where η_v is volumetric efficiency, P_i is intake pressure, V_d is the displacement volume of one cylinder, R is the ideal gas constant, and T_i is the measured temperature in the intake manifold.

When the exhaust sample is cooled in an ice bath, the majority of the water is assumed to condense. This means that for every 2 mols of H_2 that burns to form water, 1 mol of O_2 is also removed. This shrinkage of the total sample volume will increase the measured concentration of emissions, and must be accounted for. With the number of mols in the sample is represented by n_s,

$$n_\mathrm{s} = n_\mathrm{i}(1 - 1.5(\mathrm{H2int} - \mathrm{H2exh})) \tag{2.5}$$

where n_i is from Eqn. 2.4, H2int is the concentration of hydrogen in the intake charge, and $H2exh$ is the concentration of hydrogen remaining unburned in the exhaust.

Measured components such as CO_2, H_2, and CO will also be dissolved in the condensate. However with the concentration of CO_2 in 4C water at partial pressure of 10 kPa being under 0.01 mol% [102], this effect is deemed to have neglegible effect on the CO_2 measurements. H_2 and CO have lesser solubility than CO_2 [103], and thus the effect of dissolved gas in the condensate on these components is again considered neglegible for the following experimentation.

$$(x + y)\mathrm{CH_2} + (1.5x + y)\mathrm{O_2} \rightarrow x\mathrm{CO_2} + y\mathrm{CO} + (x + y)\mathrm{H_2O} \tag{2.6}$$

The injected diesel fuel quantity is calculated by solving for x and y in Eqn. 2.6. The addition of diesel fuel occurs after the intake valve closes, and so does not affect the total intake volume. Combustion will have three main products, CO_2, CO and H_2O. Diesel fuel is represented in Eqn. 2.6 as CH_2, showing the the assumption of a C:H ratio near 1:2 and negligible other components such as sulphur or nitrogen.

Diesel fuel will react to form water vapour which is then removed, affecting total sample volume in a process similar to Eqn 2.5. However due to lower concentrations this effect is neglected. Once water vapour is condensed and removed, the molar total on the left of Eqn. 2.6 is $(2.5x + 2y)$ and on the right is $(x + y)$. Therefore the diesel combustion process will shrink the total cooled exhaust volume by 1.5 times the uncooled concentration of CO_2 and 1 times the concentration of CO. In the points measured in this thesis, the concentration of CO is <0.065% which is considered negligible. Concentration of CO_2 is always less than ≈3.5%, leading to an additional <5% error in measured emission concentrations, considered acceptable.

A central contribution of this work is the inclusion of hydrogen slip in greenhouse gas totals. $\dot{m}_{\mathrm{CO2eq}}$ represents the mass flow of greenhouse gas, expressed in units of CO_2 equivalent.

$$\dot{m}_{\mathrm{CO2eq}} = \dot{m}_{\mathrm{CO2}} + \dot{m}_{\mathrm{CO}} \frac{M_{\mathrm{CO}}}{M_{\mathrm{CO2}}} + 11.6 \dot{m}_{\mathrm{H2}} \tag{2.7}$$

Where $\dot{m}_{\mathrm{CO2}}$ represents mass flow of carbon dioxide, $\dot{m}_{\mathrm{CO}}$ represents mass flow of carbon monoxide, M_{CO} and M_{CO2} are the molar masses of CO and CO_2 respectively, and $\dot{m}_{\mathrm{H2}}$ is the mass flow of hydrogen in the exhaust. CO is assumed to be converted to CO_2 in future aftertreatment systems. In all points where CO2eq is presented, the concentration of CO is relatively low compared to CO_2 and such this assumption has limited effect on the total, with no points having CO/CO_2 ratio over 0.25 and the majority under 0.02. Hydrogen slip is added at a factor of 11.6 [71].

Emissions are normalized to engine load, based on Indicated Mean Effective Pressure. CO2eq represents the normalized emissions of the engine, in grams per kilowatt hour.

$$\mathrm{CO2eq} = \frac{3600 m_{\mathrm{CO2eq}}}{V_{\mathrm{d}} \mathrm{IMEP}} \tag{2.8}$$

Where m_{CO2eq} is the equivalent CO_2 emissions in grams per engine cycle, V_{d} is the cylinder displaced volume in m^3 and IMEP is in units of Pascals. The factor of 3600 converts from seconds to hours.

2.9 Pressure Trace Analysis

Analysis of the in-cylinder pressure profiles is used to provide insight into the combustion process. Three measured in-cylinder pressure traces are shown in Fig. 2.11, displaying some common features. For this thesis, TDC of the combustion stroke is defined as a crank angle of zero. Positive numbers indicate events later than TDC, and negative numbers indicate earlier. Traces from three operating points, consisting of high load, low load, and motoring (no combustion), are presented. The mean of 600 cycles at each point is shown, surrounded by ±1 standard deviation of the 600 cycles.

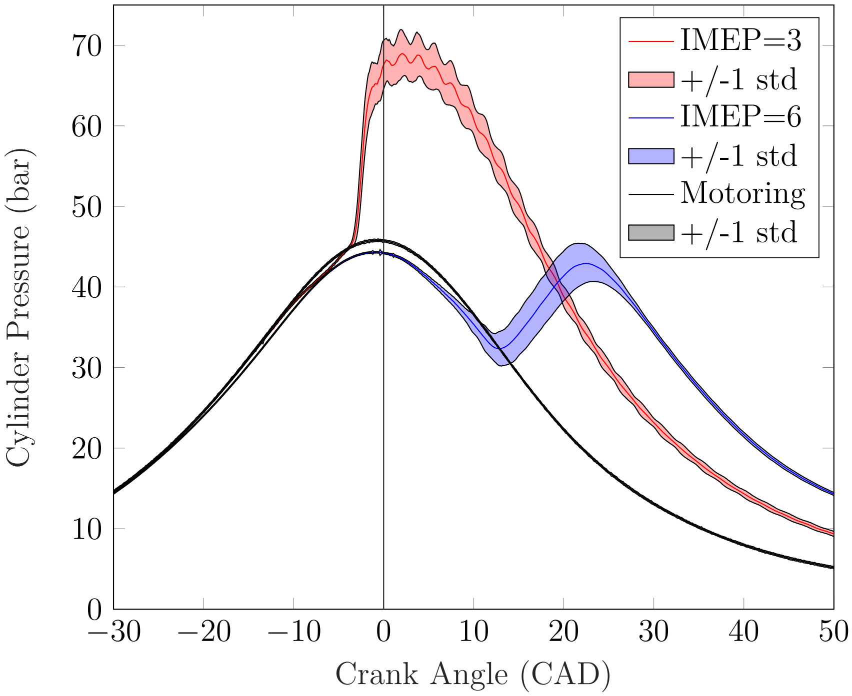

Figure 2.11: Representative Pressure Traces. The IMEP=3 case uses SOI=-14 and the IMEP=6 case uses SOI=-1

For this thesis, engine torque is calculated using IMEP, which is normalized to engine displacement. This measure has several advantages. First, by normalizing to engine displacement, it allows a direct comparison of small and large engines. Second, this measure does not include the friction of the mechanical assemblies, including the high-pressure fuel and coolant pumps, therefore allowing a more direct comparison of the combustion processes. Third, this allows the one cylinder under test to be isolated. Eqn. 2.9 shows the calculation of IMEP from a pressure trace. Work is integrated from the point of Intake Valve Closing (IVC), through compression, through expansion, and to Exhaust Valve Opening (EVO). Work is divided by cylinder volume resulting in units of pressure.

IMEP is calculated as:

$$\text{IMEP} = \frac{1}{V_\text{d}} \int_{\text{IVC}}^{\text{EVO}} P dV \tag{2.9}$$

where V_d is the displacement volume of one cylinder, P represents instantaneous in-cylinder pressure, dV represents change in instantaneous cylinder volume, and IVC and EVO represent the crank angles corresponding Intake Valve Closing and Exhaust Valve Opening.

This 4-cylinder 4.5L engine, has ≈1.1L displacement per cylinder. As an order of magnitude comparison at an operating point representative of those presented in this thesis, at 4 bar IMEP the single 1.1L cylinder will receive fuel energy of E≈1100J, and do work of W≈420J resulting in a thermal efficiency of $\eta_{th} \approx 38\%$.

With reference to Fig. 2.11, the positive total work shows up as an asymmetry in the pressure trace. For the mid load point (IMEP=3 bar), pressure is increased after TDC and remains higher than the motoring trace as the combustion chamber expands (dV is positive). For the high load point, peak pressure is not as high as the low load point. However pressure is higher than the low load trace for points after ≈20 CAD, where dV is also high due to the motion of the piston and connecting rod, and pressure remains higher through the expansion stroke. The motoring trace is roughly symmetrical, however peaks slightly before TDC. This is due to loss of heat and/or mass from the cylinder, with the angle before TDC termed Thermodynamic

Loss Angle (see Subsection 2.7.3).

In order to create work, fuel is combusted. This increases the global temperature, increasing pressure. However the total of fuel energy is split between doing useful work on the piston, and losses such as discharge of hot exhaust gas. Heat is also lost through the cylinder wall, heating the coolant. The observed heat release, of the fuel combustion not corrected for wall heat losses, is termed Apparent Heat Release (AHR). Under the assumption of the cylinder contents being well-approximated by an ideal gas, the rate of heat release can be calculated via Eqn. 2.10. This equation is only valid under the assumption of negligible mass transfer in the cylinder, and thus is only calculated between IVC and EVO. With the rate of AHR represented by dQ_{AHR},

$$dQ_{\mathrm{AHR}} = \frac{\gamma}{\gamma - 1} PdV + \frac{1}{\gamma - 1} VdP \tag{2.10}$$

where γ is the specific heat ratio of the cylinder contents, P and dP are the instantaneous pressure and its derivative with respect to crank angle, and V and dV are the instantaneous cylinder volume and its derivative with respect to crank angle.

For this work, heat loss from the cylinder contents to the combustion chamber wall is estimated using the well-known Hohenberg Correlation developed for diesel engines [97]. This uses instantaneous exposed area multiplied by an instantaneous heat transfer coefficient which will depend on piston speed, temperature, and pressure. Temperature is calculated using the ideal gas law and measured cylinder pressure. While the literature notes some issues in using wall heat loss models developed for fossil fuels when measuring and simulating hydrogen combustion [104], the effect of the wall loss for this work is relatively small compared to the apparent heat release, and using existing and common models allows comparison with existing works.

With the rate of heat loss represented by dQ_w

$$dQ_{\mathrm{w}} = AC_1 V^{-0.06} P^{0.8} T^{-0.4} (v_{piston} + C_2)^{0.8} \tag{2.11}$$

where A represents the instantaneous total of area exposed to combustion, V is the instantaneous volume, P and T are the in-cylinder pressure and temperature respectively, v_{piston} is the velocity of the piston, and constants $C_1 = 130$ and $C_2 = 1.4$ are from literature where experiments were performed on an engine of similar size [97].

The pressure trace, as recorded, contains significant noise. High-pressure fuel injection and combustion also set up pressure oscillations within the cylinder (ringing). For integrated variables, such as IMEP, the integration will smooth out the noise. However where the derivative of pressure is used (such as when calculating heat release), noise and ringing can cause large errors. Fig. 2.12 shows the effect of these techniques on the pressure trace using the same IMEP=3 bar point as shown in Fig. 2.11. Without any signal processing, the heat release rate calculated for a single pressure trace shows large fluctuations and patterns are difficult to discern. Several cycles can be averaged to reduce the effect of uncorrelated noise. Each dual-fuel point is recorded for 200 cycles and the point is repeated 3 times, so 600 cycles are available to average. These results are also plotted in Fig. 2.12. The fluctuations are reduced, however cylinder ringing is still present. Cylinder ringing is suppressed with a Gaussian FIR filter [46] with cutoff frequency of 2.5 kHz. This is implemented as a non-causal filter, in post-processing, to avoid shifting the pressure trace. To obtain acceptable reduction of cylinder ringing the pressure trace is filtered, and where the derivitive is calculated this derivitive is filtered again.

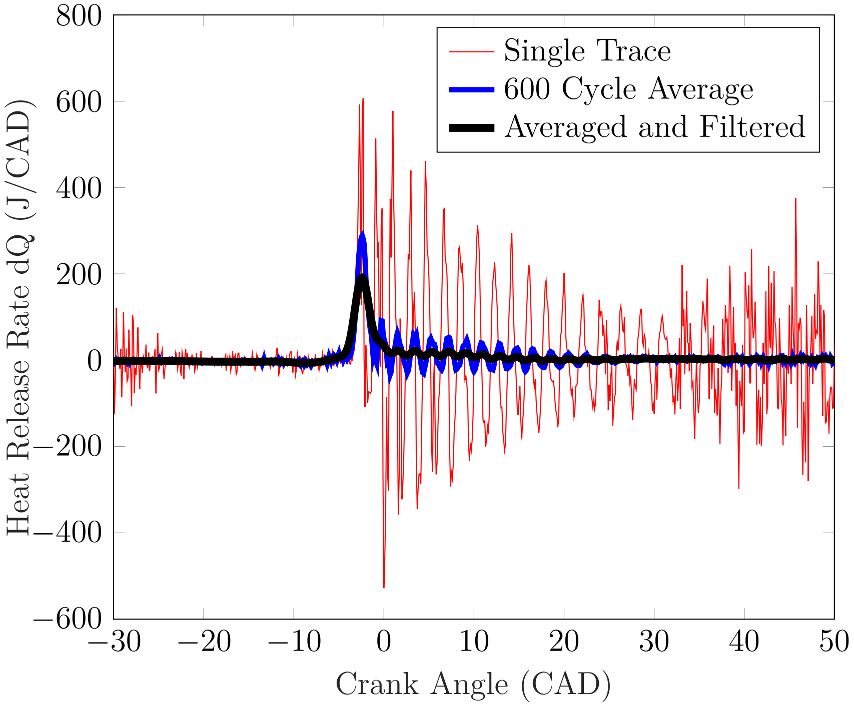

Figure 2.12: Heat Release Rate Showing Effects of Averaging and Filtering

A Gaussian filter was chosen to minimize overshoot and ringing artifacts caused by the filter. Other filter methods, for example Butterworth, can produce these artifacts for fast initial heat release rates [105]. In Fig. 2.13, an example heat release rate is generated by the sum of two Wiebe functions [106], tuned to produce a similar shape and duration to observed dual-fuel points. While the real heat release rates are never filtered (instead pressure data is filtered) this figure shows the effect of filtering artifacts. The output of a non-causal fourth-order Butterworth filter shows significant pre-ringing near -3 CAD, and post-ringing near 8 CAD. In comparison, the Gaussian filter smooths the transition to the fast initial heat release at 0 CAD and causes a slight lag at 6 CAD, but does not create ringing.

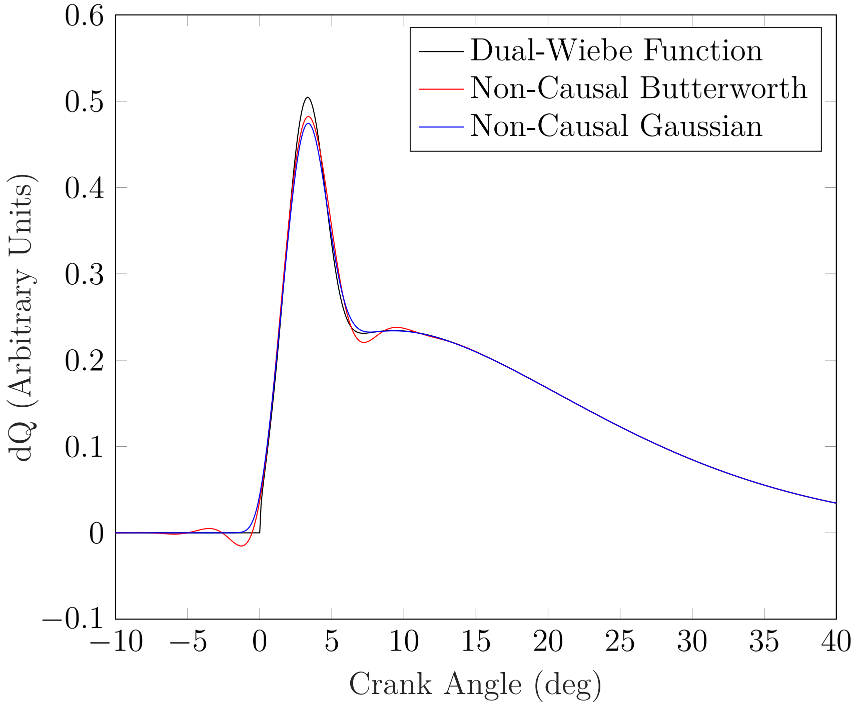

Figure 2.13: Effect of Different Filters Applied to a Modelled Heat Release Rate

MPRR is an important metric to quantify combustion speed, with high speed combustion increasing fluid shear and promoting heat transfer to the cylinder walls. This can lead to decreased thermal efficiency, hotspots and preignition [9, 44]. As MPRR is obtained by calculating the derivative of pressure with respect to crank angle, high-frequency noise is amplified and filtering is important. For this work, a moving-average filter is implemented in the FPGA module. The width of this filter is 4 samples (0.4 CAD). This suppresses high-frequency noise, while detecting the ringing shown in Fig. 2.11 and Fig. 2.12.

Cumulative heat release is calculated from the heat release rates calculated in Eqn. 2.10 and estimated in Eqn. 2.11.

With Q representing the total heat release in Joules,

$$Q = \int_{\mathrm{IVC}}^{\mathrm{EVO}} dQ_{\mathrm{AHR}} + dQ_{\mathrm{w}} \tag{2.12}$$

Where IVC and EVO represent the crank angles corresponding Intake Valve Closing and Exhaust Valve Opening, dQ_{AHR} refers to Apparent Heat Release Rate in Eqn. 2.10, and dQ_{w} represents estimated wall heat loss in Eqn. 2.11.

When calculating combustion metrics such as onset or end of ignition, a suitable threshold must be chosen. In this work, onset of ignition (and therefore ignition delay) is calculated based on the crank angle at which 10% of total heat release has occurred. The end of combustion is here defined as the crank angle where 90% of energy has been released.

Fig. 2.14 shows three normalized cumulative heat release curves calculated from dual-fuel operation at IMEP=4 bar and SOI=-4, with varying HES. These are a subset of points in Section 4.4 and Section 5.5. Fig. 2.14 corresponds to Fig. 5.12. For Fig. 2.14, the heat release from Eqn. 2.12 is further normalized into $\overline{Q}$. For each operating point, the minimum value of Q occurring after SOI is found, and the maximum value from this point to 60 CAD is found. The heat release is normalized based on this maximum and minimum resulting in $\overline{Q}$. For HES=55%, there is a phase of relatively fast initial heat release to approximately 55% (corresponding to the diesel energy fraction) followed by a slower phase. For HES=83%, there is a more constant heat release for the majority of the combustion. For both cases, near the end of combustion the heat release slows substantially. The 90% (CA90) point is chosen as a consistent threshold representing the main stages of heat release while being minimally affected by the slow late stage. In addition, the 10% threshold is chosen for the beginning of combustion, although it should be noted that there is some effect of early combustion speed on CA10. For this work, burn duration is calculated using these CA10 and CA90 thresholds.

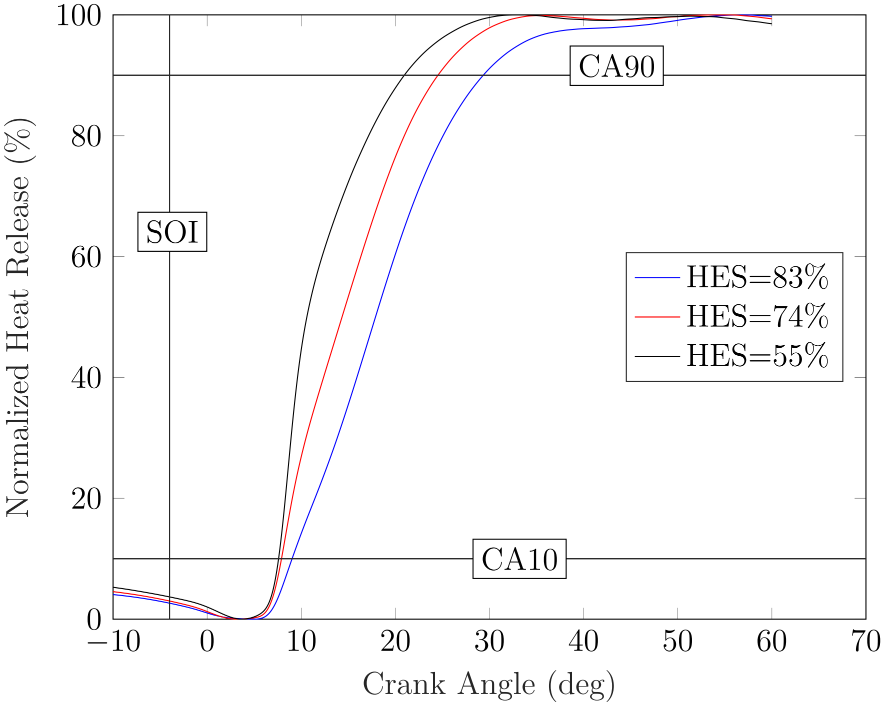

Figure 2.14: Normalized Cumulative Heat Release for IMEP=4, SOI=-4, and HES of 55%, 74%, and 83%

Chapter 3

Hydrogen Sensor[1]

3.1 Motivation

Hydrogen measurement has often been performed with large, expensive and fragile instruments such as mass spectrometers [82, 83] or gas chromatographs [108], with low-cost options often having cross-sensitivity issues [108–110]. Engine research can therefore benefit from a low-cost and rugged sensor. Further, a sensor that meets the needs of on-road production applications could find use in realtime diagnostics of dual-fuel engines in a transportation application. In this chapter, a commercial hydrogen sensor is bench-tested in detail using a high-accuracy flow rig to mix known calibration gasses in different proportions simulating engine exhaust. An overview of the sensor characterization testing performed in this chapter is given in Table 3.1.

3.2 Background

There are a great variety of methods used to quantify hydrogen concentration in gas mixtures [108, 111–113]. This topic is expected to become even more important with increasing usage of hydrogen in the economy [108, 111–113]. Although a commercial sensor is used here, choosing a sensing method that can operate with a reasonable sample rate, reliability relative to cross-sensitivities and soot contamination, and is commercially available is important to this project. Further, reducing expense and

---

[1] Elements of this chapter have been published at the 2025 CSME conference in Montreal [107].

Table 3.1: Overview of Sensor Characterization Tests

Subsection	Results	Gases Tested	Purpose
3.4.1	Fig. 3.3	H_2, O_2	Effect of low oxygen
3.4.2	Fig. 3.4	H_2	Span test
3.4.3	Fig. 3.5	H_2	Low range behavior
3.4.4	Table 3.4	H_2, CO_2, CO, UHC, O_2, NO	Screening test
3.4.5	Fig. 3.7	H_2, CO	CO cross-sensitivity
3.4.6	Fig. 3.8	CO_2, UHC, NO	Other Sensitivities
3.4.7	Table 3.6	H_2, CO	Simplified Model
3.4.8	Fig. 3.9	Engine Exhaust	Test with real engine exhaust

logistical constraints such as vibration resistance and size of equipment can be useful for potential future on-road sensing applications.

Exposure to hydrogen will change the physical properties of some materials. Palladium-Silver alloy will grow physically when exposed to hydrogen, an effect that was used to shift the wavelength response of a diffraction pattern thereby sensing gas concentration [114]. Highly-ordered structures made of Aluminum-doped Zinc Oxide nanotubes will shift their wavelength of minimum light reflectance on exposure to hydrogen [115]. Many other methods of using light interference to detect this small displacement exist [116]. However, these sensors were not commercially available. Further, there was concern about nanoscale optical methods not being resistant to the soot present in diesel engine exhaust.

Hydrogen can be adsorbed onto some metals, especially palladium, and change the work function of that metal [117]. In 1975, a Field Effect Transistor (FET) with hydrogen-sensitive gate using this effect was demonstrated [118]. Nickel has been used as the sensing element [119]. Chemosensitive FETs continue to be an active area of research for hydrogen sensing applications [120]. Although sensors with this method were not used for this work, this remains a promising technique.

In some materials, again including palladium, exposure to hydrogen causes an increase in electrical resistance due to changes in crystal structure [121]. Other materials such as titania nanotubes, grown by anodization of titanium, change resistance on exposure to hydrogen [122]. Change to the thermal resistance of semiconducting tin oxide has been used to quantify hydrogen with improved selectivity over some other methods [123].

Thermal conductivity of the gas mixture can also be used directly. Here, the different conductivity of hydrogen compared to most gasses can be used to quantify the proportion of hydrogen in a mixture with known components, for example mixtures of methane and hydrogen [108]. Speed of sound has been used to quantify hydrogen content in binary mixtures with known composition such as hydrogen-air [124]. However, the composition of engine exhaust includes varying concentrations of several main components including CO_2, CO, and possible unknown and trace compounds, and thus has too many degrees of freedom for either method to be used here.

Chromatography uses the partitioning of different sample components into a stationary and a mobile phase. When passed along a capilliary column, the components arrive at the end of the column at different times depending on how long they are slowed down by adsorption into the stationary phase [125]. These units tend to be large and high-maintenance [108] but work has been done to miniaturize these devices [126]. At the end of the column, the different components can be differentiated by several types of detectors. These operate on a variety of principles including chemiluminescence, ionization, and thermal conductivity. [125]. A gas chromatograph was used to confirm lack of hydrogen in diesel exhaust in Subsection 3.4.8. However the sample time, on the order of 20 minutes, make this device most useful for selective validation of results.

Mass Spectrometry operates by separating ions according to charge-to-mass ratio, after ionization of component molecules [127]. This process can be destructive to the molecules, and therefore the spectrum can include fragments of the original components. Mass Spectrometry has been used in studies to quantify hydrogen production from biomass burning [82] and engines [82, 83]. Although work has been done to miniaturize these historically large and high maintenance devices [128] this method was not used here.

Classic long-wave Fourier Transform Infra-Red spectroscopy is not suitable as hydrogen lacks absorption bands in the long-wave infrared region. However, Raman scattering using a 532nm incident wavelength has been used to quantify hydrogen in nitrogen mixtures [129].

Electrochemical sensors can be used to detect hydrogen. Amperometric sensors apply a voltage across an electrolyte and measure diffusion-limited current, typically linear to the concentration of measured gas over three orders of magnitude [130]. These can be high temperature such as an engine oxygen sensor or low temperature including for biomedical applications [130]. Potentiometric sensors act ideally at zero current, and measure electrochemical potential between the sense and reference electrode [108]. Electrochemical sensors can have a large cross-sensitivity, especially to hydrocarbons and carbon monoxide [108]. Parameters such as temperature can also have a large effect on the cross-sensitivity of solid oxide ampulemetric sensors [131]. This can be controlled by varying sensor parameters, for example to determine unburned hydrocarbon emissions [132] or ammonia slip from aftertreatment [133] using a commercial sensor originially manufactured for $\mathrm{NO_x}$ measurement.

Cross-sensitivity for electrochemical hydrogen sensors can be reduced by the use of a palladium [134] or fluorinated ethylene propylene (FEP) plastic [135] membrane to allow hydrogen into the sensor while keeping other gas molecules out. The choice of electrode/catalyst can affect cross-sensitivity [136]. Low-cost commercial hydrogen sensors can have cross-sensitivity to carbon monoxide of 4 times their sensitivity to hydrogen [109, 110]. Several commercial hydrogen sensors of the electrochemical and catalytic combustion type have been tested in the literature for CO cross-sensitivity [87].

Catalytic combustion sensors measure the heat generated by combustion of gas components on a catalyst surface [108, 111]. Using silicon thermopiles, a sensor with 1ppm detection limit has been reported [137]. These are often cross-sensitive to components such as CO, hydrocarbons and halogen-containing hydrocarbons and can be suceptible to catalyst poisoning [108], although some implementations have low cross-sensitivity [137]. Oxygen is required in the sample gas is in order to support the combustion reaction [108]. PTFE film can be used to increase resistance to catalyst poisoning [138] and filters or molecular sieves can be used to increase resistance to cross-sensitivity [108].

A commercial catalytic-combustion type sensor is chosen for further characterization as detailed in this chapter. After characterization, and correction for carbon monoxide concentration, this sensor will be used to measure hydrogen in dual-fuel exhaust.

3.3 Experimental Setup

A commercial catalytic-combustion sensor, RKI model 752-04 [139], is tested. Response and cross-sensitivity to gaseous components likely to be present in hydrogen-diesel dual-fuel exhaust is quantified. In Chapter 4 this sensor will be used to quantify unburned hydrogen emissions from an HDDF engine. The manufacturer specifies that there is neglegible cross-sensitivity to carbon monoxide, unburned hydrocarbon or nitrogen oxides [139] although this claim is tested for the higher levels present in raw HDDF engine exhaust. A minimum oxygen concentration of 8 vol% was specified for reliable measurement [140]. This sensor outputs a 0.5—4.5 volt signal, corresponding to an indicated hydrogen concentration by volume ($\mathrm{H2_i}$) of 0.0 to 4.0%. Thus the nominal sensitivity is 1V/H2%. In this chapter indicated hydrogen, $\mathrm{H2_i}$, is differentiated from actual gas concentration, $H2_g$.

To test the sensor for response to different gas mixtures, a flow rig setup capable of mixing up to 7 gasses at different ratios was used. This flow rig consisted of: seven mass-flow controllers, isolation valves, datalogging of sensor response by an Arduino microcontroller, and control/datalogging/configuration of the mass flow controllers using a PC running a Matlab Graphical User Interface (GUI) program. This setup is shown schematically in Fig. 3.1. This equipment has been described in prior literature [133], however the current work automated testing and datalogging of this equipment.

The mass flow controllers used and schematically depicted in Fig. 3.2 are MKS GE50 series. These controllers function on the thermal heat capacity measurement principle, and contain several preloaded calibration tables for different gasses [141]. To correct for gas mixtures not included with the factory calibration, the data is later corrected to account for actual heat capacity of the gas mixture vs assumed value. Seven controllers, ranging from 10,000 Standard Cubic Centimeter per Minute (SCCM) to 200 SCCM full-scale, are used in parallel. Each unit is rated to an accuracy of 1% of indicated flow, down to a minimum of 1% of full-scale [141]. Check valves are used on six of the gas streams to prevent backflow. The check valve is omitted on the lowest-flow stream due to concerns that the cracking pressure (1/3 PSI) of the check valve would cause bumping and inconsistent flow rate. A typical total flow rate used for these tests is 10,000 SCCM. The lowest flow used is 2 SCCM, which is used for hydrogen to determine the detection limit / deadband of the sensor. Depending on the test, inactive gas streams are isolated using motor-actuated ball valves.

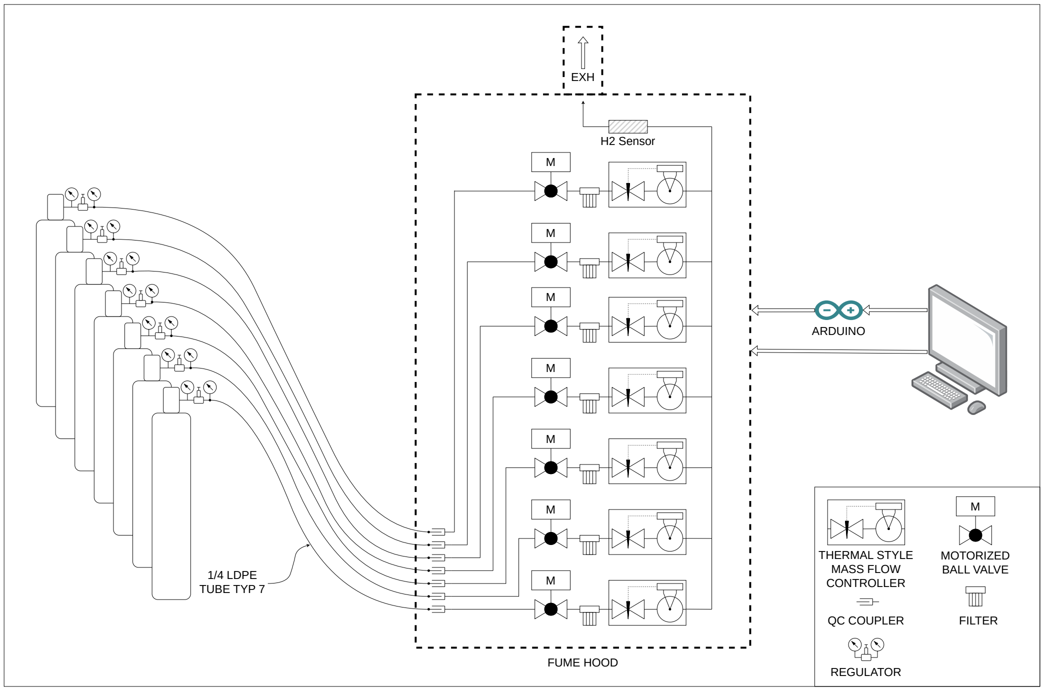

Figure 3.1: Schematic of Flow Rig

Overall control of the setup is through a custom Matlab-based GUI running on a Windows PC, which automatically runs multipoint testing. As the program runs, the PC sends Modbus commands over TCP/IP to the seven flow controllers. This Matlab program also communicates with an Arduino Mega, and uses the digital IO to open/-close motorized gas isolation valves. Configuration of the flow controllers is through a web (HTTP) interface separate from the Matlab program. Data acquisition from the flow controllers is via Modbus protocol over TCP/IP. The voltage output from the hydrogen sensor is measured using the Arduino. The Analogue-to-Digital Converter (ADC) present on the Arduino has 10-bit resolution and 5V range, corresponding to 5mV resolution. At the nominal scale factor of the sensor this corresponds to a resolution of 0.005 H2%. Isolation valve limit switch positions are also measured by the Arduino.

Before operating the equipment, a Matlab data structure is prepared. This contains information on the duration of each test point in seconds, and a vector corresponding to mass flow controller setpoints and isolation valve commands for each gas. At the end of a run, a data structure containing measured flow, setpoints, measured valve position, and hydrogen sensor response is saved to the PC. Each test point is held approximately 120 seconds to let the system reach steady state. Each test point is made up of approximately 30 measurements, and in subsequent analysis the last 10 are averaged. Recording all 30 points, including the transients, allows troubleshooting and confirmation that both the measured flow rates and sensor response has converged to a steady state. A typical response to a step change in hydrogen concentration setpoint is shown in Fig. 3.2, showing that this method allows time for the setup to reach steady state.

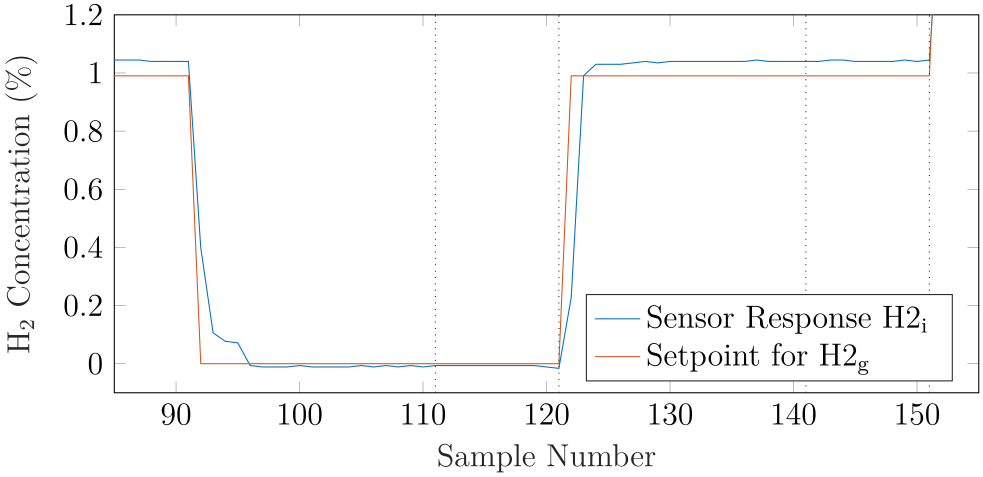

Figure 3.2: Hydrogen Sensor and Calibration Rig Transient Response. Ten Samples are Averaged for Each Operating Point, Between Samples 111–121 and 141–151

In initial testing, noise was observed at the hydrogen sensor output. In operation, a sawtooth wave of approximately 30mV (corresponding to 0.03% H2) at about 20 kHz was superimposed on the signal. To remove this, a single-pole RC lowpass filter was added to the sensor output, designed to suppress this signal to <1mV. This filter was in place for all testing whether using calibration gas or engine exhaust, and thus the sensor is considered calibrated as a unit inclusive of this filter.

Several gases were considered for testing cross-sensitivity, according to how likely they are to be in hydrogen-diesel dual-fuel exhaust and how likely they are to affect the sensor readings. The list of test gasses is presented in Table 3.2. Carbon monoxide is well-known to affect some catalytic sensors [87, 108–111] and is included for testing. There is a potentially large and variable amount of carbon dioxide present in both diesel-only and HDDF exhaust due to the injected diesel fuel. Hydrocarbons are known to affect some catalytic sensors [108, 111]. These are present in dual-fuel exhaust to varying degrees [41, 42, 142, 143]. Here, a mixture of propane diluted in nitrogen is used to represent these emissions. Nitrogen oxides are also present in dual-fuel exhaust in varying amounts [40, 41]. Here, a mixture of 1.96% Nitric Oxide in N_2 is used to represent NO_x emissions. Catalytic combustion sensors are well-known to be affected by oxygen concentration [108]. Pure oxygen is mixed into the other gasses at an appropriate ratio to simulate oxygen-depleted engine exhaust.

Table 3.2: Hydrogen Sensor Calibration Gases

Rack Position	Emission Type	Composition[a]	Accuracy[b]
1	Diluent Gas	100% N_2	99.95% Min
2	CO_2	100% CO_2	99.9% Min.
3	UHC	5060ppm C_3H_8, bal N_2	2% Rel.
4	O_2	100% O_2	99.6% Min.
5	CO	9%CO, 45%CO_2, bal N_2	1% Rel.
6	NO_x	1.96% NO, bal N_2	2% Rel.
7	H_2	100% H_2	99.95% Min.

[a] Volume Basis.

[b] Per Manufacturer.

3.4 Sensor Testing Results

3.4.1 Oxygen Depletion

Catalytic type sensors are affected by oxygen concentration [108]. This sensor is rated to give a correct reading between 8–20% oxygen, but is not rated to function properly under 8% oxygen [140]. Engine exhaust can contain varying amounts of residual oxygen. This sensor is tested at constant hydrogen concentrations and varying oxygen levels, with results presented in Fig. 3.3.

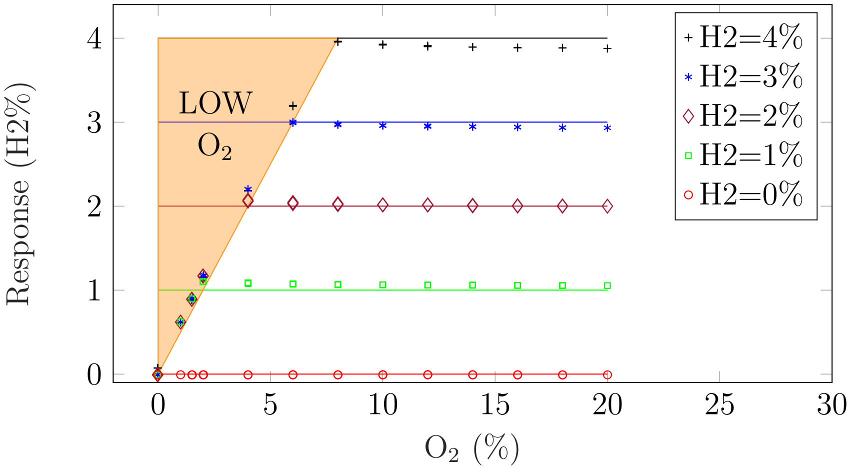

Figure 3.3: Sensor Output Dependence on Oxygen Level at Different Hydrogen Concentrations

Oxygen depletion affects the output of this sensor. Lower concentrations (such as H2=1%) will report correctly even at relatively low (H2=2%) oxygen. Higher hydrogen concentrations require more oxygen to report correctly. A lack of oxygen will cause the reading to be limited to a low value, depending on the oxygen level. This effect can be seen in the highlighted region of Fig. 3.3 labelled as "Low O_2". An oxygen concentration of approximately half the hydrogen concentration is required for accurate reporting, which may be related to the stoichiometry of hydrogen combustion. Also, near the point of oxygen starvation, the sensor slightly over-reports the hydrogen value compared to full-oxygen points. As oxygen level increases, the reading converges to a constant value.

With $\mathrm{H2_i}$ being the indicated hydrogen (sensor output),

$$\mathrm{H2_i} = \max(\frac{\mathrm{O_2}}{2}, \mathrm{H2_g}) \tag{3.1}$$

where $\mathrm{H2_i}$ is indicated hydrogen concentration, $\mathrm{O_2}$ is the oxygen concentration, and $\mathrm{H2_g}$ is actual gas concentration of hydrogen.

The purpose of testing this sensor, is for use in measuring hydrogen in dual-fuel exhaust. Studies have found peak exhaust emissions of H2exh=1% [62] and H2exh=2.5% [16] per volume. Within the range of 0—3% $\mathrm{H_2}$ and 8—20% $\mathrm{O_2}$, the results are promising for use in engine exhaust measurement. In this region, RMS error is ±0.040% and maximum error is +0.069%. Within the full-scale range of 0–4% $\mathrm{H_2}$, the error is slightly greater however this concentration is unlikely to be present in HDDF engine exhaust [16, 62].

3.4.2 Full-Scale Hydrogen Response

Fig. 3.4 shows the response of the sensor to hydrogen concentrations from zero to full-scale (4%). At all points, 17% oxygen is available for the catalytic reaction to take place. This sweep is performed once increasing hydrogen, and once decreasing to give an idea of any sensor or setup hysteresis. In common with all flow bench tests here, each point represents the average of 10 samples over ≈40 seconds.

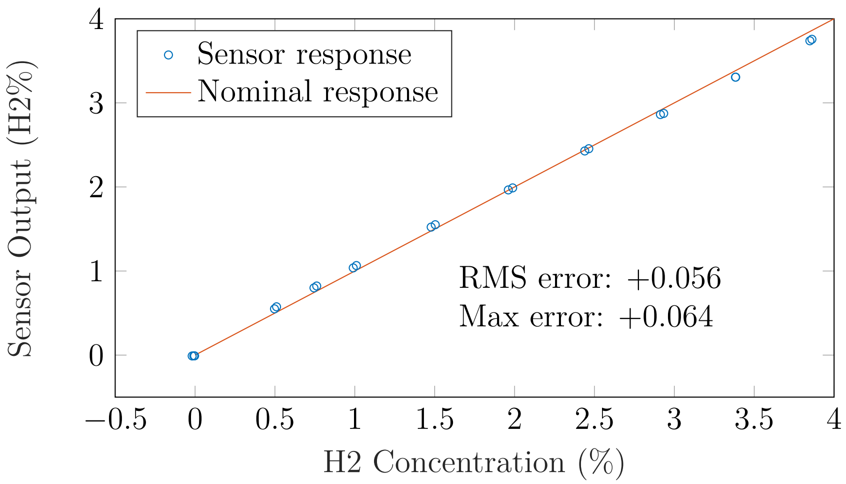

Figure 3.4: Sensor Output Response to H2 Concentrations across the range of $H2_g$= 0–4% with O_2=17%. Ideal response of $H2_i = H2_g$ and error relative to ideal response also shown for comparison.

Hysteresis is not evident, data points at similar hydrogen concentrations cluster closely together. Some non-linearity is present, evidenced by an S-shape to the sensor response. A linear-least-squares regression results in a response of 0.9640 H2%/H2% and output offset of 0.0595 H2%. Inverting this relationship results in Eqn. 3.2.

With $H2_g$ being actual gas concentration,

$$H2_g = 1.037H2_i - 0.0617 \tag{3.2}$$

where $H2_i$ is indicated or reported concentration.

These results can also be compared to the ideal response of $H2_g = H2_i$, and the slope and offset included in the error. This results in an RMS error of 0.056 H2%, and maximum absolute error of 0.064 H2%. This is similar to the RMS and maximum errors obtained in the test on oxygen depletion (Fig. 3.3).

3.4.3 Low Range H2 Response

Hydrogen was added over a range of 0—50 SCCM, with nitrogen and oxygen added to obtain a total flow of 10,000 SCCM and O_2=14%. The controller would only accept setpoints of 3 SCCM or higher, corresponding to $H2_g$=0.03%, or a setpoint of zero. The flow measurement accuracy is rated to 1% of reading. ADC resolution is 10-bit, resulting in resolution of $H2_i$ being 0.005 H2%. Ten voltage measurements are averaged at each point. A check valve is not installed on the hydrogen line to reduce bumping, where a check valve opens intermittently, due to the low flows of hydrogen used. Fig. 3.5 shows the sensor response to 0–0.5% H2 at a constant oxygen level of 14%. At zero, the sensor outputs approximately zero as expected. At higher concentrations, a linear response of $H2_i = 0.926H2_g + 0.051$ was observed, showing a positive offset which is inconsistent with the zero hydrogen point outputting zero. Thus at low hydrogen concentrations, a significant nonlinearity is observed.

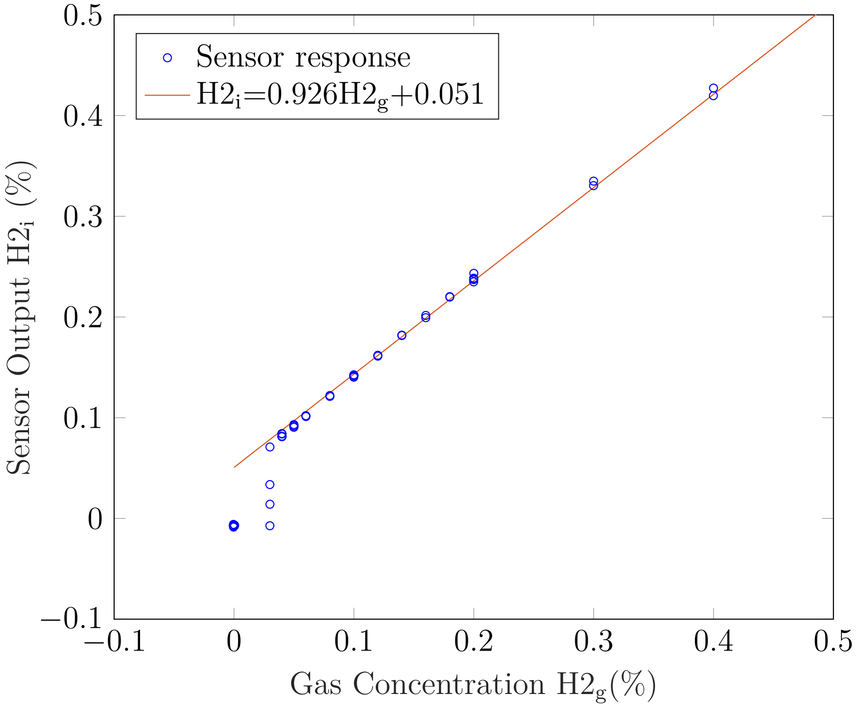

Figure 3.5: Sensor Response to Low Concentrations of Hydrogen

At the lowest non-zero hydrogen concentration, different tests take on values between zero and 0.07%. At this hydrogen concentration, the sensor varies between outputting 0.07% and zero during the testing. Because each test point consists of the average of 10 instantaneous readings over approximately 40 seconds after the flow has reached steady-state, the average values plotted in Fig. 3.5 can take on intermediate values. Review of the data showed that no instantaneous measurements between 0–0.047% were recorded. This 0–0.047% range is 10 ADC counts, so ADC resolution is not believed to be a factor. This gap in output values is believed to reflect the presence of an output deadband, where small output values are reported as zero.

While this data is taken at the low-flow limit of the hydrogen flow controller, both Fig. 3.4 and Fig. 3.5 show a small offset error. The repeatable and near-perfect zero is therefore an outlier, leading to the conclusion that values under $H2_g \approx 0.047\%$ are reported by the sensor to zero.

3.4.4 1- and 2-Factor Cross-Sensitivities

A 2-factor screening test was performed to test response to 6 species and 2-factor combinations thereof. The concentration of hydrogen, oxygen, and four other gasses, was varied while the total flow rate was held constant by adding nitrogen. The concentration of each factor was varied as high or low with levels defined in Table 3.3. Although a 2-level design cannot account for a nonlinear response to any individual factor, this was deemed acceptable for this screening test, as only oxygen depletion and low output ranges exhibited marked nonlinearity and levels are chosen to avoid these regions. Each combination of H2, CO_2, CO, UHC, O_2 was tested. The test was then repeated in the presence of NO_x. Six replicates were performed, for statistical significance and to gauge setup repeatability.

High and low ranges of each factor were chosen to be large relative to normal dual-fuel engine operation, while still respecting the limits of the equipment and sensor. The low value of hydrogen, present as a minimum at all points, is 0.1% to avoid the deadband behavior reported in Subsection 3.4.3. The high level was chosen to be representative of typical exhaust emissions [61] rather than the full scale range of the sensor. Likewise there is a minimum of 9% oxygen to avoid nonlinear behavior as reported in Fig. 3.3, with the high O_2 range of 17% corresponding to low load diesel

Table 3.3: H2 Sensor Cross-Sensitivity Screening Test Levels

Variable	Factor	Level (hi)	Level (lo)
X_1	H_2	0.1%	1.6%
X_2	CO	0ppm	2000ppm
X_3	CO_2	1%	11%
X_4	UHC	0ppm	1000ppm
X_5	O_2	9%	17%
X_6	NO	0ppm	3000ppm

or dual-fuel operation. Carbon monoxide varies from 0–2000ppm. The test gas for CO also contains carbon dioxide, and therefore any point with high CO must have high CO_2. The low range of CO_2 is set above this value, and pure CO_2 added to keep this low level constant across tests. The CO_2 high level is consistent with, and in fact exceeds, the limits encountered by setting a minimum oxygen requirement. This CO_2 high limit is near stoichiometric combustion of C_nH_{2n} and could never be encountered with 9% atmospheric oxygen remaining especially when hydrogen is added. Nitric Oxide is added from 0–3,000 ppm, and propane is added from 0–1,000 ppm to represent unburned hydrocarbon emissions from 0–3,000 ppm on a carbon basis. High and low ranges for this test are summarized in Table. 3.3.

One outlier was found. This is an outlier not only in the data but within the 6 replicates, as shown in Fig. 3.6. This was removed from the dataset.

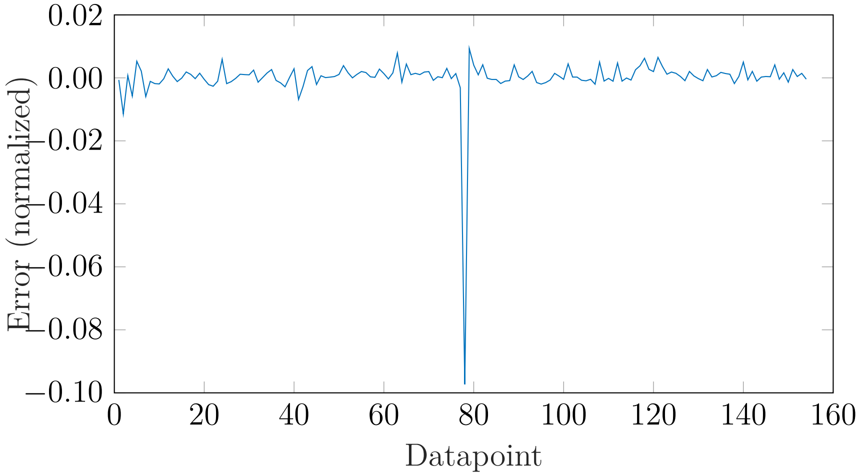

Figure 3.6: Hydrogen Sensor Screening Test Error Plot Showing Outlier (Removed for Following Analyses)

A multivariable linear model was created, considering interaction effects between any two variables. With the normalized sensor output represented by $\hat{Y}$,

$$\hat{Y} = a_0 + \sum_{i=1}^{6} a_i X_i + \sum_{i=1}^{6} \sum_{j=i}^{6} a_{ij} X_i X_j \quad \forall j > i \tag{3.3}$$

where a_i represents the model coefficients found in Table 3.4 and X_i and X_j represent gas concentrations after being normalized to the ranges in Table 3.3.

The offset term, in real H2%, is 0.045% which is similar to Fig. 3.5. The coefficient for hydrogen response, a_1=0.967, is close to the expected value of unity and similar to that obtained in Fig. 3.5. Confidence interval (95%) for each coefficient is presented as well as statistical significance of regression (P-value).

In Table 3.4 many of the model terms have large P-values, indicating low significance. Also, many terms are of a magnitude that can be ignored. A coefficient of 0.003 represents a difference in sensor response of 0.0045%, under the measurement resolution. Those that are significant at $P < 0.05$ and $a_n > 0.003$ are: Offset, H_2, CO, H_2-CO_2, H_2-UHC, H_2-O_2, and H_2-NO_x.

Table 3.4: Screening Test Model Coefficients (Normalized)

Model Coefficients	Meaning	Value (Normalized)	Confidence (95%)	P Value
a_0	$\overline{\text{Offset}}$	+0.030	±0.001	0.000
a_1	$\overline{\text{H2}}$	+0.967	±0.002	0.000
a_2	$\overline{\text{CO}}$	+0.047	±0.002	0.000
a_3	$\overline{\text{CO2}}$	-0.002	±0.002	0.008
a_4	$\overline{\text{UHC}}$	-0.000	±0.002	0.406
a_5	$\overline{\text{O2}}$	-0.001	±0.002	0.279
a_6	$\overline{\text{NO}}$	-0.003	±0.002	0.001
a_{12}	$\overline{\text{H2}}$-$\overline{\text{CO}}$	-0.003	±0.004	0.050
a_{13}	$\overline{\text{H2}}$-$\overline{\text{CO2}}$	-0.010	±0.003	0.000
a_{14}	$\overline{\text{H2}}$-$\overline{\text{UHC}}$	+0.007	±0.003	0.000
a_{15}	$\overline{\text{H2}}$-$\overline{\text{O2}}$	-0.008	±0.003	0.000
a_{16}	$\overline{\text{H2}}$-$\overline{\text{NO}}$	+0.021	±0.002	0.000
a_{23}	$\overline{\text{CO}}$-$\overline{\text{CO2}}$	-0.002	±0.004	0.106
a_{24}	$\overline{\text{CO}}$-$\overline{\text{UHC}}$	-0.001	±0.004	0.336
a_{25}	$\overline{\text{CO}}$-$\overline{\text{O2}}$	-0.000	±0.004	0.426
a_{26}	$\overline{\text{CO}}$-$\overline{\text{NO}}$	+0.001	±0.002	0.218
a_{34}	$\overline{\text{CO2}}$-$\overline{\text{UHC}}$	+0.000	±0.003	0.393
a_{35}	$\overline{\text{CO2}}$-$\overline{\text{O2}}$	-0.000	±0.003	0.371
a_{36}	$\overline{\text{CO2}}$-$\overline{\text{NO}}$	+0.000	±0.002	0.477
a_{45}	$\overline{\text{UHC}}$-$\overline{\text{O2}}$	+0.000	±0.003	0.443
a_{46}	$\overline{\text{UHC}}$-$\overline{\text{NO}}$	-0.001	±0.002	0.260
a_{56}	$\overline{\text{O2}}$-$\overline{\text{NO}}$	-0.000	±0.002	0.472
RMS error	+0.002	(Normalized Units)		
Max error(-)	-0.012	(Normalized Units)		
Max error(+)	+0.009	(Normalized Units)		

3.4.5 CO Cross-Sensitivity

Cross sensitivity of some types of catalytic sensors to carbon monoxide is well known [87, 108], although there are some catalytic sensors that have low cross sensitivity [137]. Per Coefficient a_2 in Table 3.4, the largest cross-sensitivity of this sensor is to carbon monoxide. As this compound is often present in diesel dual-fuel exhaust, further detailed testing was performed. Calibration gas containing carbon monoxide, was added to vary CO concentration from 0–3500 ppm while hydrogen concentration was fixed at four different concentrations of 0.1, 0.5, 1, 2, and 4%. Similarly to the screening test, the minimum hydrogen concentration is 0.1% to avoid nonlinearity at extremely low output values (Fig. 3.5). Testing was carried out at a constant 14% oxygen concentration. The difference in sensor reading at each constant hydrogen level, relative to the no-CO case, is presented versus CO concentration input in Fig. 3.7.

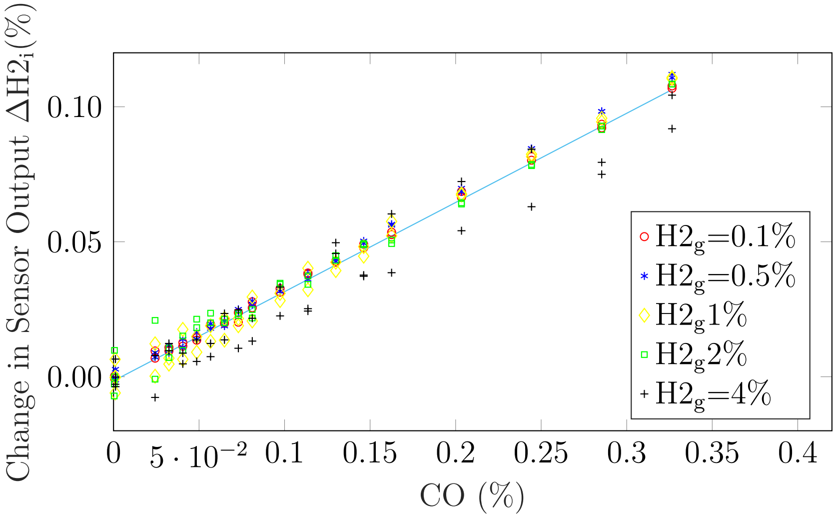

Figure 3.7: CO Sensitivity at Different Hydrogen Amounts, O_2=14%, CO_2:CO Ratio of 5:1, Line Shows Regression for All $H2_g$ per Table 3.5

An approximately linear response is observed for all tested CO and H2 levels. Linear regression was performed on the data, with the slope of sensor H2 response relative to CO concentration listed for each hydrogen concentration in Table 3.5. While cross-sensitivity is present, it is limited to just over 0.1% H_2 at 3500ppm CO.

Table 3.5: CO Cross-Sensitivity at Different H_2 Concentrations Using Varied Amount of 9%CO + 45% CO_2 Calibration Gas

H_2 Constant (%)	CO Slope (H2%/CO%)	CO Slope Confidence (95%)	CO Slope P-Value	Offset (H2%)	Offset Confidence (H2%)	Offset P-Value
0.1	0.331	±0.004	0.000	0.000	±0.001	0.049
0.5	0.347	±0.004	0.000	-0.001	±0.001	0.001
1	0.345	±0.013	0.000	-0.003	±0.002	0.001
2	0.323	±0.014	0.000	0.000	±0.002	0.358
4	0.306	±0.026	0.000	-0.003	±0.004	0.047
All	0.330	±0.008	0.000	-0.002	±0.001	0.004

For potential on-road applications, where CO levels as high as 3500ppm are not expected, the error generated by CO cross-sensitivity may be negligible. For research use, the readings will be corrected for CO concentration.

3.4.6 Sensitivity to UHC, CO_2, NO, and H_2-NO_x Interaction

To further confirm a lack of sensitivity to UHC, CO_2, and NO, further testing was performed where the concentration each of these components was varied across a range that is representative of HDDF combustion. A consistent concentration of 0.1% H_2 is present to avoid sensor nonlinearities at low output values as observed in Subsection 3.4.3. NO is varied 0–3500ppm, CO_2 0–15%, and UHC is again represented by 0–1000ppm propane.

The change in sensor output, $\Delta H2_i$, is plotted in Fig. 3.8. Response of $\Delta H2$ to UHC is slightly positive, but without discernible trend and always within 0.005%. The response of $\Delta H2$ to CO_2 shows a slight downward trend except for the last point, but again the maximum response is considered negligible for the present research. The response of $\Delta H2$ to NO_x at high hydrogen appears to go have a slight upward trajectory while at low hydrogen having a slight downward trajectory indicating the presence of a small, positive H_2-NO_x interaction. However the difference between maximum and minimum is only 0.025 H2% at 3500 ppm NO_x. This is considered negligible for the present dual-fuel engine application. Also, in the HDDF test results, high NO_x is never observed simultaneously with high unburned hydrogen.

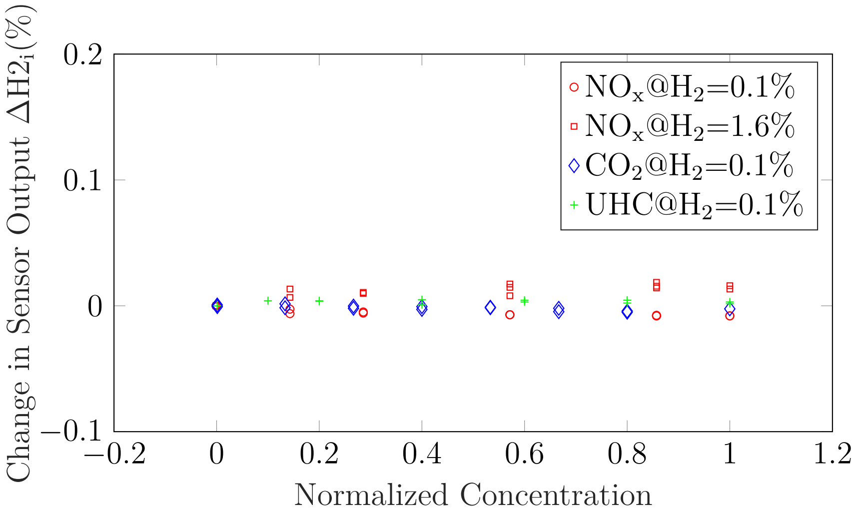

Figure 3.8: Cross Sensitivities to NO, CO_2 and UHC

3.4.7 Simplified Linear Model

Table 3.6: H_2 Sensor Reduced-Order Model Coefficients (Normalized)

Model Coefficients	Meaning	Value (Normalized)	Confidence (95%)	P-Value
a_0	$\overline{\text{Offset}}$	+0.028	+/-0.001	0.000
a_1	$\overline{H_2}$	+0.975	+/-0.002	0.000
a_2	$\overline{CO}$	+0.047	+/-0.003	0.000
RMS error	+0.006	(Normalized Units)		
Max error(-)	-0.024	(Normalized Units)		
Max error(+)	+0.019	(Normalized Units)		

Of the cross-sensitivities and interaction effects tested, only that of CO cross-sensitivity is significant to the present application of hydrogen measurement in dual-fuel exhaust. A simplified linear model was fit to the same data as the more complex model in Subsection 3.4.4. This simplified model takes into account only sensitivity to H_2, sensitivity to CO, and offset. Again data is normalized to the values in Table 3.3.

With $\overline{\mathrm{H2_i}}$ representing the normalized sensor response,

$$\overline{\mathrm{H2_i}} = a_0 + a_1\overline{\mathrm{H2_g}} + a_2\overline{CO} \tag{3.4}$$

where a_0, a_1, and a_2 are model coefficients found by regression, $\overline{\mathrm{H2_g}}$ is the normalized true hydrogen concentration, and $\overline{CO}$ is normalized CO concentration.

Model coefficients given in Table 3.6 are normalized to the values in Table 3.3. Offset is thus 0.042 H2%, response to hydrogen is 0.975 H2%/H2%, and CO sensitivity is 0.392 H2%/CO%. The RMS model error of 0.009 H2%, and greatest deviation of 0.036 H2%, is considered acceptable for the present HDDF exhaust measurement application.

3.4.8 Cross-Sensitivity to Real Engine Exhaust

This sensor has been comprehensively tested for hydrogen response and 5 potential cross-sensitivities. However, real engine exhaust can contain a wide variety of compounds [144].

As a baseline, the engine was run with diesel only and no added hydrogen. Two exhaust samples with high CO content were collected and analysed using Gas Chromatography (GC). Each sample was run through the GC twice. One operating point used diesel injection duration and timing that mimicked a stock ECU, but a restrictor plate on the inlet that reduced manifold pressure to ≈0.5 bar to promote incomplete combustion producing 4600ppm CO. The second operating point used diesel SOI=-30 and no restrictor, producing 1100ppm CO. No hydrogen was detected by the gas chromatograph at either of these points, and thus this engine is assumed to produce no hydrogen in the exhaust when operated in diesel-only mode and operating points similar to the above.

The HDDF engine was then operated at several diesel-only operating points, with no hydrogen fuel added. This operation produced varying levels of CO. Exhaust was cooled using an ice bath as described in Chapter 2. The sensor response relative to measured the CO level is plotted in Fig. 3.9. The linear model in Table 3.6 is also plotted, with the assumption of ($H2_g$=0). At low CO levels, the sensor output ($H2_i$) is zero (see Subsection 3.4.3). Where $H2_i$ >0.047%, the data behaves similarly to the linear model.

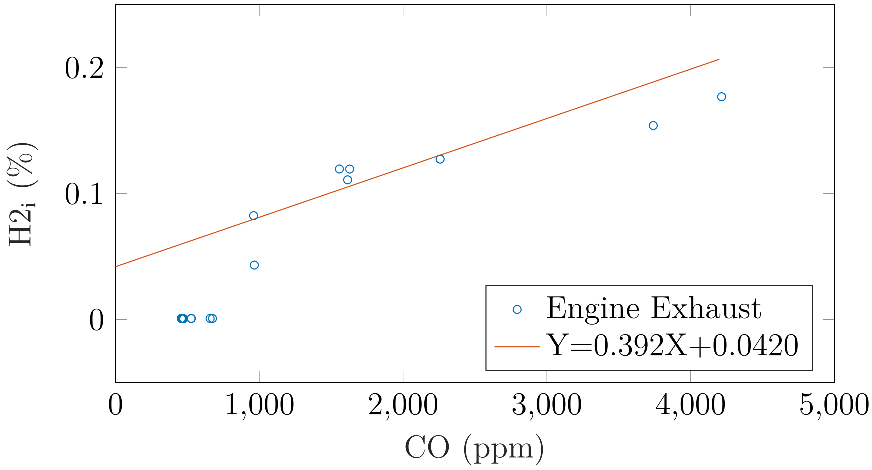

Figure 3.9: Response of Sensor to Real Diesel Exhaust

The points where $H2_i$ >0.047% were compared to the model in Table 3.6, which predicts a cross-sensitivity of 0.392 H2%/CO% plus offset. RMS error is under 0.02 H2%, showing good correlation.

Table 3.7: Real Engine Exhaust vs Sensor Model

RMS Error (H2%)	0.0194
Max Error(+) (H2%)	0.0346
Max Error(-) (H2%)	-0.0165

3.5 Chapter Summary

Measurement of hydrogen in the presence of other gasses can be achieved by many different methods, and this field remains an area of active research. A commercial hydrogen sensor, RKI 752-04 which is based on the catalytic oxidation method, was comprehensively tested for response to hydrogen and cross-sensitivity to other gases.

A high-accuracy flow rig, able to mix 7 gases at arbitrary ratios, was automated to perform tests without user intervention and according to a pre-calculated experimental design. This rig was used to determine response to hydrogen and 5 other gasses likely to be present in dual-fuel engine exhaust.

For $H2_g$= 0–4%, comparing the output of this sensor to input concentration $H2_g$ shows an RMS error 0.056 H2%. This sensor also exhibits deadband, where sensor output values $H2_i$ >0.047 H2% are set to zero. Due to the catalytic combustion operating principle, a minimum oxygen concentration is required for accurate reading. This minimum is dependent on the hydrogen concentration. Within the range O_2=8–20% and H2=0–3%, the RMS error of sensor output vs actual hydrogen concentration is 0.040 H2%.

A 2-level, 6-variable linear model with interaction effects found that many cross-sensitivities and interactions were not significant ($P<0.05$) or of a magnitude that is potentially negligible for the present engine research. However, cross-sensitivity to CO was observed. Using the same data, a linear model of reduced complexity was fit. This included only sensor span, CO cross-sensitivity, and an offset. This simplified model achieved RMS error of 0.009 H2%, with normalized model coefficients given in Table 3.6.

Carbon monoxide sensitivity, while significant for the present research, might not preclude the use of this sensor in on-road diagnostic applications. Exhaust concentrations of CO from an HDDF vehicle are expected to be lower than the values tested here, especially if the sensor is used post-aftertreatment for example to diagnose catalyst efficiency in removing hydrogen slip. This would mean that this sensor can be used without correction for CO levels.

This RKI sensor was then used to measure real diesel engine exhaust, under the tested assumption of zero hydrogen in the exhaust. Of the points where sensor response was above the sensor deadband, the error between the simplified linear model and sensor response was under 0.02 H2%.

Based on the testing completed, the RKI 752-04 sensor is suitable for use for measurement of unburned hydrogen in engine exhaust. This will allow for evaluation of the amount of hydrogen slip in dual-fuel or 100% hydrogen engine exhaust, which can be an important contributor to total greenhouse gas emissions. This low-cost sensor is portable and with a minimum oxygen concentration could be used to monitor engine out hydrogen emissions as this technology is developed and deployed to the market.

Chapter 4

HDDF Engine Testing Results[1]

4.1 Overview of HDDF Testing

This chapter is divided into several parameter sweeps according to the parameter varied. A single diesel injection is used throughout as shown in Fig. 2.5. Three engine parameters are varied: start of diesel injection (SOI), duration of diesel injection (DOI), and hydrogen intake concentration (H2int). Engine outputs include hydrogen concentration in exhaust (H2exh), Indicated Mean Effective Pressure (IMEP), and Maximum Pressure Rise Rate (MPRR). Inputs and outputs are shown schematically in Fig. 2.7. Equivalent CO_2 emissions (CO2eq), including the effect of hydrogen slip, are calculated using Eqn. 2.7.

Unburned hydrogen emissions are strongly dependent on H2int, and secondarily dependent on SOI. In Section 4.2, DOI is held constant, SOI is held constant to one of four values, and H2int is varied.

In Section 4.3, SOI is varied while DOI is kept at the same value as Section 4.2 and H2int is held constant to 5 vol% or to 8.3 vol%.

Section 4.4 presents 4 and 6 bar IMEP points, and Section 4.5 extends the operation down to 3 bar IMEP.

Section 4.6 examines engine operation at maximum HES points. DOI is held

---

[1] Elements from Section 4.2 and Section 4.3 have been presented at the 2024 conference of the Combustion Institute - Canadian Section [145].

constant at the minimum reliable injector energization duration. H2int is varied to keep IMEP at a constant 2,3,4,or 6 bar while SOI is swept.

A summary of chapter sections is shown in Table 4.1, with the parameters held constant and varied in each controlled experiment.

Table 4.1: Dual-Fuel Engine Testing Overview

Section	H2int	DOI	SOI	HES	IMEP
4.2	Swept	0.23 ms	-4,-14,-24,-34 CAD	–	–
4.3	5%, 8.3%	0.23 ms	Swept	–	–
4.4	–	–	-4,-14,-24,-34 CAD	Swept	4, 6 bar
4.5	–	–	-4,-14,-24,-34 CAD	Swept	3 bar
4.6	–	0.17 ms	-4,-9,-14,-19,-24,-29 CAD	Maximized	2,3,4,6 bar

4.2 Hydrogen Equivalence Ratio Sweep

Several studies in the literature have identified fuel-air ratio to be an important factor affecting unburned hydrogen emissions from internal combustion engines [16, 45, 62]. In a spark-ignited hydrogen engine, as ϕ increased from 0.1–0.2, H2exh decreased from 2.5–0.5% [16]. Spark timing was not specified. In a diesel engine supplemented with hydrogen and operated at 10% load, H2exh increased to 1.4% as H2int was increased from 0–4.5%. Further addition up to H2int=6.5% reduced H2exh [62]. When the diesel engine was operated at higher loads, peak H2exh was lowered. In another study with a diesel engine supplemented by hydrogen, combustion efficiency of hydrogen varied 93–98% as H2int was varied 1–6% [45].

H2int, the amount of hydrogen fuel in the cylinder, was swept 2–11%. DOI, the diesel injection duration, was kept constant at 0.23 ms. This corresponds to approximately 5 mg of diesel fuel, and is near the minimum reliable injection amount with this engine's stock injectors. SOI was held to four different values, namely SOI=-2, SOI=-12, SOI=-22, and SOI=-27. These are bounded in both directions by misfire. In operation, it was observed that the point of misfire is dependent on H2int (higher hydrogen percentage could not tolerate early or late injection, compared to low hydrogen points) and on diesel injection amount (larger diesel injection would allow a greater range of injection timing). When misfire occurred, this often created a flammable mixture that lit off in the exhaust, at which point the hydrogen flow was stopped for safety. Dependent on the test, the engine produced an IMEP in the range of approximately 0–5 bar. For this sweep on H2int, each point is held for 400 cycles to allow the gas analysis equipment to reach steady state, and Maximum Pressure Rise Rate (MPRR) is averaged over the last 50 cycles of each point. Test points are performed in random order to confound any coupling effects with prior test points.

Fig 4.1 shows the measured concentration of hydrogen in the exhaust as a function of H2int. For H2int>7%, H2exh is insensitive to SOI. However within the range of H2int=2–7%, H2exh is sensitive to SOI. Within this region of H2int=2–7%, SOI=-2 results in the highest H2exh compared to other injection timings. For SOI=-2, H2exh peaks at 2.5% at H2int=4.5%. This exhaust concentration means that over half of the hydrogen fuel remains unburned. For SOI=-12, H2exh is lower and the peak is shifted left to H2int=2.5%. Of the four values of SOI studied, the least slip occurs for SOI=-22. Further advancing injection to SOI=-27 increases H2exh. The overall behavior of a peak in H2exh near H2int=3–5% is replicated in further sections.

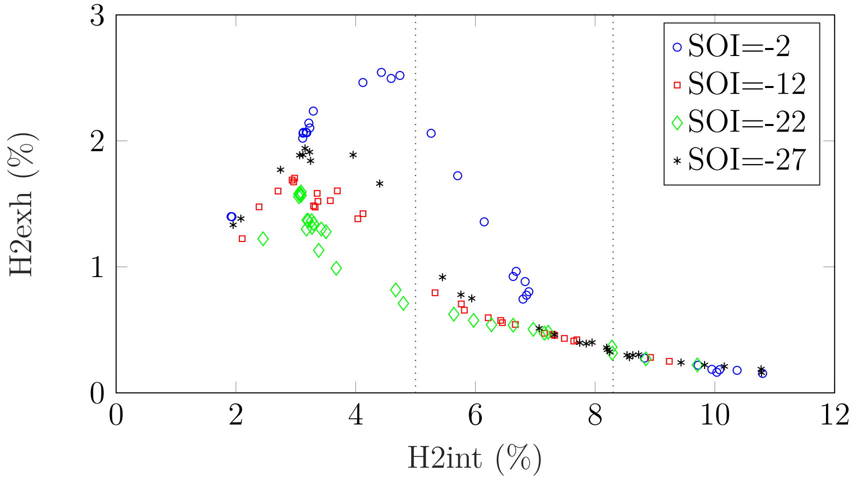

Figure 4.1: H2exh vs H2int with DOI=0.23ms and SOI={-2,-12,-22,-27}. Dotted lines indicate values of H2int used in Fig. 4.3 and Fig. 4.4

MPRR is an important metric of combustion speed, and is associated with increased heat transfer to engine components. This must be kept to safe levels, and usually is part of a tradeoff between engine performance and durability. The 50-cycle average of MPRR produced by the tests as described in Fig. 4.1 is shown in Fig. 4.2. Here MPRR is plotted as a function of H2int. The four choices of SOI cluster into three distinct groups. The earliest (SOI=-2) and latest (SOI=-27) have a relatively low MPRR of < 1 bar/CAD until approximately 9 vol% intake H2. From there, late (SOI=-2) injection continues to have a low MPRR, while for the earliest injection (SOI=-27) the MPRR starts to increase with increasing intake hydrogen fraction. For a given H2int, SOI=-10 tends to have the largest MPRR of 4–7.5 bar/CAD compared to other SOI. MPRR increases with H2int. SOI=-20 has MPRR intermediate to the other points of 2–7.5 bar/CAD, again increasing with H2 addition.

When DOI is constrained, H2exh is greatly affected by H2int. At lower H2int, H2exh is also affected by SOI. Conversely MPRR is greatly affected by SOI, and also by H2int.

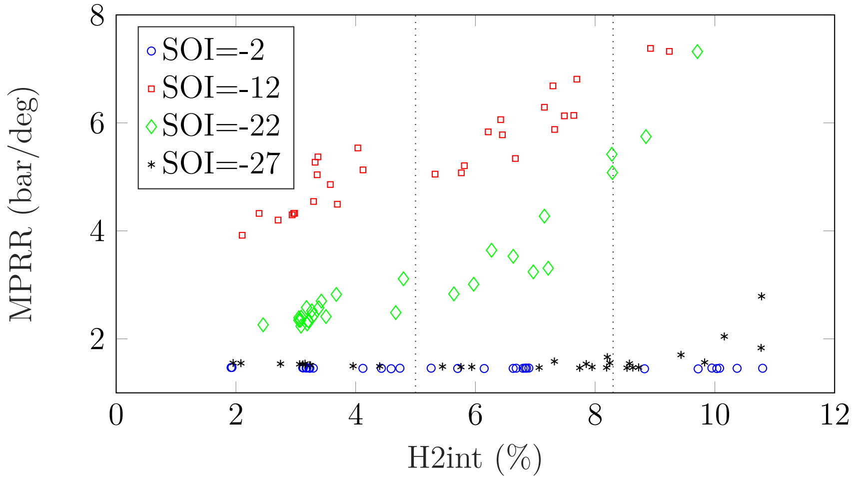

Figure 4.2: MPRR vs H2int with DOI=0.23ms and SOI={-2,-12,-22,-27}. Dotted lines indicate values of H2int used in Fig. 4.3 and Fig. 4.4

4.3 Timing Sweep

To investigate the effect of SOI to greater resolution, a sweep was performed with DOI=0.23ms and H2int= 5 or 8.3%. This corresponds to operation at IMEP≈2 or IMEP≈4 bar, although actual IMEP is allowed to vary.

Fig. 4.3 plots H2exh as a function of SOI. For H2int=8.3%, H2exh=0.35±0.04% and is insensitive to SOI. For H2int=5%, consistent with Fig. 4.1, H2exh shows a strong dependence on SOI. At the minimum near SOI=-22, H2exh=0.96% compared to H2exh=2.4% at SOI=2.

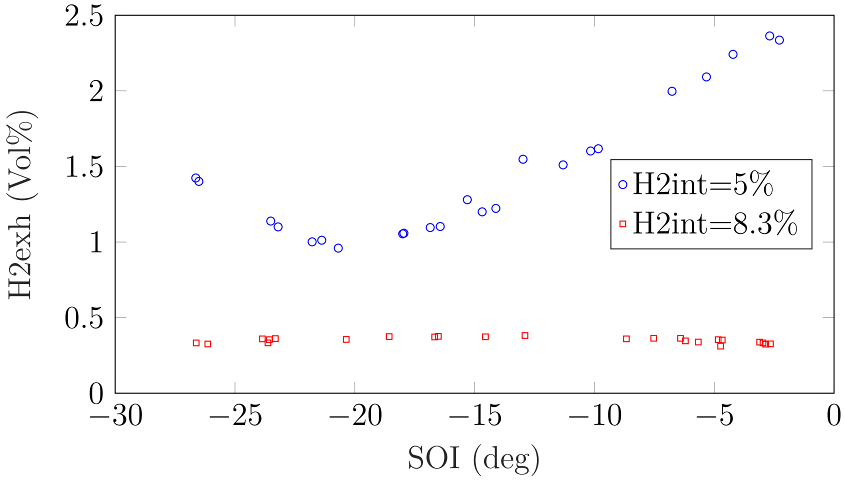

Figure 4.3: H2exh vs SOI, DOI=0.23ms, H2int=5% and 8.3%

MPRR is shown as a function of SOI in Fig. 4.4. Here both H2int=5% and H2int=8.3% show similar peaks in MPRR near to SOI=-10 and SOI=-13.

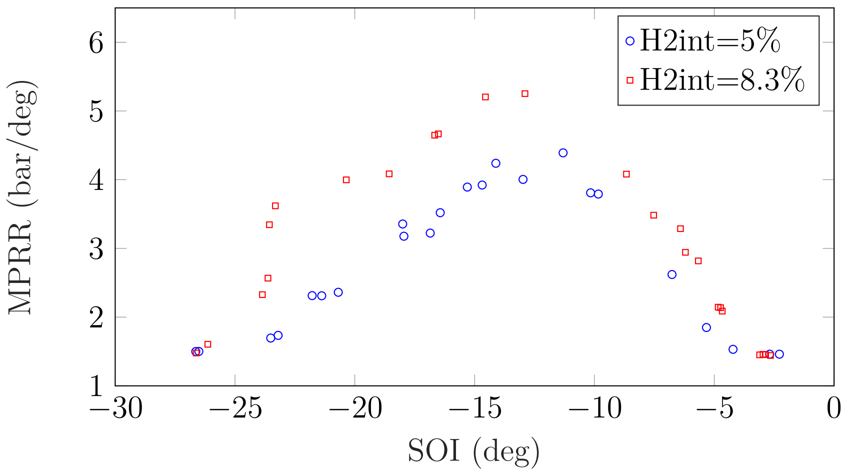

Figure 4.4: MPRR vs SOI, DOI=0.23ms, H2int=5% and 8.3%

To gain further insight into the relationship between H2exh and MPRR, H2exh is plotted vs MPRR in Fig. 4.5. For H2int=8.3% the slip is relatively constant, so varying SOI does not reduce slip, but can increase MPRR. For H2int=5%, there is a distinctive shape due the peak of H2exh (Fig 4.3) being shifted relative to the peak in MPRR (Fig. 4.5). Thus for a given MPRR, there is a value of SOI that results in this MPRR at high slip, and another SOI that results in low slip. This is largest at low MPRR, before the high-slip and low-slip points converge around MPRR=4.5 bar/deg. For H2int=5%, the low MPRR region occurs at early and late SOI, and the high MPRR region occurs near SOI=-18.

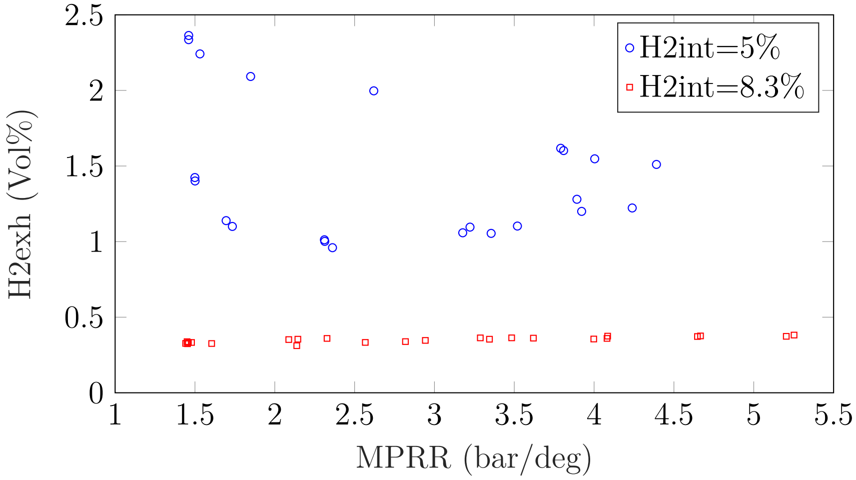

Figure 4.5: H2exh vs MPRR, DOI=0.23ms, H2int=5% and 8.3%

4.4 Constant Load of 4 and 6 bar IMEP

An engine often operates at a prescribed speed and torque. Here, the engine was mapped by prescribing a diesel injection (DOI) and varying the hydrogen injector duration (correlated to H2int) to meet a load target of either IMEP=4 bar or IMEP=6 bar. The fraction of fuel energy made up by hydrogen (HES) was therefore also varied for each constant-IMEP point. SOI was held constant to one of four values.

DOI was bounded by rough combustion (High MPRR) at larger DOI, and misfire at smaller DOI. For IMEP=4, the engine could operate with a ride range in SOI and so SOI=-34, SOI=-24, SOI=-14, and SOI=-4 were chosen. For the 6 bar points, early timing (SOI=-4) tended to lead to high MPRR> 15 bar/CAD at large diesel DOI, and late timing (SOI=+1) tended to result in misfire at low DOI. Therefore only SOI=-1 was chosen.

Each operating point was repeated three times per point, to estimate overall repeatability. The error bars in the following graphs show the median data point, surrounded by the minimum and maximum observed value. The experimental results are given in Tables B.5, B.6, B.7, B.8, and B.9 located in Appendix B.

4.4.1 CO_2 Equivalent Emissions

CO_2 equivalent emissions (CO2eq) are shown as a function of HES in Fig. 4.6. These equivalent emissions totals are calculated using Eqn 2.7. CO2eq for all values of SOI and both engine loads follow a similar trend, replacing hydrogen with diesel causes a monotonic decrease in CO2eq. This closely tracks the replacement value. At IMEP=4 bar, SOI=-30 and HES=51%, CO2eq = 380 g/kWh. At IMEP=4 bar, SOI=20 and HES=88%, CO2eq = 108 g/kWh. The IMEP=6 bar case closely follows the IMEP=4 bar cases.

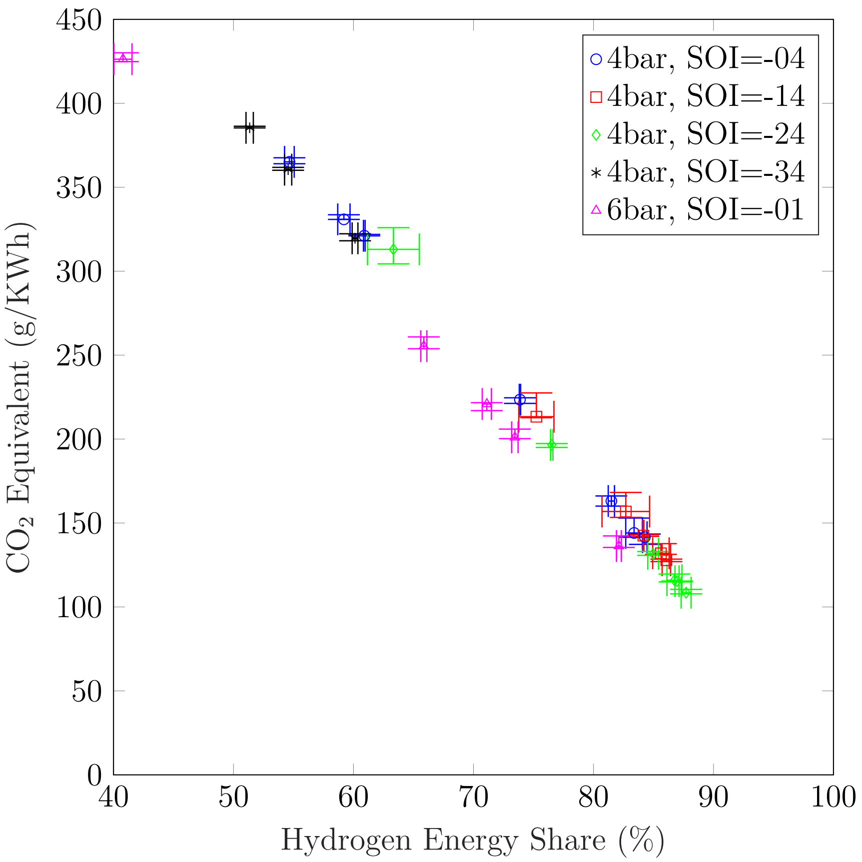

Figure 4.6: Overall CO_2 Equivalent vs HES, 4 and 6 bar IMEP

The CO2eq contribution, in g/kWh, of only the unburned hydrogen is shown in Fig. 4.7. As HES increases, H_2 slip decreases. Therefore, the decrease in total CO2eq is made up of both a reduction in diesel useage, and decrease in H2exh. Hydrogen slip can make up a sizeable fraction of total CO2eq emissions. At IMEP=4 bar, SOI=0 and HES=55%, H2 slip makes up 41 g/kWh of CO2eq out of 365 g/kWh total, or 11%. As HES increases, total CO2eq decreases faster than H_2 slip. At IMEP=4 bar, SOI=-10 and HES=86%, slip contributes 33 out of 132 g/kWh, or 25% of the total. The IMEP=6 bar points show less H_2 slip. At HES=41%, H_2 slip contributes 12 g/kWh equivalent (2.9% of total), and at HES=82% H_2 slip contributes 6.2 g/kWh (4.6% of total).

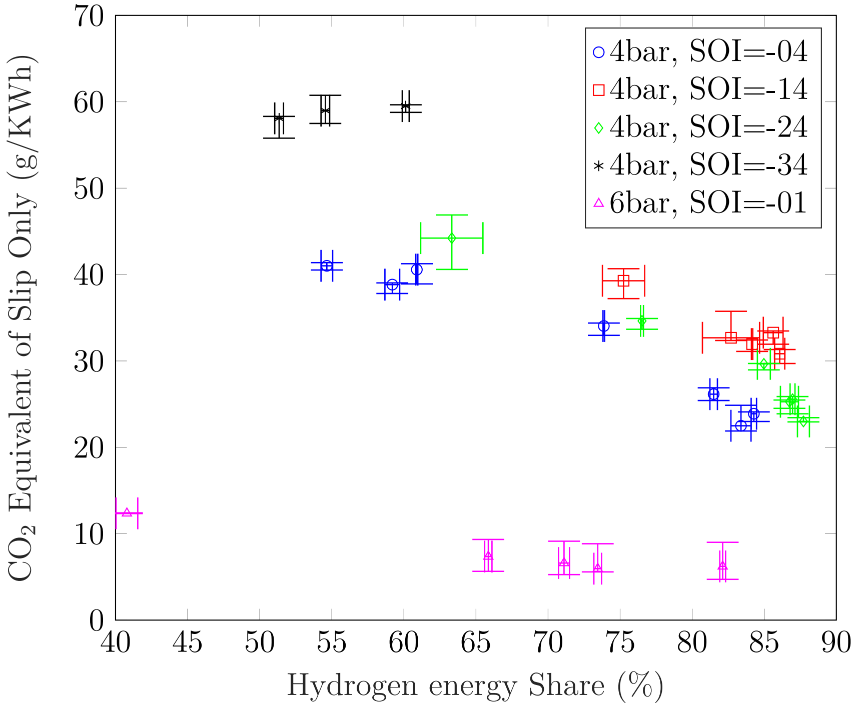

Figure 4.7: CO$_2$ Equivalent of H2exh only, 4 and 6 bar IMEP

Based on Section 4.2 Fig. 4.1, H2exh is greatly affected by H2int. Fig. 4.8 presents H2exh as a function of H2int for IMEP=4 and IMEP=6. Compared to Section 4.2, here DOI is not constant, and as H2int increases DOI decreases to keep IMEP constant. For both IMEP=4 bar and IMEP=6 bar, increasing H2int decreases H2exh. This is despite the fact that more hydrogen is associated with a smaller diesel injection, providing less ignition energy to the H2-air mixture.

In Fig. 4.8, IMEP=6 bar shows a similar decreasing trend in H2exh to IMEP=4 bar, but at lower values. For H2int=6%, the lower value of H2exh is attributed to greater DOI required to create 6 bar IMEP. For H2int>7%, the low H2exh is consistent with Fig. 4.1.

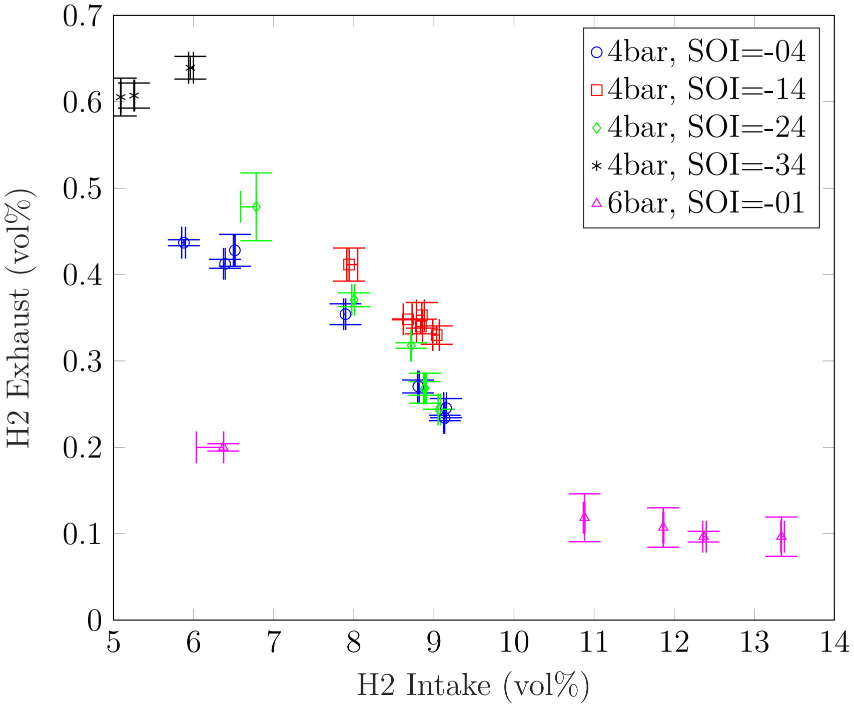

Figure 4.8: H2 Exhaust vs H2-Air Intake Mixture, 4 and 6 bar IMEP

Thermodynamic efficiency, η_{th}, is plotted in Fig. 4.9. For high HES, at IMEP=4 later SOI=-4 has lower efficiency compared to SOI=-14 and SOI=-24. This shows some benefit to earlier SOI at IMEP=4. Thermal efficiency is further discussed in Subsection 4.4.2 Fig. 4.12.

A tradeoff is seen in thermal efficiency vs slip reduction. In Fig. 4.1, DOI is kept constant and for a given H2int in the range 6–9%, late timing (SOI=-2) results in the highest H2exh. However, when IMEP is kept constant in Fig. 4.8, late timing (SOI=-4) results in the lowest H2exh. This correlates to Fig. 4.9, where late timing is associated with lower η_{th}. For a given H2int, more diesel is added to keep the IMEP constant and thus there is greater ignition energy. For given DOI, more hydrogen is added which burns more completely.

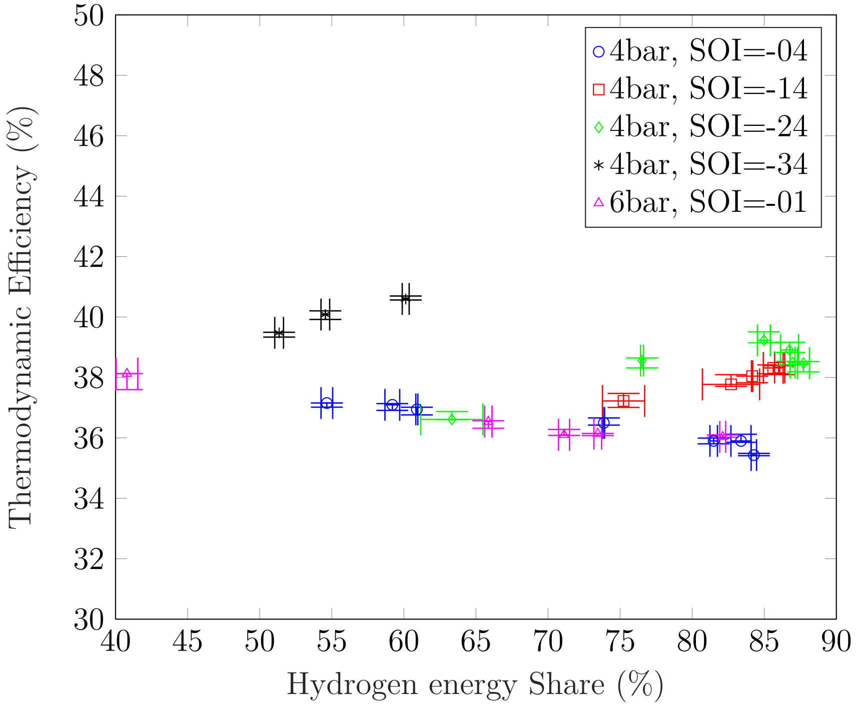

Figure 4.9: Overall Thermodynamic Efficiency vs HES, 4 and 6 bar IMEP

4.4.2 Combustion Metrics

Combustion metrics are presented relative to HES. The shape of dual-fuel heat release curves for this engine, including a pattern commonly encountered consisting of two separate peaks, is explored further in Chapter 5. However the purpose of this subsection is to summarize the results as they pertains to 4 and 6 bar IMEP at varying HES. The combustion metrics are tabulated in Tables A.5, A.6, A.7, A.8 and A.9. Representative, normalized cumulative heat release curves and thresholds used to calculate beginning and end of combustion are shown in Fig. 2.14 in Section 2.9. End of combustion is defined as CA90, and thus burn duration is defined as CA90-CA10.

Fig. 4.10 presents ignition delay (based on CA10) as a function of HES for the one, IMEP=6 bar and four, IMEP=4 bar cases. For the IMEP=6 bar case (at SOI=-1), CA10 is relatively unaffected by HES. Likewise at IMEP=4 bar (SOI=-4, -14), there is small effect of HES. At IMEP=4 bar and SOI=-24, ignition delay is strongly affected by HES, changing from 15 to 25 CAD. Ignition delay of the SOI=-34 case is the longest of the IMEP=4 bar cases, and increases with HES from 28 to 31 CAD. For these tests at constant IMEP, as HES is increased the delay period is affected by both greater H2int and smaller DOI.

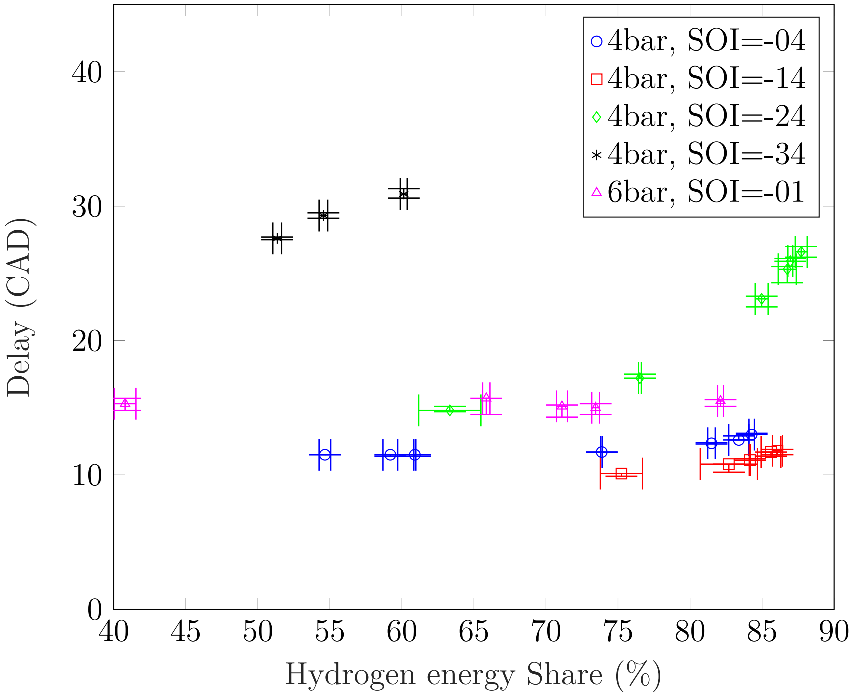

Figure 4.10: Ignition Delay (SOI–CA10) vs HES, 4 and 6 bar IMEP

Fig. 4.11 shows burn duration as a function of HES. For the IMEP=4 bar and SOI=-4 case, there is a significant increase in burn duration when substituting hydrogen for diesel, from 13 to 21 CAD. Full heat release curves explaining this phenomenon are presented in Chapter 5. This increase in burn duration is consistent with the reduced maximum pressure rise rate (Fig. 4.13) observed at greater HES. This upward trend is present for all IMEP=4 bar cases, and is particularly prominent for the SOI=-24 case, where burn duration increases fourfold from 5 to 21 CAD. This slower combustion is also consistent with Fig. 4.13 where MPRR steeply decreases with HES. SOI=-24 shows a similar pattern across its more limited operating range. The earliest timing, SOI=-34, shows among the shortest burn durations, increasing with hydrogen addition. For the IMEP=6 bar case, burn duration is less affected by

HES than at lower load.

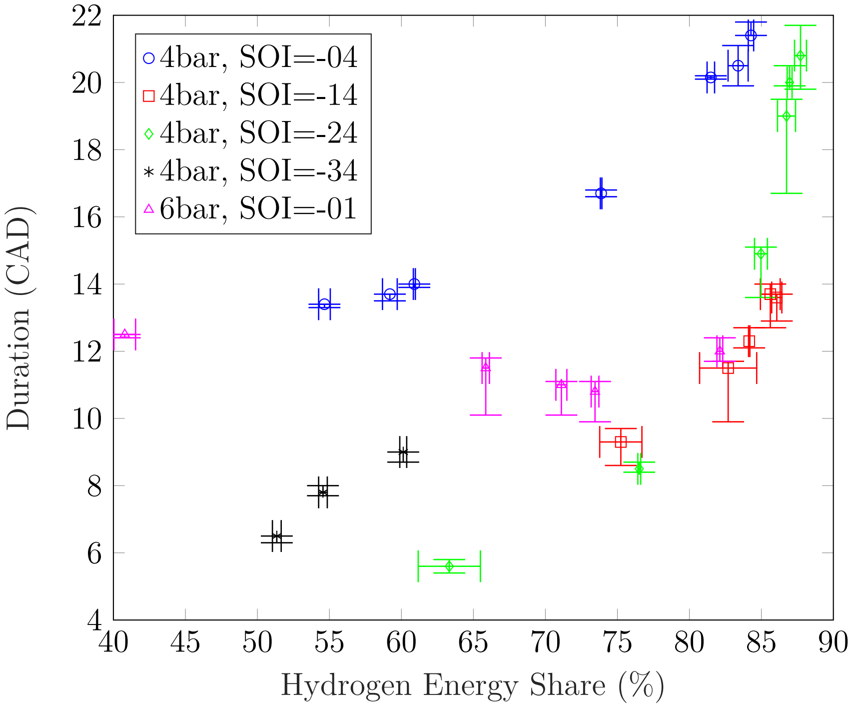

Figure 4.11: Burn Duration vs HES, 4 and 6 bar IMEP

The crank angle where 50% of fuel fraction has burned, CA50, is an important metric and often associated with efficiency. Fig. 4.12 presents the thermal efficiency as a function of CA50. For IMEP=6 bar, patterns are less apparent, with CA50 always in the small range of 16–20 aTDC. However, for IMEP=4 bar, a clear pattern emerges for IMEP=4 bar where thermal efficiency is maximized at CA50≈5 CAD.

Combustion metrics for these IMEP=4 and 6 bar tests are tabulated in Tables A.5, A.6, A.7, A.8, and A.9 located in Appendix A.

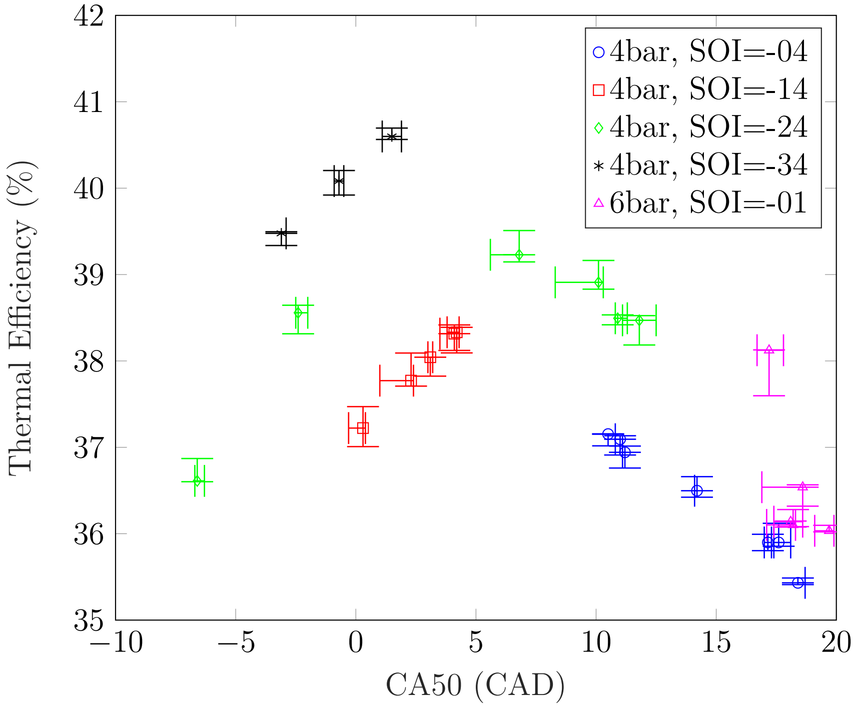

Figure 4.12: Thermal Efficiency vs CA50, 4 and 6 bar IMEP

4.4.3 Maximum Pressure Rise Rate

Maximum Pressure Rise Rate (MPRR) is a metric of combustion speed, which is important for engine durability. High pressure rise rates will increase fluid shear and reduce the boundary layer, increasing heat transfer to the engine components. This increased heat transfer can also reduce engine efficiency and lead to local hot spots promoting preignition [9],[44].

Results at IMEP=4 and IMEP=6 bar are presented in Fig.4.13. At each choice of SOI, the MPRR decreases monotonically with increasing HES. Notably, the SOI=-34 results are the lowest MPRR at a given HES fraction, despite the longer ignition delay and ignition well before TDC (Fig. 4.10) and short burn duration (Fig. 4.11). The SOI=-1 (IMEP=6) and SOI=-4 (IMEP=4) cases also tend to have lower MPRR for given HES. SOI=-14 has a high MPRR, increasing rapidly with larger DOI (lower HES) and demonstrating the reason behind the limited range of HES for this SOI.

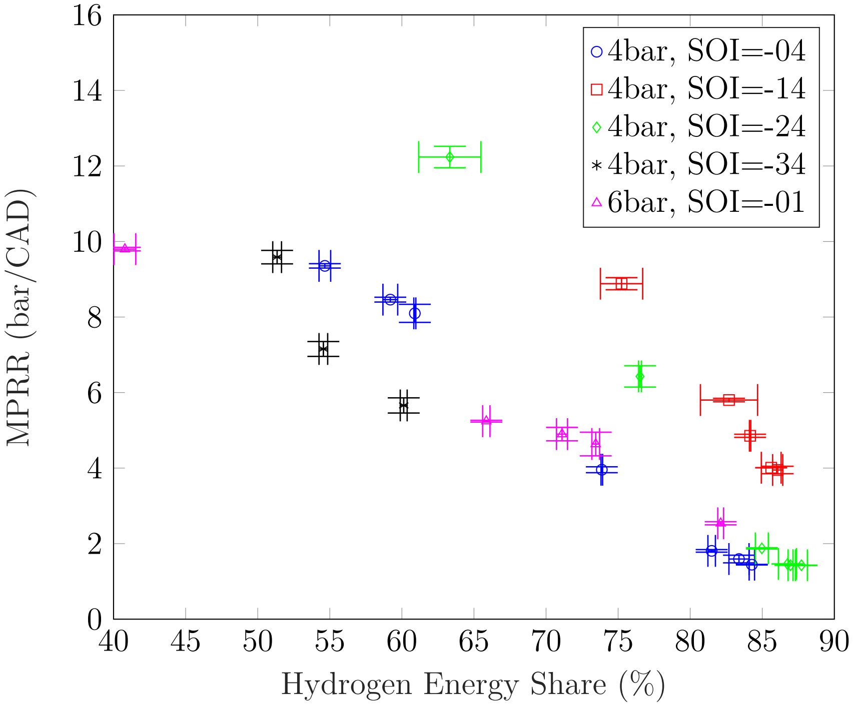

Figure 4.13: MPRR vs HES, 4 and 6 bar IMEP

While it is certainly expected that MPRR and peak heat release will be linked, there are still factors that affect the relationship between MPRR and peak heat release. Pressure and volume at the time of highest heat release will affect the relationship. Different pressure trace filtering is used for each calculation - a lower cutoff is used for heat release to suppress ringing, but as MPRR does not depend on duration of ringing (only the peak of the derivative) a higher cutoff frequency is used. The effect of averaging multiple cycles may also be significant - the pressure trace is averaged before calculating heat release, whereas the MPRR is calculated per-cycle and then averaged. Fig. 4.14 shows a clear correlation between the two values, dependent on SOI. For SOI=-1, the slope of MPRR vs peak heat release is lower. For SOI=-14, the slope is higher, showing a reduced tolerance for high peak heat release at this SOI, and helping explain the high MPRR encountered at this SOI.

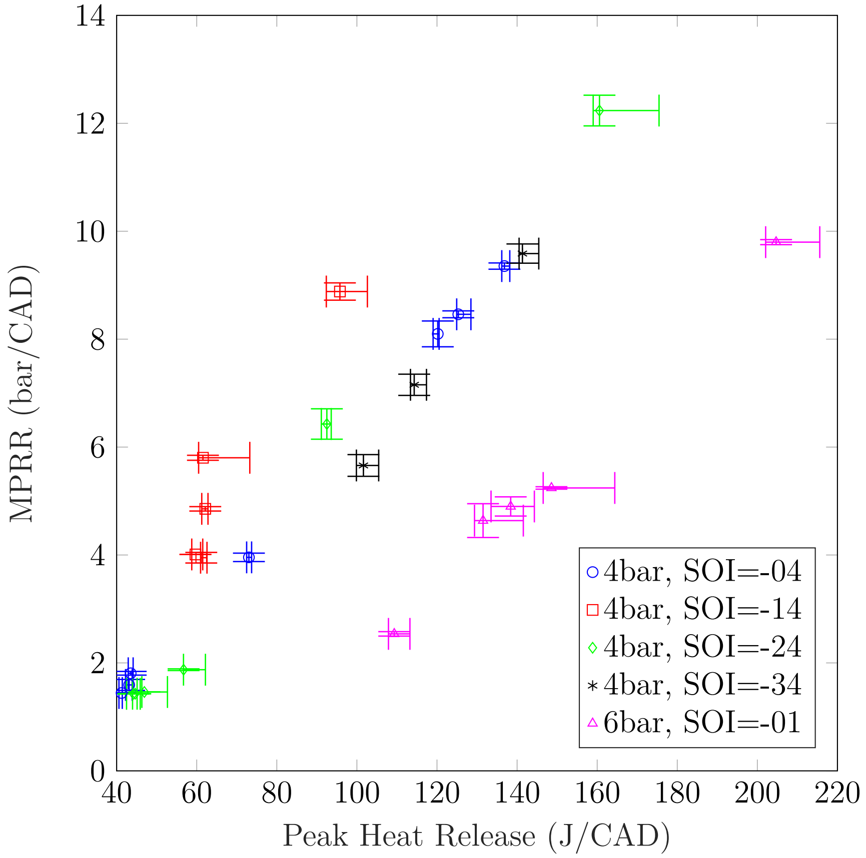

Figure 4.14: MPRR vs Peak Heat Release, 4 and 6 bar IMEP

4.4.4 Summary of Testing at Constant Load of 4 and 6 bar IMEP

The results from this section are summarized below:

At 4 and 6 bar IMEP, CO_2 equivalent emissions closely follow diesel replacement. Unburned hydrogen emissions also decrease with increasing HES. A tradeoff is observed at IMEP=4 bar where later SOI reduces the thermal efficiency, forcing an increase in total fuel that causes the hydrogen to burn more completely reducing hydrogen emissions.

Increasing HES tends to increase the ignition delay at some points, however ignition delay is most affected by SOI. Burn duration increases with HES at all 4 bar points, but not at 6 bar. As CA50 moves toward 5 CAD, from either direction, thermal efficiency is increased.

MPRR is decreased by increasing HES at all 4 and 6 bar points.

4.5 Constant Load of 3 bar IMEP

The same methodology as Section 4.4 was extended to 3 bar IMEP. Similar constraints were observed in operation, where DOI was bounded by misfire at low DOI and fast combustion at high DOI. Both H2int and DOI are more constrained by the requirement to not exceed a lower IMEP.

Like Section 4.4, each operating point was repeated three times and error bars show the minimum and maximum run. Often results were less consistent at this lower load, resulting in greater errorbars in the following figures.

Experimental results are reproduced in Tables B.1, B.2, B.3, and B.4 located in Appendix B.

4.5.1 CO_2 Equivalent Emissions

Fig. 4.15 shows the calculated total CO_2 equivalent emissions (CO2eq), calculated using Eqn 2.7, of the IMEP=3 bar points with IMEP=6 bar points added for comparison. Both carbon dioxide and the effect of unburned exhaust hydrogen are included in this total.

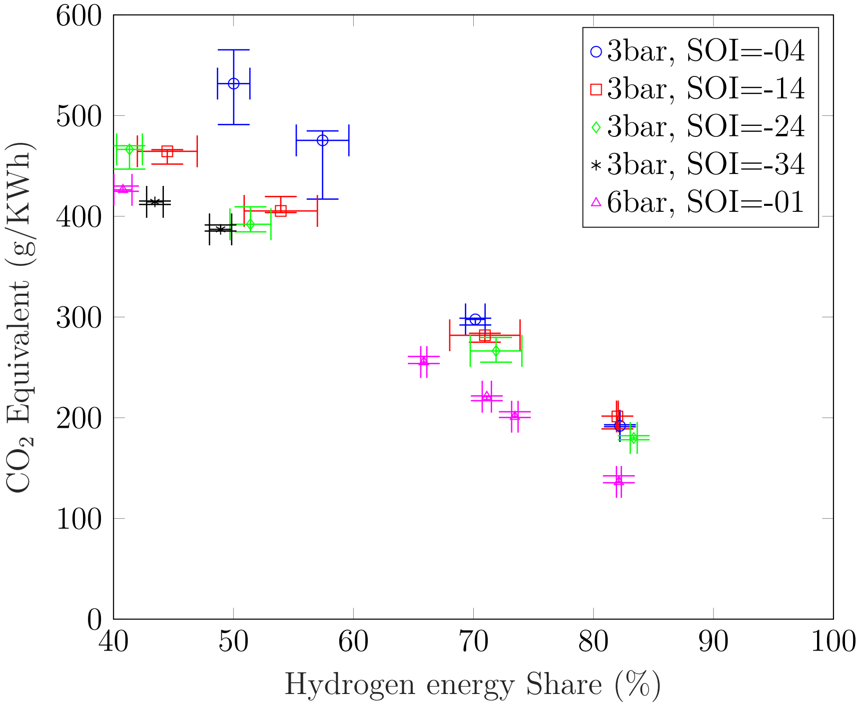

Figure 4.15: Overall CO_2 Equivalent vs HES, 3 and 6 bar IMEP

Unlike the 4 and 6 bar operating points in Fig. 4.6, diesel injection timing makes a significant difference to total CO_2 emissions for the lower 3 bar cases shown in Fig. 4.15. For constant injection timing, there is again a monotonic decrease with increasing HES. All 3 bar points result in greater CO_2 equivalent emissions, relative to HES, than the 6 bar case. SOI=-4 tends to have larger total CO_2 equivalent emissions at a given SOI, while SOI=-24 tends to have less than SOI=-4 and SOI=-14. SOI=-34 resulted in the lowest total CO2eq, but had limited operating range.

The unburned hydrogen emissions, expressed as g/kWh of CO2eq, are plotted in Fig. 4.16. At IMEP=3, the effect of unburned hydrogen is much larger than at IMEP=6, peaking at 150 g/kWh CO2eq. This also makes up a greater proportion of the total. At SOI=20 and HES=85%, slip contributes 76 of a total of 201 g/kWh, or 38% of the total CO2eq. Additionally, at IMEP=4 (Fig. 4.7) slip decreased monotonically with higher HES while here at IMEP=3, in Fig. 4.16, only SOI=-4 is monotonic over a large range. This is attributed to these IMEP=3 points operating at lower

H2int compared to IMEP=4.

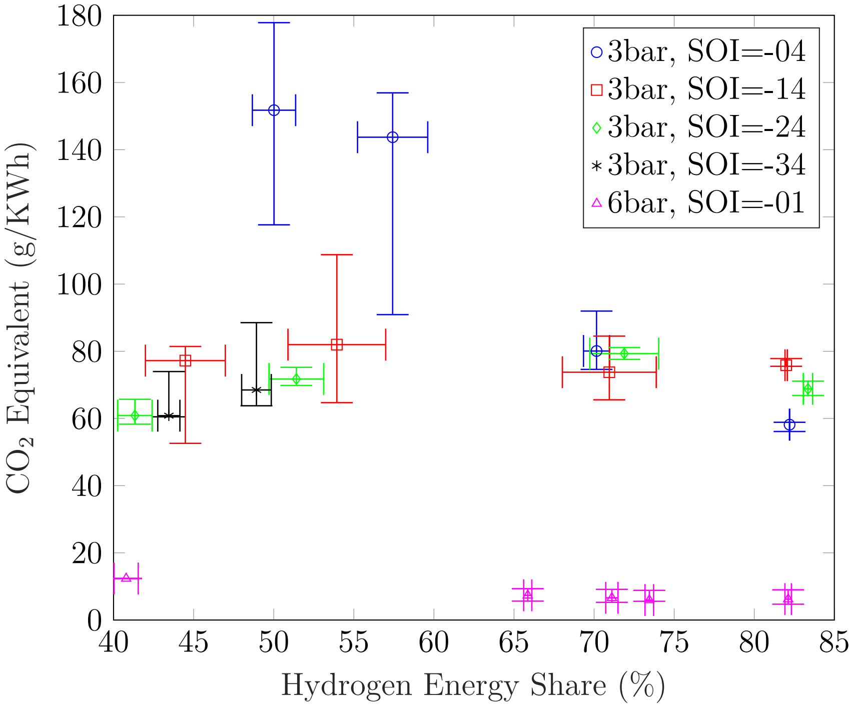

Figure 4.16: CO$_2$ Equivalent of H2exh only, 3 and 6 bar IMEP

Fig. 4.17 shows the dependence of H2exh on H2int at different SOI. Comparing to IMEP=4 case in Fig. 4.8, where increasing H2int monotonically decreased H2exh, at IMEP=3 H2exh is not monotonic. The IMEP=3 case, like the IMEP=4 case, is consistent with Fig. 4.1, but for the 3 bar case H2int is lower and so 3 bar operation includes some regions of Fig. 4.1 where increasing H2int increases H2exh. Unlike at 4 bar, at 3 bar SOI=-4 shows the greatest slip compared to other SOI.

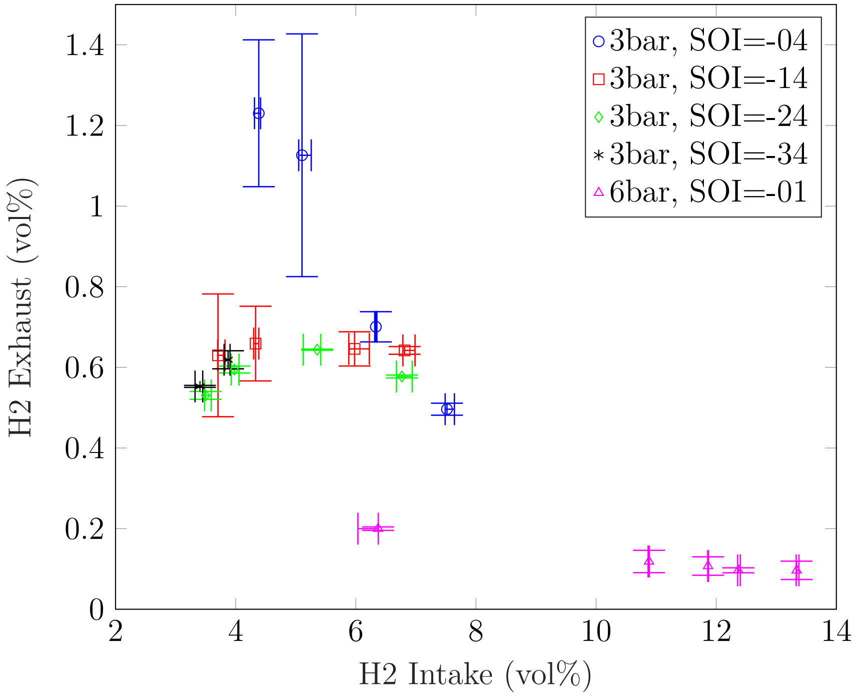

Figure 4.17: H2exh vs H2int, 3 and 6 bar IMEP

Fig. 4.18 plots thermal efficiency (η_{th}) as a function of HES. Comparing to the IMEP=4 bar cases in Fig. 4.9, there is a greater range in η_{th} for IMEP=3. Again the later timing (SOI=-4) trends lower than others, with the SOI=-14 and SI=-24 cases trending higher.

At IMEP=3, a tradeoff between η_{th} and slip is not readily apparent. Instead, SOI=4 results in both high slip and low η_{th}, with low η_{th} possibly driven by the high slip. Shifting SOI earlier at this load burns the hydrogen more completely and also increases thermal efficiency. For a given SOI, total CO2eq is again monotonically reduced by increasing HES.

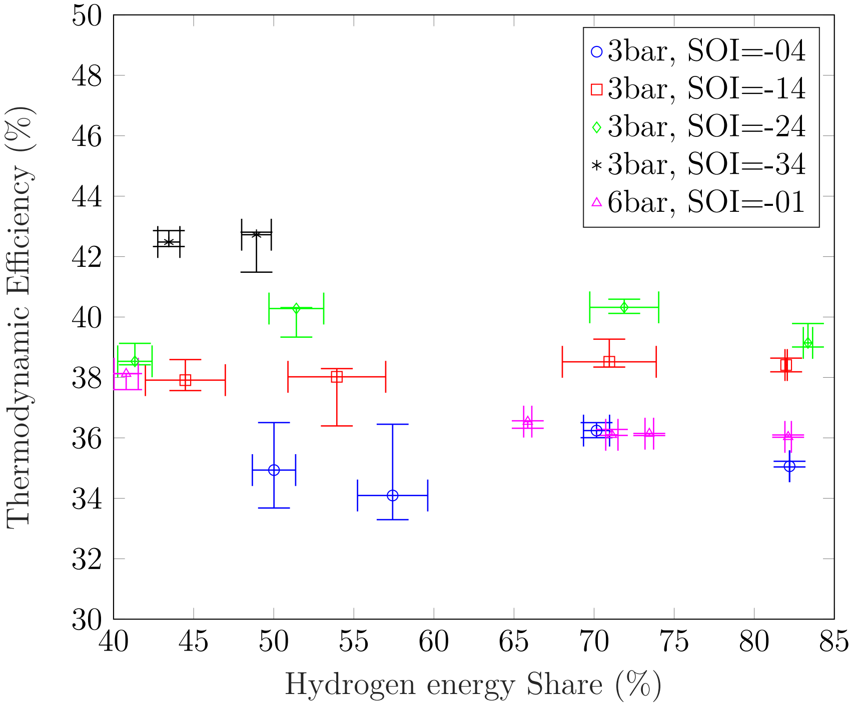

Figure 4.18: Thermodynamic Efficiency vs HES, 3 and 6 bar IMEP

4.5.2 Combustion Metrics

Fig. 4.19 shows the effect of varying HES on ignition delay. Similar to 4 bar operation, SOI=-14 results in the shortest delay, which is relatively constant near 10 CAD. SOI=-4 shows a slightly longer delay at near 12 CAD, relatively unaffected by HES. Operation at SOI=-24 is affected by HES, with larger diesel injections and less hydrogen (low HES) resulting in 15 CAD while higher HES lengthens this delay to 22 CAD. The earliest injection, at SOI=-34, has significantly increased ignition delay as expected by the lower in-cylinder pressure and temperature at injection.

Burn duration is shown in (Fig. 4.20). For SOI=-4, this increases with higher HES. A similar trend is observed at SOI=-24. For SOI=-14, varying HES does not significantly affect the burn duration until the highest HES value, which is asscociated with the smallest diesel injection. Burn duration for the two viable SOI=-34 points are similar to other SOI within the restricted range of HES available at that SOI.

Combustion metrics for these IMEP=3 bar tests are tabulated in Tables A.1, A.2, A.3, and A.4 located in Appendix A.

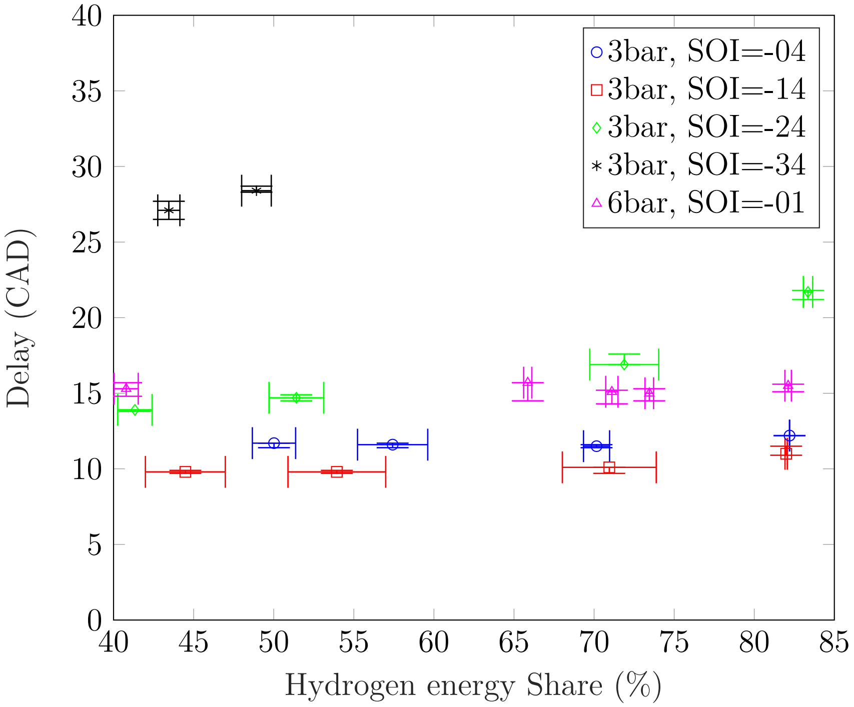

Figure 4.19: Ignition Delay vs HES, 3 and 6 bar IMEP

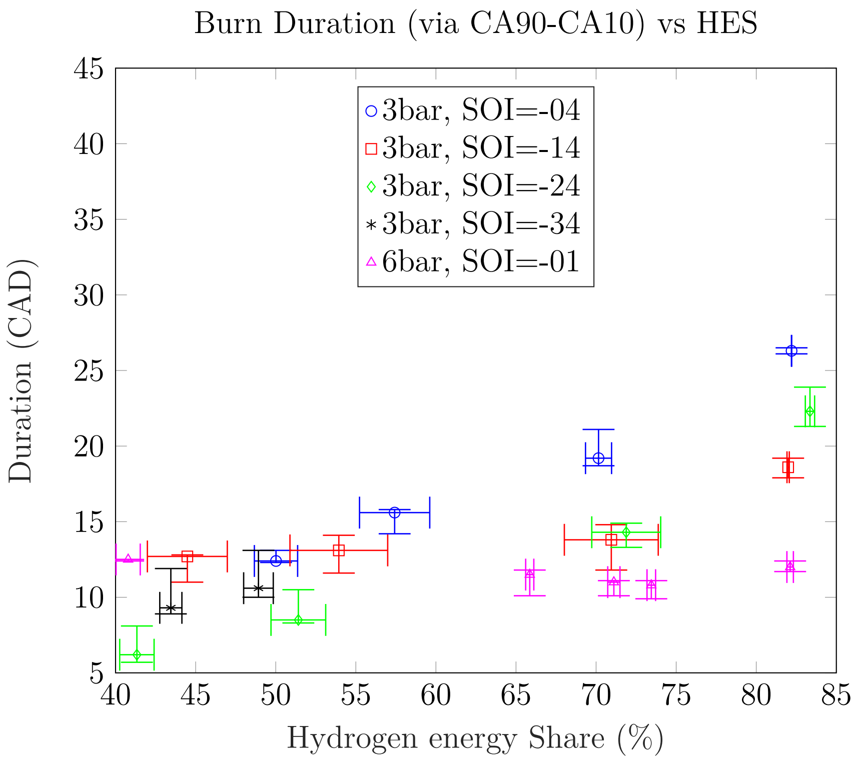

Figure 4.20: Burn Duration vs HES, 3 and 6 bar IMEP

4.5.3 Maximum Pressure Rise Rate

Fig. 4.21 shows Maximum Pressure Rise Rate (MPRR) as a function of HES. Similarly to 4 bar operation (Fig. 4.13), SOI=-14 results in the severest pressure rise rate and the greatest reduction in MPRR as HES in increased. SOI=-4 shows a low MPRR, and results from 3 bar SOI=-4 are very similar to 6 bar SOI=-1. SOI=-34 results in a low MPRR for a given HES, however the range in HES is limited.

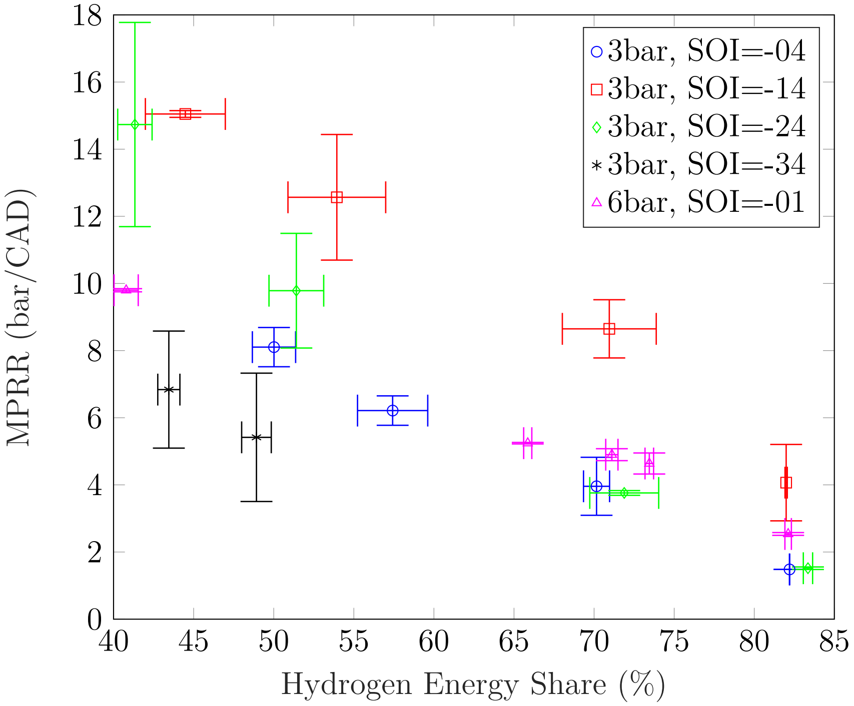

Figure 4.21: MPRR vs HES, 3 and 6 bar IMEP

4.5.4 Summary of Testing at Constant Load of 3 bar IMEP

The results from this section are summarized below:

At 3 bar load, CO_2 equivalent emissions at a given SOI are monotonically decreased by maximizing HES. Compared to 4 bar operation, SOI has a large impact on CO_2 equivalent emissions. The effect of unburned hydrogen on the total is higher, reaching 38% of the total.

Compared to 4 bar, the range in thermal efficiencies is higher, and unlike 4 bar operation low efficiency is associated with high slip. At the lower H2int encountered in 3 bar operation, increasing H2int does not always decrease H2exh.

Ignition delay is affected by HES at some points, but is mostly dominated by SOI. Burn duration is affected by both SOI and HES.

MPRR is in the same range for 3 bar as for 4 bar. The trends are similar with SOI=-14 resulting in high MPRR for a given HES compared to SOI=-4. Increasing HES decreases MPRR for a given SOI.

4.6 Maximum Hydrogen Share at 2,3,4,6 bar IMEP

4.6.1 Overview of Maximum Hydrogen Share Tests

Several advantages of lowering diesel and increasing hydrogen energy share were found in prior Sections 4.4 and 4.5. Not only did carbon dioxide emissions reduce, for many operating conditions unburned hydrogen emissions also reduced. MPRR was lowered for all cases. In this section, the dual-fuel engine is operated with the observed minimum reliable pulse width (DOI=0.17ms), several injection timings of SOI=-4 to -29 dependent on operating point, and hydrogen is added to meet a setpoint of IMEP=2,3,4 and 6 bar. Similar to Sections 4.4 and 4.5, each point was replicated three times to quantify repeatability of the overall setup. Error bars in the following plots show the median data point surrounded by minimum and maximum.

As before, the allowable operating range was bounded. With the small DOI, early SOI resulted in misfire and so the earliest injection here is at SOI=-29. At early SOI adding hydrogen to increase IMEP resulted in misfire, so IMEP=3 and 4 bar points are constrained to later injection. Late injection, past SOI=-4, also resulted in misfire. For IMEP=6 bar only one SOI, at SOI=-4, was tested. Earlier (SOI=-9) resulted in intermittent cycles with unacceptable pressure rise rate. Later SOI resulted in misfire. At SOI=-4, high pressure rise rate limited hydrogen addition and so load was bounded to 6 bar IMEP regardless of SOI.

Diesel DOI is held constant for all tests, however measured injected fuel mass varies with SOI. The dependence of injected fuel mass on SOI is likely due to pressure pulsations inside the fuel rail [41]. Due to the dominating effect of diesel mass on total CO_2 equivalent emissions (Sections 4.4 and 4.5) and to fairly compare operating points, only the CO_2 equivalent contribution of hydrogen slip is considered. Further, with a constant DOI, HES is not a good metric to compare points so these results are presented in terms of SOI. For all tests, HES is in the range of 78–89%. Operating points are summarized in Table B.10 located in Appendix B.

4.6.2 CO_2 Equivalent Emissions

Unburned hydrogen emissions, at each power level as a function of SOI, are shown in Fig. 4.22. Hydrogen emissions are in units of CO_2 equivalent per kWh. At IMEP=2 bar, both due to high unburned hydrogen and low power, specific emissions are high ranging from 150–300 g/kWh equivalent. Minimum emissions are near SOI=-24, however there is a large scatter in the dataset indicating high variation in combustion at all IMEP=2 bar points. While at this load the average power was also difficult to keep consistent, however Table B.10 shows that the unburned hydrogen varied more than the IMEP. At higher power, IMEP=3 bar, unburned hydrogen emissions are less variable and show a peak near SOI=-14. At IMEP=3 bar, SOI=-4 has the lowest specific emissions. Emissions are still substantial, around 75 g/kWh equivalent. At IMEP=4 bar, the trend is similar but emissions are lower. The single point at IMEP=6 bar had much lower emissions indicating more complete combustion of the hydrogen fuel.

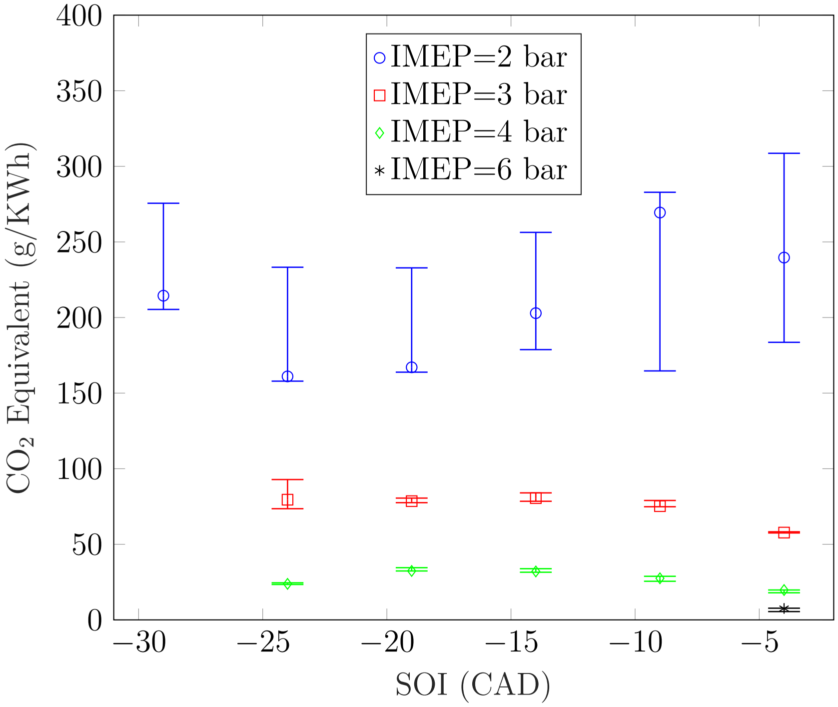

Figure 4.22: CO_2 Equivalent of H2exh vs SOI at Different IMEP, Max HES run

In prior testing shown in Fig 4.1, Fig. 4.3, and Fig. 4.16, late SOI is associated with high unburned hydrogen. But here, at IMEP=3 bar and IMEP=4 bar, late SOI is associated with lower unburned emissions. This is attributed to the lower thermal efficiency (Table B.10) forcing more hydrogen fuel into the cylinder, which burns more completely.

In prior Section 4.2, H2exh was heavily dependent on H2int. For the minimum-DOI case, H2exh is plotted in Fig. 4.23 relative to H2int. SOI, as well as slight variation in diesel injected mass and variation in IMEP are not plotted and thus their effect will add to the scatter in Fig. 4.23. This allows an estimation of the effects of these variables. For IMEP=3 bar and IMEP=4 bar, both within and between the groups, there is a clear trend of decreasing hydrogen emissions with increasing H2int. For IMEP=6 bar, the hydrogen emissions are low. For IMEP=2 bar, the scatter is sufficiently large that conclusions are difficult within the group. However, for IMEP=3 and 4 bar, low H2int is associated with high H2exh within that IMEP group. Further, comparing between groups, higher H2int is associated with lower H2exh.

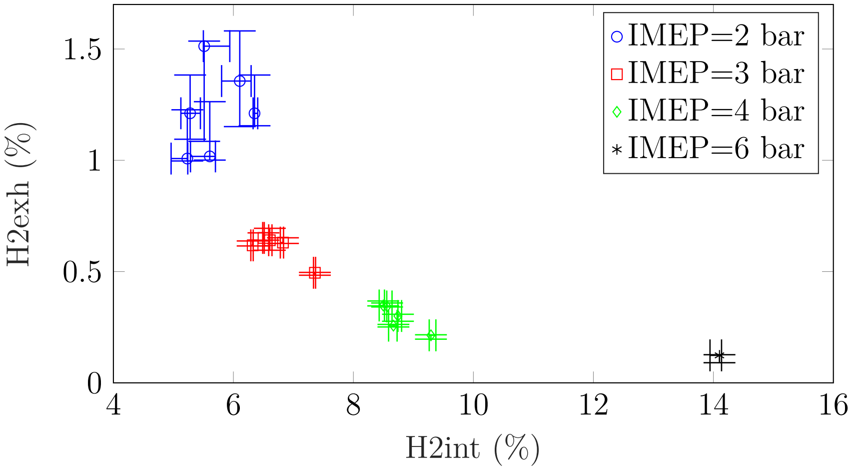

Figure 4.23: H2exh vs H2int at Different IMEP, Max HES run

4.6.3 Combustion Metrics

In this section, diesel DOI is held constant in contrast to Sections 4.4 and 4.5. This minimizes the effect of varying diesel injection and therefore the main factors are load (highly correlated to H2int as seen in Fig. 4.23) and SOI.

The ignition delay, based on CA10, is shown in Fig. 4.24. The reaction to varying IMEP (and therefore H2int) can be seen as a vertical displacement between points corresponding to different loads. For IMEP=2, 3, and 4 bar, and SOI=-19, -14, and -24, the lowest load (lowest H2int) points have the shortest delay. Therefore, H2int appears to retard ignition. For later SOI, this appears to be also the case, however, overlapping error bars make conclusions difficult. The single high-hydrogen, IMEP=6 point has slightly shorter delay than all other points at that SOI. Fig. 5.6 presents heat release rate for this point compared to other SOI=-4 points, showing that this IMEP=6 point has different characteristics than the other points and this shorter ignition delay is not just an artifact of faster combustion reaching the CA10 threshold faster. One possibility is that the more vigorous combustion increases cylinder wall temperature thus speeding up autoignition of the diesel plume. Chapter 5 contains a more detailed discussion of heat release in HDDF combustion.

SOI has a larger effect on ignition delay than load or H2int. As SOI is advanced from -4 to -9, the delay shortens and reaches a minimum. Further advancing SOI lengthens the delay.

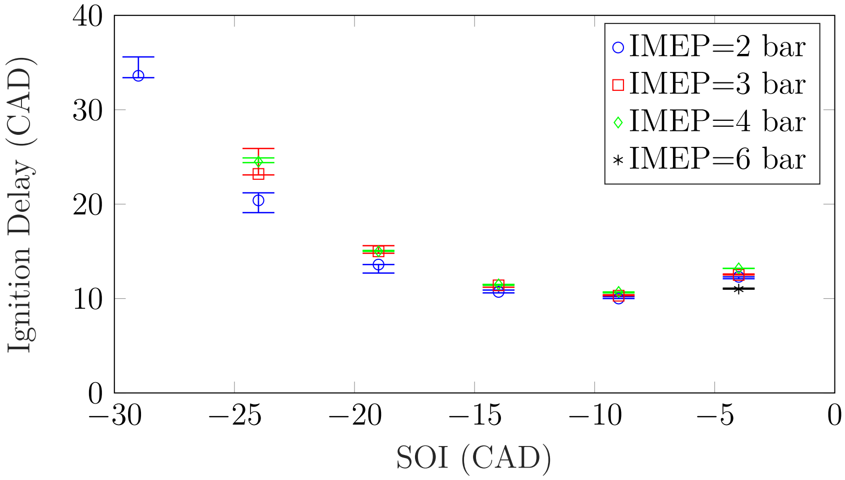

Figure 4.24: Ignition Delay vs SOI at Different Engine Loads, Max HES run

Thermal efficiency is presented as a function of CA50 in Fig. 4.25. Despite injection as early as SOI=-29, all values of CA50 are after TDC. The general trend is that as the position of CA50 increases to be further after TDC, the efficiency drops. The lowest-load point, IMEP=2, has the lowest efficiency, attributed to large amounts of fuel remaining unburned. IMEP=3, 4, and 6 have higher efficiencies, comparable to prior Sections 4.4 and 4.5.

Combustion metrics for the present, minimum diesel DOI and maximum HES tests are summarized in Table A.10 located in Appendix A.

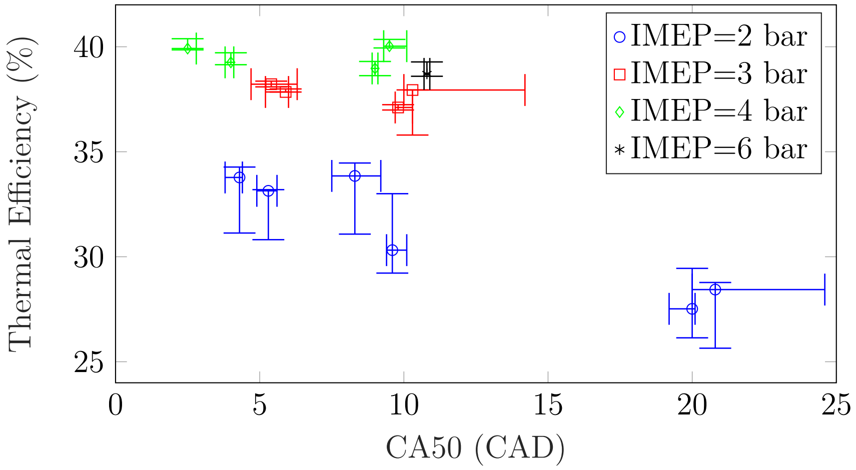

Figure 4.25: Thermal Efficiency vs CA50 at Different Engine Loads, Max HES run

4.6.4 Maximum Pressure Rise Rate

MPRR, as a function of SOI, is shown in Fig. 4.26. At a constant load, as SOI is varied, H2int changes only slightly (see Fig. 4.23). DOI is kept constant. Variation in MPRR across a constant load is mainly due to SOI, and vertical variation between constant SOI points in Fig. 4.26 is due to H2int.

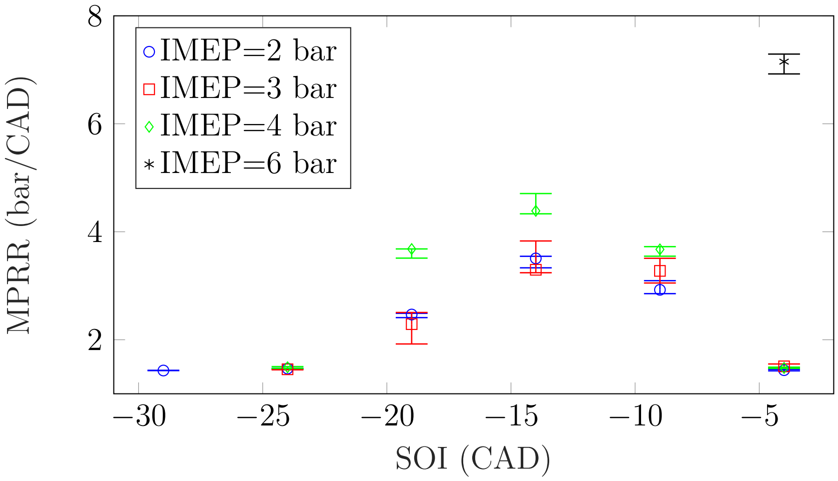

Figure 4.26: MPRR vs SOI at Different engine loads, Max HES run

MPRR of these tests are comparable to the highest-HES and lowest-MPRR points in Sections 4.4 and 4.5. For IMEP=2, 3, and 4, at the two extremes of SOI (SOI=-24 and SOI=-4), MPRR is at a minimum near MPRR≈1.5bar/CAD. For all IMEP in this range, SOI=-14 results in the largest MPRR. At a given SOI, the highest IMEP (therefore highest H2int) results in the highest MPRR. For lower IMEP, error bars overlap. The highest load point, IMEP=6, is again an outlier with high MPRR.

Similarly to Section 4.3, MPRR is most affected by SOI, with the peak occurring near SOI=-14.

4.6.5 Summary of Maximum Hydrogen Share testing

With diesel DOI set to a consistent minimum, operation could be extended down to IMEP=2 bar. At this power level, high emissions of unburned hydrogen were found.

Increasing power was achieved by increasing H2int, which has a strong correlation with decreasing H2exh.

For IMEP=2, 3, and 4 bar, MPRR is affected by both H2int and SOI. For all H2int in that range SOI=-14 results in the largest MPRR. The single IMEP=6 bar point, tested at SOI=-4, had higher MPRR however less than some tests where more diesel was used.

Ignition delay is affected by both the presence of hydrogen and SOI, however the main effect is by SOI. Near SOI=-9 ignition delay is minimized. Again IMEP=6 is an outlier, with low ignition delay. CA50 for all points is after TDC, with a scattered trend of thermal efficiency decreasing the farther that CA50 is from TDC.

4.7 Chapter Summary

In Section 4.2, with constant DOI unburned hydrogen emissions are strongly dependent on H2int. A peak in H2exh is observed when H2int is between 3-5 Vol%, with the location and magnitude of the peak dependent on diesel injection timing. Injection at SOI=-4 results in the largest unburned emissions. Earlier diesel injection timing, at SOI=-14 and SOI=-24, lower H2exh and shift the location of the peak to lower H2int. Advancing SOI further, reverses this trend. For these tests where IMEP is uncontrolled, MPRR was strongly dependent on SOI, and also increases with increasing HES.

In Section 4.3, SOI was varied with constant DOI and H2int. For H2int=5%, H2exh shows a minimum at SOI=-22, while for H2int=8.3% H2xh is insensitive to SOI. For both intake fractions, MPRR shows a maximum near SOI=-13.

In Sections 4.4 and 4.5, operation at constant IMEP=3,4 and 6 bar shows a trend that increasing HES decreases both CO_2 emissions and unburned hydrogen emissions. However as CO_2 is reduced, the lessening hydrogen emissions take on a larger percentage of the total GWP, reaching 22% of total in 4 bar operation and 38% for 3 bar operation. At low load, aftertreatment may be beneficial in decreasing total GWP of H2DF engines. At IMEP=4, total CO2eq is insensitive to SOI. However at IMEP=3, particularly for lower HES, the effect of SOI on total CO_2 equivalent increases. H2Exh appears to be primarily driven by low hydrogen fuel ratios, while MPRR apears to be driven mainly by large DOI and by SOI. Burn duration increases with increasing HES. At all tested loads, larger HES was asscociated with lower unburned hydrogen emissions, lower total GWP and lessened MPRR.

In Section 4.6, HES was maximized through minimizing DOI and operation was extended down to IMEP=2 bar. At IMEP=2, high specific emissions of unburned hydrogen were found. Combustion was also inconsistent at this low power level. At IMEP of 3 and 4 bar, specific unburned hydrogen emissions were lower at later SOI. This reveals a tradeoff where lower thermal efficiency resulted in more fuel, which burned more completely. H2exh is much lower for the 6 bar case, for which SOI was heavily constrained due to high pressure rise rate at early injection. Ignition delay is affected by H2int but primarily SOI. MPRR peaks near SOI=-14 for IMEP=2, 3, 4 bar.

Chapter 5

HDDF Heat Release Characteristics[1]

5.1 Overview of Results

Heat release in diesel engines [9, 43, 44] and dual-fuel engines [40, 42, 45, 46] has been shown to progress in several stages.

For a single diesel injection without a second fuel, injected through a central nozzle without prechamber and without wall impingement, three main phases occur [9]. Fig 5.1 shows these phases. Some portion of the fuel will evaporate before igniting. After a delay period, combustion of this premixed portion will cause a sharp initial peak. After this peak, the heat release is rate-limited by the mixing of fuel with air [9, 43]. A late phase of combustion occurs after the two main events.

After injection but before combustion, as some portion of fuel evaporates, a small amount of negative heat release wil be observed [9, 43] (not included in Fig. 5.1).

Heat release in engines, both spark-ignited and diesel, is often modelled as one or more Wiebe functions [106]. For hydrogen-diesel dual fuel operation, heat release has been modelled as the superposition of four Wiebe functions [46].

In this chapter, heat release profiles are explored starting with diesel pilot injections only, and no hydrogen, at different DOI and SOI. This is done as a baseline to compare

---

[1] Elements of this chapter have been published at the 2025 meeting of the Combustion Institute - Canadian Section [146].

with dual-fuel operation. Hydrogen is then added as volume fraction in intake air (H2int) in different amounts to produce a load of IMEP=2 to 6 bar. These heat release profiles correspond to the testing performed in Section 4.6. Heat release for dual-fuel operation at IMEP=2, 3, and 6 bar and varying Hydrogen Energy Share (HES) is explored, providing further insight into the results in Sections 4.4 and 4.5. A chapter overview is given in Table 5.1.

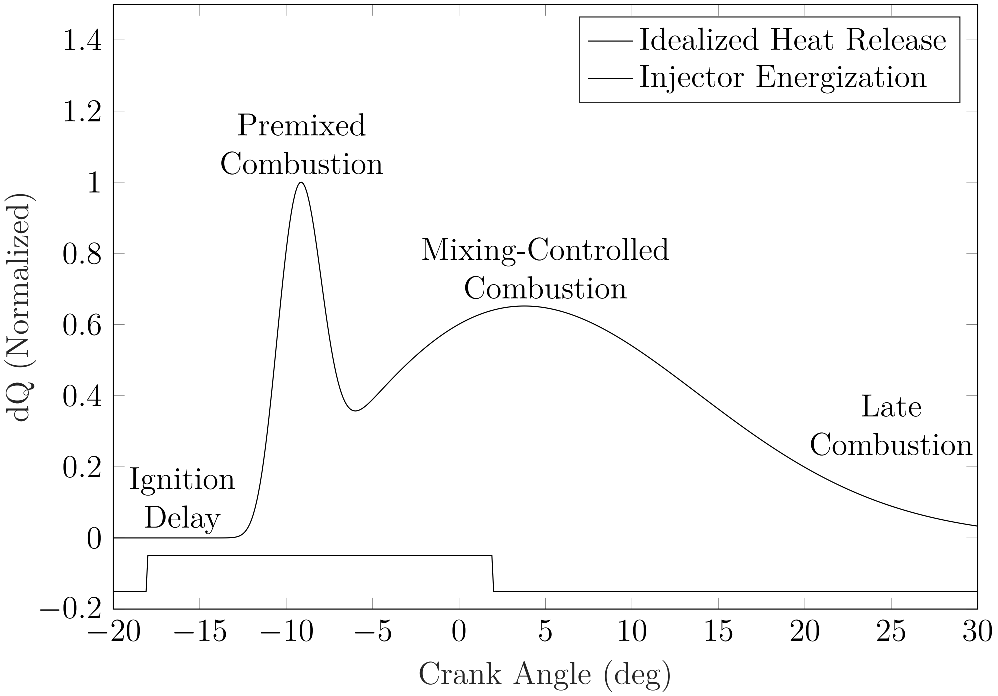

Figure 5.1: Idealized Heat Release for a Single Central Diesel Injection. Names Given to Phases are from Heywood [9]

Table 5.1: Overview of Heat Release Results

Section	Test	Purpose
5.2	Diesel Pilot only at SOI=-4	Baseline diesel-only combustion
5.3	Diesel Pilot only, earlier SOI	Baseline at earlier SOI
5.4	Dual-Fuel with minimum pilot	Corresponds to Section 4.6
5.5	Dual-Fuel with varying HES	Corresponds to Sections 4.4 and 4.5

5.2 Diesel Pilot Only, SOI=-4

Fig. 5.2 shows heat release patterns for a single diesel injection at SOI=-4 and different injection durations. This will form a baseline for the dual-fuel results. Heat release from a motoring trace is also shown for comparison. Injector energization profile is also shown for the two extremes of 0.17 and 0.35 ms duration. The smallest results in IMEP≈0, while the largest results in IMEP≈1.5 bar. Diesel injection durations are chosen to correspond to the dual-fuel testing in Chapter 4.

The evaporation phase, “A”, is visible in Fig. 5.2. The negative heat release in stage “A” was compared to fuel vaporization. For the largest injection (DOI=0.35 ms), the total heat release of phase “A” was summed. For accuracy, the motoring heat release was subtracted. This was compared to the heat of vaporization of dodecane, finding that 30mg of liquid fuel would have evaporated. The entirety of the remaining heat release is 440 J, corresponding to 10 mg fuel combusted, an amount confirmed by exhaust analysis. Therefore, some other factor (such as gas dynamics) must account for the size of the dip in phase “A”. Here it is speculated that the dip in Fig. 5.2, as well as being due to fuel evaporation, is accentuated by the high pressure fuel jet blowing air into the piston bowl, locally reducing pressure at the sensor (located in the cylinder head).

The next phase, “B”, is attributed to premixed combustion of that portion of diesel fuel that evaporated. Both magnitude and duration of this phase increase with increasing diesel injection.

Phase “C” is reserved for diffusion-limited combustion. A slight downward trend is observed between 12–20 CAD, which may be a small contribution of this phase. At these tested light-load conditions, if this phase is present it is obscured by cylinder ringing.

Phase “D” is reserved for hydrogen combustion, and is not present in Fig. 5.2. This stage is further discussed in Section 5.4 when hydrogen is added.

Phase “E” is regarded as the late stage combustion process and makes up a relatively small proportion of total heat release.

These phases are summarized in Table 5.2

Table 5.2: Labels Used for Phases of Dual-Fuel Heat Release

Dual-Fuel Phase	Name in Heywood and Fig. 5.1	Description
“A”	—	Fuel Evaporation
“B”	Premixed Combustion	Premixed Diesel
“C”	Mixing-Controlled Combustion	Mixing-Limited Diesel
“D”	—	Hydrogen Combustion
“E”	Late Combustion	Late or Tail Stage

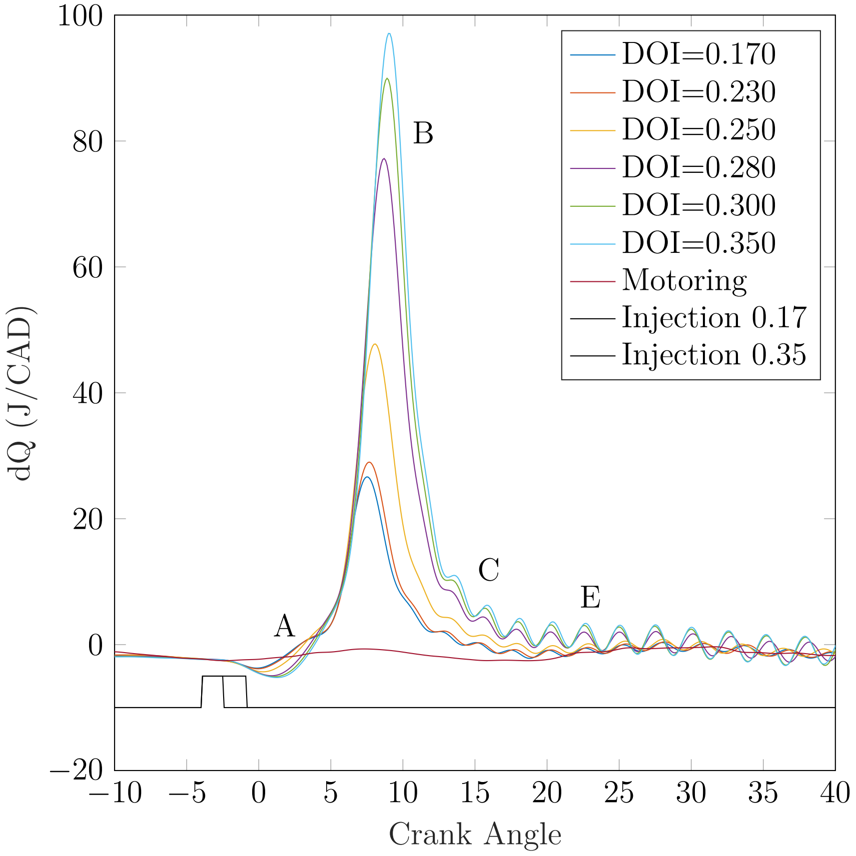

Figure 5.2: Heat Release Profiles with No Hydrogen, Fixed SOI=-4 and Varying DOI.

5.3 Diesel Pilot Only, Earlier Injection Timing

The heat release profiles obtained with diesel injection only at different SOI are shown in Fig. 5.3 and Fig. 5.4. For better comparison between different SOI, the horizontal axis is shifted to represent crank angle after injection. The vertical axis is also shifted to place the value of heat release at a consistent zero point, overlaying the curves at different SOI. Injector enable signal is also shown below the heat release curves for reference.

In Fig. 5.3, diesel DOI is set to 0.35 ms. Similar stages to Fig. 5.2 are seen. A dip is seen approximately 4–5 CAD after injection, corresponding the “A” phase. For SOI=-14, compared to SOI=-4, the main heat release (“B”) is slightly earlier and sharper. For SOI=-29, the “A” phase is extended and there is a small peak near 25 degrees after injection. The main heat release is slower at SOI=-29 than either SOI=-4 or SOI=-14. Later stages (“C”, “E”) do not appear to be present to a significant extent.

In Fig. 5.4, DOI is set to 0.17ms. Heat release curves obtained at SOI=-4 and SOI=-9 show very similar trends, both to each other and to the DOI=0.35ms case. As SOI is advanced from -4 to -9 CAD, ignition delay decreases and heat release is sharper. As SOI is further advanced to SOI=-19 and -24, ignition delay increases and heat release spreads out. At SOI=-24 the total heat release is significantly less, showing poor combustion on the edge of misfire. At SOI=-29, the diesel injection failed to ignite and so SOI=-29 is not included here.

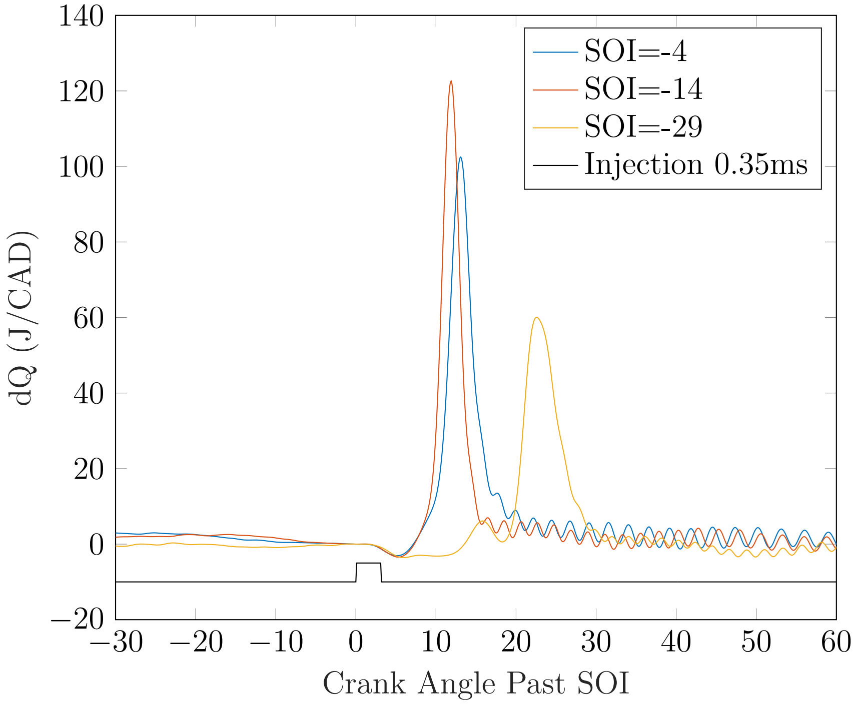

Figure 5.3: Diesel Heat Release Profiles with DOI=0.35ms. For SOI={-4, -14, -29} Peak Heat Release Rate Occurs at Crank Angle Location={9.1,-2.1,-6.4} CAD

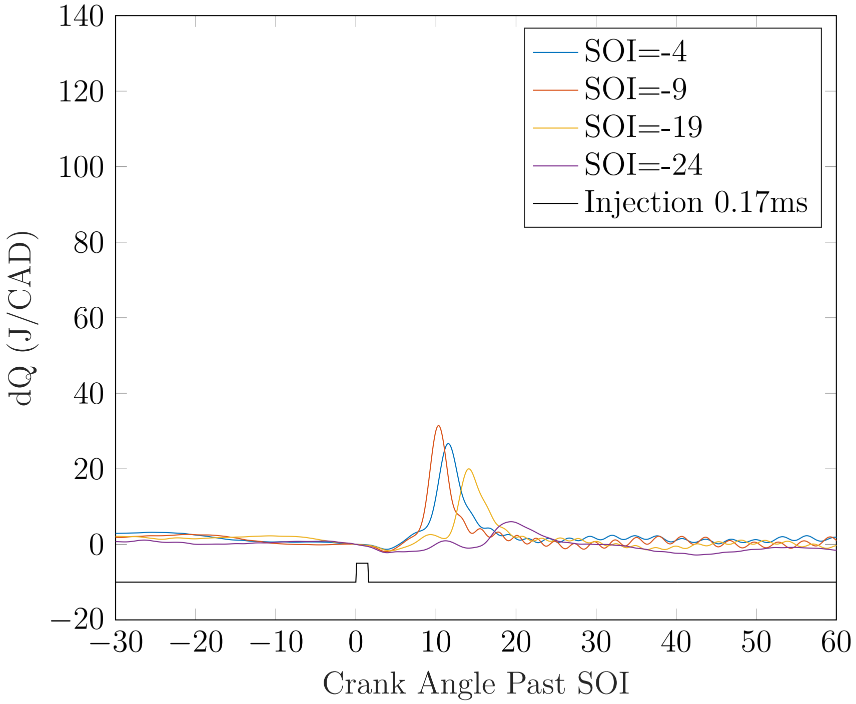

Figure 5.4: Diesel Heat Release Profiles with DOI=0.17ms. For SOI={-4, -9, -19, -24}, Peak Heat Release Rate Occurs at Crank Angle Location={7.5,1.3,-4.9,-4.7} CAD

5.4 Hydrogen-Diesel Dual-Fuel Operation with Minimum Pilot Injection

The main goal of hydrogen-diesel dual-fuel operation is a reduction in carbon dioxide emissions, creating a strong incentive to minimize the diesel DOI. The minimum diesel DOI that would reliably ignite across a range of operating points was determined to be 0.17 ms. This minimum injection is consistent with Fig. 5.2 and Fig. 5.4. These minimum-pilot tests are the same as those in Section 4.6.

In this testing, the engine was run in dual-fuel mode using a 0.17ms pilot injection and SOI=-4. Hydrogen was added at different concentrations (H2int=6.1–9.3 Vol%) to meet a target of 2, 3, or 4 bar IMEP. Hydrogen Energy Share (HES) varies from 78–86%. Heat release rate is shown in Fig. 5.5.

The first stage, “A”, is relatively consistent across the different hydrogen amounts. Compared to the diesel-only case, the transition to phase “B” is slightly retarded by hydrogen.

Peak heat release rate within the premixed diesel (“B”) phase, is slightly increased and slightly (2 degrees) retarded when hydrogen is added compared to the diesel-only case. This retarding effect may partially be due to lowered overall volumetric efficiency due to airflow stalling in the intake runner [41], slightly lowering the cylinder pressure prior to injection (Fig. 2.11). This stage makes up the peak heat release rate for all but the highest-hydrogen case. Between the three hydrogen-containing cases, the upward slope of this phase is consistent. The peak of this stage is raised by hydrogen addition, however this phase is less affected than others.

Stage “C” or mixing-limited combustion, if present, is obscured by hydrogen addition.

The main effect of hydrogen at these operating conditions is to create a separate phase, here labelled “D”. This appears to start concurrently with “C”, adding to the total heat release rate, but lasts for a longer time and contributes more to the total heat release. For H2int=6.1%, this stage continues to about 40 CAD. Moving to H2int=7.4%, increases but does not lengthen this stage, and some effect of stage "C" is still present. At the highest H2int=9.3%, stage "D" starts to increase beyond stage "B" and drive the peak heat release.

Stage "E", late or tail-stage combustion, is also increased by hydrogen compared to diesel-only.

These results can be compared to recent literature. Using a factory-configuration diesel ECU and adding hydrogen, a dual-peak heat release rate was obtained [46]. The injection strategy of the ECU was not given but is assumed to consist of two or more injections. Four main stages were present. At IMEP=4.7 bar, the premixed peak dominates peak heat release and "diesel main" is relatively small. The effect of hydrogen addition is to slightly lengthen the "diesel main" phase. However at IMEP=9.6 bar, two peaks are visible. Similar to the results in Fig. 5.5, the initial peak was somewhat consistent with hydrogen addition. A large "diesel main" stage was present due to larger diesel useage, which is not present in Fig. 5.5. In their tests, the"diesel main" overlaps with the hydrogen phase, which may explain the large peak on addition of modest concentrations of hydrogen (maximum H2int=8% at HES=35% and IMEP=9.6) compared to the lower-diesel and lower-load tests in Fig. 5.5.

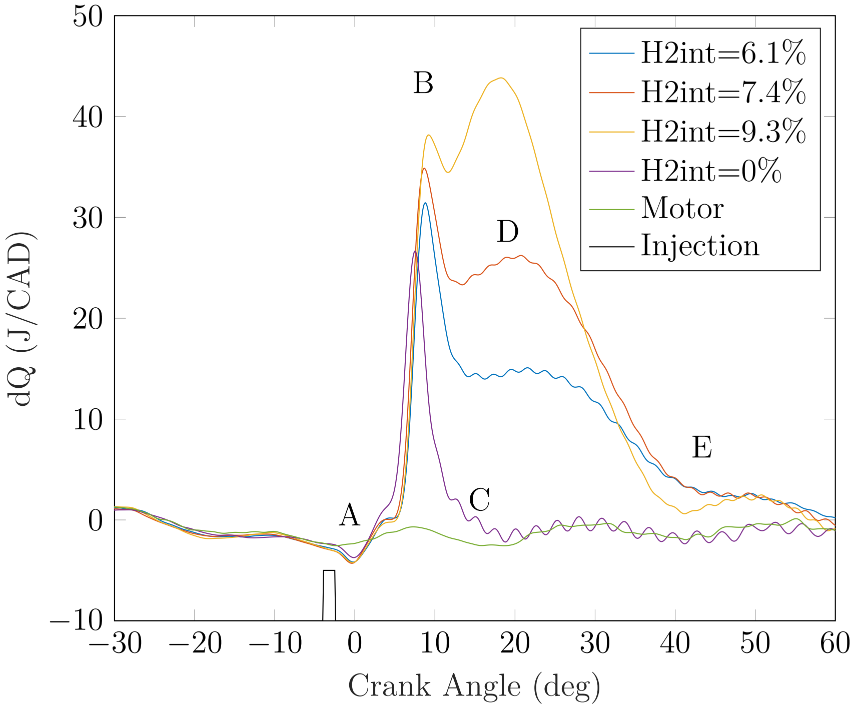

Figure 5.5: Dual-Fuel Operation with Consistent Pilot: SOI=-4 aTDC, DOI=0.17 ms, Varying IMEP={2,3,4} bar

The same maximum-HES operation as Fig. 5.5 was extended to IMEP=6 bar where H2int=13.3%. At this point HES=89%. Heat release rate is plotted in Fig. 5.6. Due to fast pressure rise rates, 6 bar operation was only conducted at SOI=-4 and not SOI=-9 and earlier. A slight increase is visible approximately 6 degrees after SOI, within the“A” stage, similar to the lower load cases but arriving sooner by about 2 degrees. The main combustion event has higher peak heat release than any phase at the other lower loads. Further stages are obscured. At IMEP=6 bar, hydrogen slip is low (see Section 4.6).

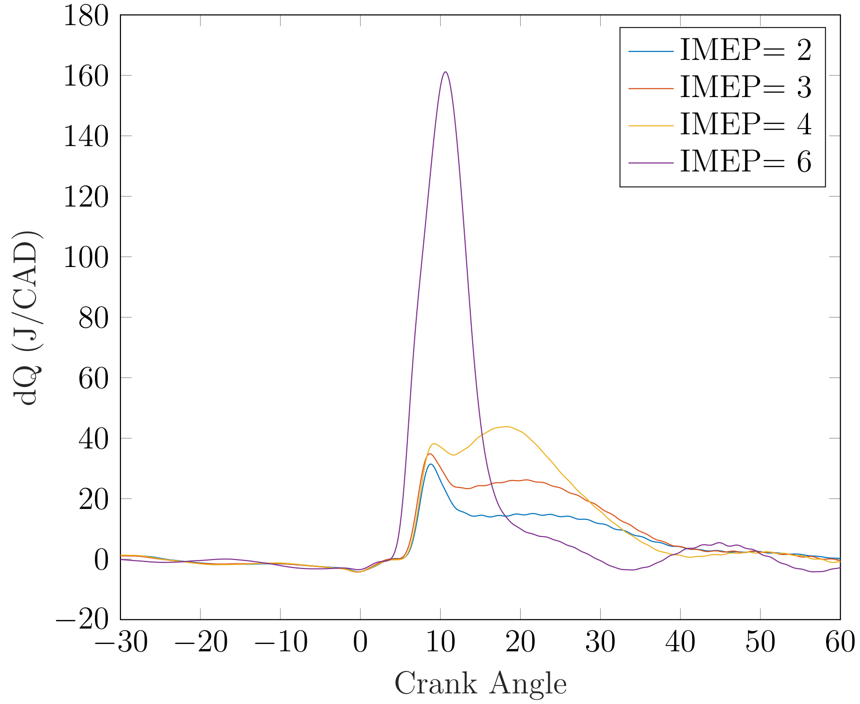

Figure 5.6: Dual-Fuel Operation with Consistent Pilot: SOI=-4, DOI=0.17 ms, Comparing 6 bar (H2int=13.3% and HES=89%) to Lower Loads

The effect of varied SOI on these minimum-DOI points was also investigated with Fig. 5.7 showing the heat release profiles obtained with varied SOI and consistent IMEP=4. The SOI=-4 case for Fig. 5.7 is the same as the IMEP=4 case in Fig. 5.5. Similarly to Fig. 5.4, the horizontal axis is shifted to represent crank angle after injection and the vertical axis is shifted to place the value at SOI at a consistent location and overlap the heat release curves for better comparison.

For the SOI=-4 case, discussed previously, all 5 stages are visible. For earlier injection at SOI=-19, the first stage is still visible at a consistent time delay from injection. However “B” and “D” merge together to create one peak. The rising slope of “B” is consistent between SOI=-4 and SOI=-19. The lower combustion chamber volume near TDC (compared to near 20 aTDC) may force combustion to progress more quickly. The result is a higher peak heat release and an overlap of the stages, with “E” again relatively small.

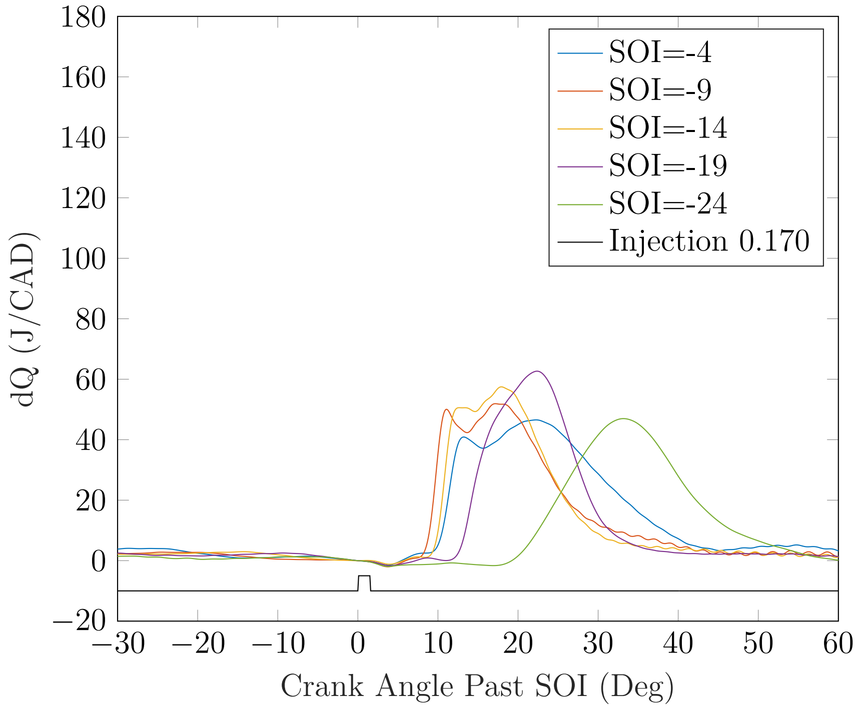

Figure 5.7: IMEP=4 bar points with DOI=0.17 and SOI varied

5.5 Varying HES at Consistent IMEP

Some on-road applications retrofit diesel engines by adding port-injected hydrogen but retaining the stock ECU for diesel injection [32, 46]. In that application, the diesel DOI cannot be constrained to a minimum. In these tests, a diesel injection duration is chosen and hydrogen added to meet a load setpoint of IMEP={3,4,6} bar. SOI is kept at {-4,-14,-24,-34} for the lower loads. For the highest load (IMEP=6 bar), SOI=-1 was chosen, with earlier SOI creating high MPRR combustion and later SOI resulting in misfire. These tests are the same tests as Section 4.4 and Section 4.5, and to be consistent with these prior sections, results are presented in terms of Hydrogen Energy Share at a constant load.

Fig. 5.8 shows the results for 3 bar at SOI=-4 and HES={50,71,82}%. Stage “A” is clearly visible. As HES is reduced (diesel increased) this stage becomes more pronounced, consistent with Fig. 5.2 and Fig. 5.5. In the “B” stage, a greater diesel injection will increase and slightly retard this stage's peak (Fig. 5.2). To a smaller extent, less hydrogen will slightly lessen and advance this peak (Fig. 5.5). In these constant-load tests, as diesel is increased the hydrogen is reduced. Fig. 5.8 shows the effect of diesel dominating, with a larger injection increasing and retarding the "B" stage. This results in greater MPRR (as shown in Fig. 4.21). Again with reference to Fig. 5.8, for HES={82, 71}%, stage "D" is visible and increased by hydrogen. For HES=50%, the remaining combustion is low and slow, making it difficult to distinguish as the tail phase "E".

Advancing SOI to SOI=-14, results in similar patterns in heat release rate. Fig. 5.9 shows the curves obtained. Compared to the SOI=-4 case, Stage "B" occurs earlier and closer to TDC. It also results in higher peak heat release. This is seen in Fig. 4.21 where the SOI=-14 cases tend to result in higher MPRR than SOI=-4 for consistent HES.

In Fig. 5.9, further advancing SOI to SOI=-24 changes the heat release pattern for the high-HES points. While for HES=42% the pattern is similar, for HES=71% the "B", "C" and "D" phases combine together. For HES=84%, the combustion happens in a single phase, with peak near 8 CAD. This is delayed and peak heat release is reduced compared to the lower-HES cases.

Fig. 5.11 presents the earliest timing case of SOI=-34. The operational range at this SOI is limited, thus only HES=44% and HES=50% were tested. Lower HES (larger diesel) resulted in unacceptable MPRR, and higher HES (lower diesel) resulted in misfire. The combustion occurs as a single peak. In contrast to prior results, higher diesel results in a lower and slower heat release. This effect is replicated at SOI=34 for 4 bar cases. However it is difficult to draw conclusions as to the effect of diesel vs hydrogen as both combust without visibly separated phases at this advanced SOI.

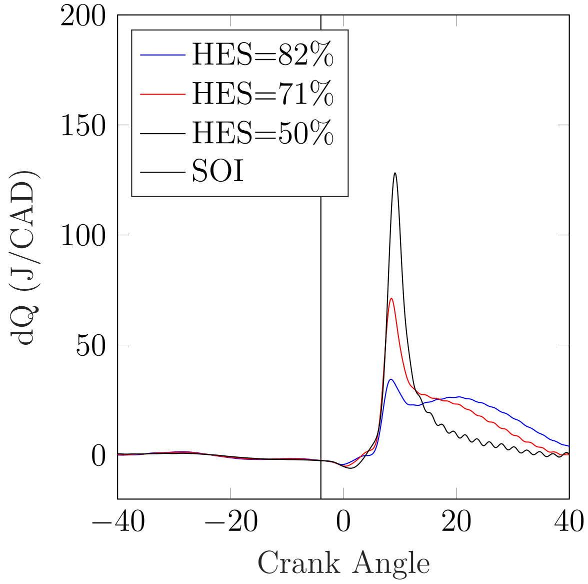

Figure 5.8: Heat Release Rates at Varying HES, SOI=-4, IMEP=3 bar

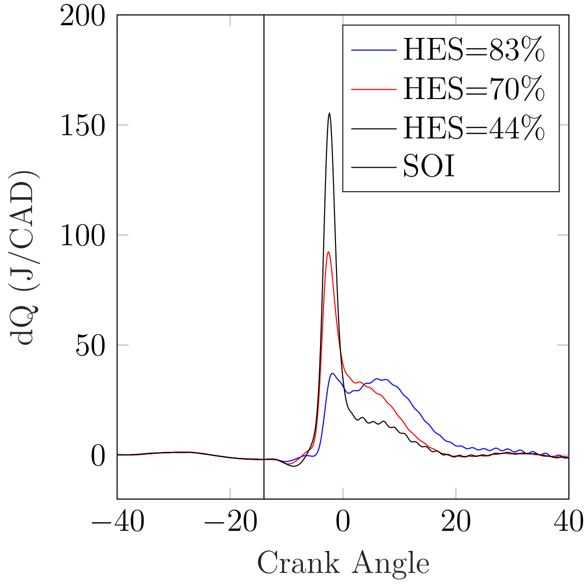

Figure 5.9: Heat Release Rates at Varying HES, SOI=-14, IMEP=3 bar

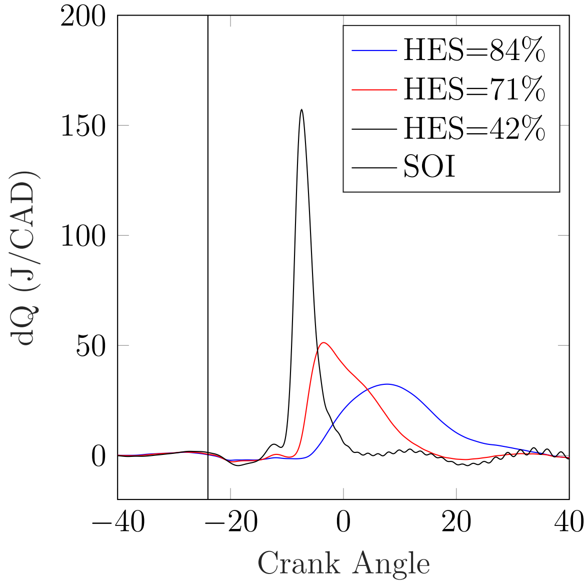

Figure 5.10: Heat Release Rates at Varying HES, SOI=-24, IMEP=3 bar

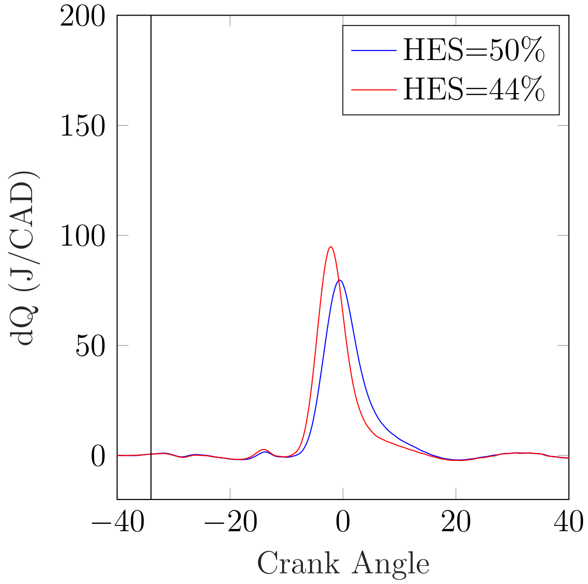

Figure 5.11: Heat Release Rates at Varying HES, SOI=-34, IMEP=3 bar

Increasing IMEP to 4 bar, from the previous 3 bar, results in similar characteristics. Heat release curves for 4 bar operation are presented in Fig. 5.12, 5.13, 5.14, 5.15.

At SOI=-4, shown in Fig. 5.12, the trends are similar to those at 3 bar. Compared to IMEP=3, the IMEP=4 cases at SOI=-4 have a more pronounced "D" phase.

Advancing timing to SOI=-14, shown in Fig. 5.13, the combustion shows distinct stages while being compressed. All tested points are at relatively low diesel amounts (high HES) as larger diesel injections resulted in unacceptable pressure rise rates. The “A” stage is relatively unaffected. The “B” stage is slightly compressed, and leads directly into the “D” stage. The “D” stage is greatly compressed, resulting in shorter but faster heat release. This is somewhat similar to, but more pronounced than Fig 5.9. Both stages (“B” and “D”) occur near to TDC where cylinder volume is low and temperatures resulting from combustion are high.

Fig. 5.14 shows the patterns obtained at IMEP=4 and SOI=-24. Similarly to the IMEP=3 case, high HES (low diesel) results in delayed combustion with the stages blending together, in contrast to lower HES (higher diesel) where distinct stages are observed.

At SOI=-34, presented in Fig. 5.14, all the tested cases have combustion that blends into a single peak. Similarly to the IMEP=3 tests at this SOI, but in contrast to the results at other SOI, higher diesel and lower HES result in lessened peak heat release.

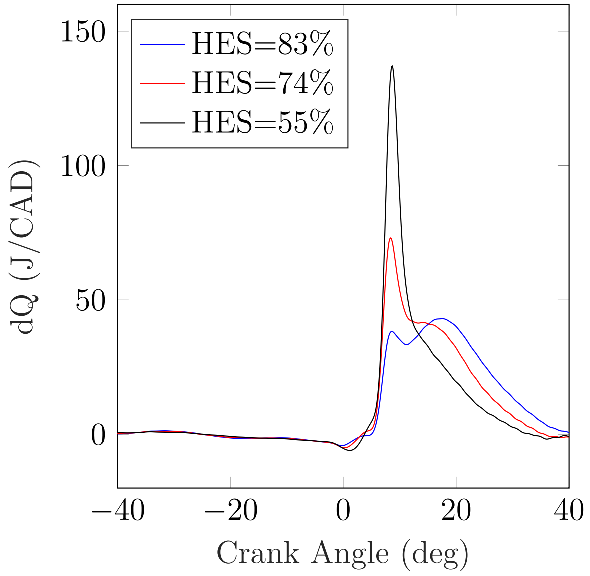

Figure 5.12: Heat Release Rates at Varying HES, SOI=-4 and IMEP=4 bar

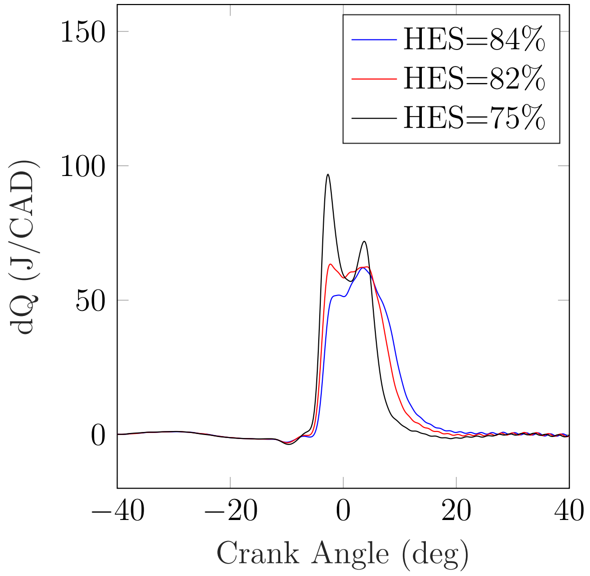

Figure 5.13: Heat Release Rates at Varying HES, SOI=-14 and IMEP=4 bar

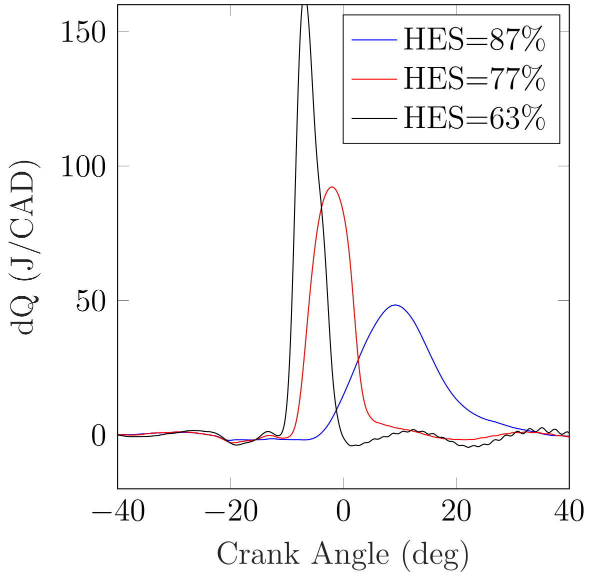

Figure 5.14: Heat Release Rates at Varying HES, SOI=-24 and IMEP=4 bar

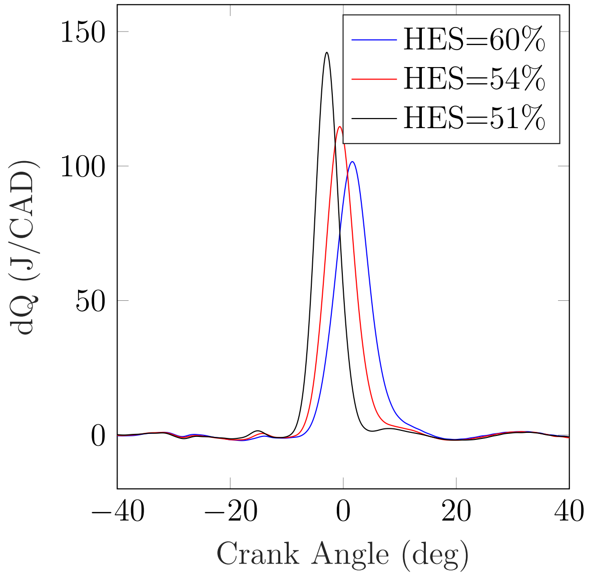

Figure 5.15: Heat Release Rates at Varying HES, SOI=-34 and IMEP=4 bar

Tests at IMEP=6 are constrained to a single SOI, later than the other tests. SOI=-1 was chosen as giving a reasonable operating range of DOI. Earlier SOI resulted in large pressure rise rates, while later SOI resulted in misfire at low diesel DOI.

Fig. 5.16 shows some similarities to the other tests at IMEP=3 and IMEP=4. The “A” phase is present, but for the lowest HES=42% the transition to subsequent phases is much quicker. The “C” phase is again not present. However there does not appear to be a separate “B” and “D” phase. Instead, the main combustion is completed in a single fast peak with high peak heat release. For HES=42% and HES=66%, higher diesel injection increases peak heat release but without a separate “B” phase. For HES=82%, an asymmetric pattern emerges where “B” and “D” may be beginning to separate. This higher load point (IMEP=6) is associated with both higher diesel and higher hydrogen. Notably, the pattern observed for IMEP={3,4} where increasing HES decreases peak heat release, is observed at IMEP=6 despite the higher H2int (up to 13.3%). Testing at lower diesel injection was not possible due to misfire.

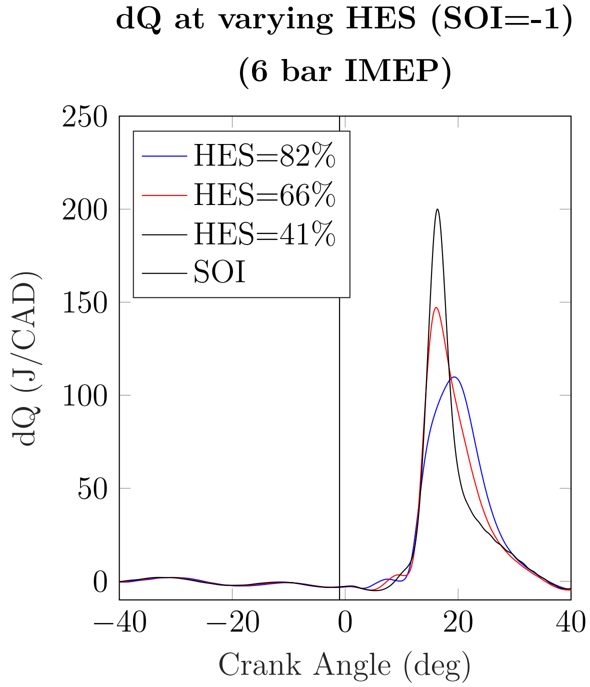

Figure 5.16: Heat Release Rates at Varying HES, SOI=-1, IMEP=6 bar

5.6 Summary of Heat Release Results

At SOI=-4 and IMEP={2, 3, 4} bar, five stages of heat release are observed. The first, “A”, occurs with diesel injection and is believed to be a combination of fuel evaporation and pressure wave from the injector. The next, “B”, is directly dependent on diesel DOI but not strongly dependent on H2int. At most points this phase dominates peak heat release. Phase “C”, diffusion-limited diesel combustion, is not observed in this testing. Hydrogen addition creates a distinct phase “D”. A tail of late combustion, “E”, is observed but contributes a relatively small portion to the heat release. The main drivers of heat release are phase “B”, largely dependent on diesel, and phase “D”, largely dependent on hydrogen.

At higher H2int, corresponding to high HES and IMEP=6, the main combustion progresses as a single peak with large heat release. High pressure rise rates are encountered at early SOI.

For earlier SOI at IMEP=2, 3, and 4 bar, the phases of combustion also tend to blend together.

The large peak in heat release due to diesel injection (Phase “B”), helps explain why in Sections 4.4 and 4.5 maximizing HES minimized MPRR in those tests.

Chapter 6

Conclusions and Future Work

6.1 Conclusions

A port-injected hydrogen-diesel dual fuel (HDDF) engine was operated at low load in naturally-aspirated condition using a single diesel pilot injection to ignite the hydrogen fuel. Emissions of unburned hydrogen were measured using a commercial, low-cost sensor that was characterized for cross-sensitivity to common engine exhaust components. Calculated CO_2 equivalent totals are presented, taking into account the global warming effect of unburned hydrogen. Heat release patterns are calculated in order to qualitatively understand dual-fuel combustion.

The sensor used for exhaust hydrogen measurement was characterized using a high-accuracy flow rig. This catalytic-combustion sensor requires oxygen to measure hydrogen, with low oxygen resulting in the sensor output saturating at a value that depends on the oxygen concentration. Above 8 vol% of oxygen the sensor gives correct readings. Between 8 – 20 vol% oxygen and 0 – 3 % hydrogen the RMS accuracy is 0.04 H2%. Cross-sensitivities to unburned hydrocarbons (propane), nitric oxide, and carbon dioxide are negligible for the tested ranges. A linear cross-sensitivity to carbon monoxide is found and sensor readings are compensated for this effect.

In the HDDF engine with constant diesel DOI=0.23ms, emissions of unburned hydrogen are strongly dependent on intake hydrogen fuel-air ratio (H2int), with peak exhaust concentration (H2exh) occurring with H2int≈3–5%. In the range H2int≈2–7%, H2exh is dependent on injection timing (SOI), but SOI has less effect with higher H2int.

The engine was operated with variable hydrogen energy share (HES) at loads of {3,4,6} bar IMEP. At 3 bar IMEP, the CO_2 equivalent emissions were dependent on SOI. For 4 and 6 bar IMEP, SOI made relatively little difference to the CO_2 equivalent emissions. At all loads and SOI, total CO_2 equivalent emissions were monotonically reduced by maximizing HES. Maximum Pressure Rise Rate (MPRR) is dependent on SOI but is decreased at all points by maximizing HES.

The engine was operated with the minimum reliable diesel pilot injection, achieving HES=78–89%. Operation at IMEP=2 bar was possible but showed high hydrogen slip, significantly affecting thermal efficiency. Operation at 2 bar IMEP also showed inconsistent exhaust emissions compared to higher loads. Compared to 2 bar IMEP, operation at 3, ,4, and 6 bar IMEP showed much reduced slip. With the diesel pilot held constant, for IMEP=2, 3, and 4 bar, MPRR was strongly dependent on SOI.

Five stages of heat release are observed at SOI=-4. The first stage is believed to be a combination of fuel evaporation and pressure wave caused by the injector. The next stage is most strongly dependent on injected diesel fuel quantity. With high diesel and low hydrogen, this stage contains the peak heat release for the profile and helps to explain the decrease in MPRR with increasing HES. A small third stage is visible both for diesel pilot and dual-fuel operation. The fourth stage is driven by hydrogen. A small fifth stage of late combustion is present. For high H2int and/or early SOI, the combustion stages tend to merge together.

6.2 Future Work

Several important parameters have been investigated for their effects on port-injected hydrogen-diesel dual-fuel operation at high Hydrogen Energy Share values. Hydrogen slip has been quantified for this engine, and heat release rate profiles and patterns have been presented. Several possible directions for future research include:

- A dual-injection strategy can be used to increase power while staying within MPRR limits, by igniting a premixed hydrogen combustion phase then following up with another diesel injection after the hydrogen heat release is complete.
- Engine boost can be used to reduce hydrogen fuel ratio and therefore combustion speed.
- Throttled operation, in conjunction with a high-reactivity fuel, can be used to increase hydrogen fuel ratio thereby decreasing slip.
- EGR can be used to reduce peak cylinder temperatures.

References

[1] Government of Canada, *2030 emissions reduction plan*, Accessed 2024-10-24, 2022. [Online]. Available: Website:https://www.canada.ca/en/environment-climate-change/news/2022/03/2030-emissions-reduction-plan--canadas-next-steps-for-clean-air-and-a-strong-economy.html.

[2] United States Department of State and the United States Executive Office of the President, *The long-term strategy of the United States: Pathways to net-zero greenhouse gas emissions by 2050*, 2021.

[3] European Commission, *European climate law*, website, accessed 2024-10-24, 2024. [Online]. Available: https://climate.ec.europa.eu/eu-action/european-climate-law_en.

[4] G. G. Njema, R. B. O. Ouma, and J. K. Kibet, "A review on the recent advances in battery development and energy storage technologies," *Journal of Renewable Energy*, vol. 2024, P. V., Ed., pp. 1–35, May 2024, ISSN: 2314-4386. DOI: 10.1155/2024/2329261.

[5] A. Soleimani *et al.*, "Progress in hydrogen fuel cell vehicles and up-and-coming technologies for eco-friendly transportation: An international assessment," *Multiscale and Multidisciplinary Modeling, Experiments and Design*, vol. 7, no. 4, pp. 3153–3172, May 2024, ISSN: 2520-8179. DOI: 10.1007/s41939-024-00482-8.

[6] R. D. Reitz *et al.*, "IJER editorial: The future of the internal combustion engine," *International Journal of Engine Research*, vol. 21, no. 1, pp. 3–10, Sep. 2019, ISSN: 2041-3149. DOI: 10.1177/1468087419877990.

[7] A Onorati *et al.*, "The role of hydrogen for future internal combustion engines," *International Journal of Engine Research*, vol. 23, no. 4, pp. 529–540, Mar. 2022, ISSN: 2041-3149. DOI: 10.1177/14680874221081947.

[8] E. Eckermann, *World History of the Automobile.* SAE International, Sep. 2001, ISBN: 9780768008005. DOI: 10.4271/r-272.

[9] J. B. Heywood, *Internal Combustion Engine Fundamentals*, J. P. Holman, Ed. McGraw-Hill, Inc, 1988, ISBN: 0-07-028637-X.

[10] F. S. AlHumaidan, M. Absi Halabi, M. S. Rana, and M. Vinoba, "Blue hydrogen: Current status and future technologies," *Energy Conversion and Management*, vol. 283, p. 116 840, May 2023, ISSN: 0196-8904. DOI: 10.1016/j.enconman.2023.116840.

[11] F. Kourougianni *et al.*, "A comprehensive review of green hydrogen energy systems," *Renewable Energy*, vol. 231, p. 120 911, Sep. 2024, ISSN: 0960-1481. DOI: 10.1016/j.renene.2024.120911.

[12] E. Hand, "Hidden hydrogen," *Science*, vol. 379, no. 6633, pp. 630–636, Feb. 2023, ISSN: 1095-9203. DOI: 10.1126/science.adh1477.

[13] E. M. Yedinak, "The curious case of geologic hydrogen: Assessing its potential as a near-term clean energy source," *New Scientist*, 2022.

[14] J. Dinneen, "Gaseous gold," *New Scientist*, 2024.

[15] S. Verhelst, P. Maesschalck, N. Rombaut, and R. Sierens, "Increasing the power output of hydrogen internal combustion engines by means of supercharging and exhaust gas recirculation," *International Journal of Hydrogen Energy*, vol. 34, no. 10, pp. 4406–4412, May 2009, ISSN: 0360-3199. DOI: 10.1016/j.ijhydene.2009.03.037.

[16] R. J. Natkin, X. Tang, K. M. Whipple, D. M. Kabat, and W. F. Stockhausen, "Ford hydrogen engine laboratory testing facility," in *SAE Technical Paper Series*, ser. ANNUAL, SAE International, Mar. 2002. DOI: 10.4271/2002-01-0241.

[17] T. Tsujimura and Y. Suzuki, "Development of a large-sized direct injection hydrogen engine for a stationary power generator," *International Journal of Hydrogen Energy*, vol. 44, no. 22, pp. 11 355–11 369, Apr. 2019, ISSN: 0360-3199. DOI: 10.1016/j.ijhydene.2018.09.178.

[18] H Homan, R Reynolds, P DeBoer, and W McLean, "Hydrogen-fueled diesel engine without timed ignition," *International Journal of Hydrogen Energy*, vol. 4, no. 4, pp. 315–325, 1979, ISSN: 0360-3199. DOI: 10.1016/0360-3199(79)90006-5.

[19] M Shahbakhti and C. R. Koch, "Characterizing the cyclic variability of ignition timing in a homogeneous charge compression ignition engine fuelled with n-heptane/iso-octane blend fuels," *International Journal of Engine Research*, vol. 9, no. 5, pp. 361–397, Oct. 2008, ISSN: 2041-3149. DOI: 10.1243/14680874jer01408.

[20] M. Shahbakhti, R. Lupul, and C. R. Koch, "Cyclic variations of ignition timing in an HCCI engine," in *ASME/IEEE 2007 Joint Rail Conference and Internal Combustion Engine Division Spring Technical Conference*, ser. JRC-ICE2007, ASMEDC, Jan. 2007, pp. 405–415. DOI: 10.1115/jrc/ice2007-40032.

[21] S. S. Goldsborough and P. Van Blarigan, "A numerical study of a free piston ic engine operating on homogeneous charge compression ignition combustion," in *SAE Technical Paper Series*, ser. ANNUAL, SAE International, Mar. 1999. DOI: 10.4271/1999-01-0619.

[22] P. A. Caton and J. T. Pruitt, “Homogeneous charge compression ignition of hydrogen in a single-cylinder diesel engine,” *International Journal of Engine Research*, vol. 10, no. 1, pp. 45–63, Feb. 2009, ISSN: 2041-3149. DOI: 10.1243/14680874jer02208.

[23] O. Stenlåås, M. Christensen, R. Egnell, B. Johansson, and F. Mauss, “Hydrogen as homogeneous charge compression ignition engine fuel,” in *SAE Technical Paper Series*, ser. SFL, SAE International, Jun. 2004. DOI: 10.4271/2004-01-1976.

[24] T. Noda and D. E. Foster, “A numerical study to control combustion duration of hydrogen-fueled HCCI by using multi-zone chemical kinetics simulation,” in *SAE Technical Paper Series*, ser. ANNUAL, SAE International, Mar. 2001. DOI: 10.4271/2001-01-0250.

[25] T. Tsujimura, S. Mikami, N. Achiha, Y. Tokunaga, J. Senda, and H. Fujimoto, “A study of direct injection diesel engine fueled with hydrogen,” *SAE Transactions , 2003, Vol. 112, Section 4: Journal of Fuels and Lubricants (2003), pp. 390-405*, 2003.

[26] J. Gomes Antunes, R. Mikalsen, and A. Roskilly, “An experimental study of a direct injection compression ignition hydrogen engine,” *International Journal of Hydrogen Energy*, vol. 34, no. 15, pp. 6516–6522, Aug. 2009, ISSN: 0360-3199. DOI: 10.1016/j.ijhydene.2009.05.142.

[27] S Furuhama and Y Kobayashi, “Development of a hot-surface-ignition hydrogen injection two-stroke engine,” *International Journal of Hydrogen Energy*, vol. 9, no. 3, pp. 205–213, 1984. DOI: 10.1016/0360-3199(84)90120-4.

[28] M. Aliramezani, I. Chitsaz, and A. A. Mozafari, “Thermodynamic modeling of partially stratified charge engine characteristics for hydrogen-methane blends at ultra-lean conditions,” *International Journal of Hydrogen Energy*, vol. 38, no. 25, pp. 10 640–10 647, Aug. 2013, ISSN: 0360-3199. DOI: 10.1016/j.ijhydene.2013.05.172.

[29] X. Liu, G. Seberry, S. Kook, Q. N. Chan, and E. R. Hawkes, “Direct injection of hydrogen main fuel and diesel pilot fuel in a retrofitted single-cylinder compression ignition engine,” *International Journal of Hydrogen Energy*, vol. 47, no. 84, pp. 35 864–35 876, Oct. 2022, ISSN: 0360-3199. DOI: 10.1016/j.ijhydene.2022.08.149.

[30] P. Rorimpandey *et al.*, “Hydrogen-diesel dual-fuel direct-injection (H2DDI) combustion under compression-ignition engine conditions,” *International Journal of Hydrogen Energy*, vol. 48, no. 2, pp. 766–783, Jan. 2023, ISSN: 0360-3199. DOI: 10.1016/j.ijhydene.2022.09.241.

[31] A. Boretti, “A dual fuel ICE Diesel-H2 featuring 1,600 bar cryogenic liquid H2 injection,” *International Journal of Hydrogen Energy*, vol. 46, no. 36, pp. 19 171–19 179, May 2021, ISSN: 0360-3199. DOI: 10.1016/j.ijhydene.2021.03.048.

[32] M. Guan *et al.*, "Characterizing hydrogen-diesel dual-fuel performance and emissions in a commercial heavy-duty diesel truck," *International Journal of Hydrogen Energy*, vol. 86, pp. 1085–1096, Oct. 2024, ISSN: 0360-3199. DOI: 10.1016/j.ijhydene.2024.08.480.

[33] C. Government, "Transportation in Canada 2022," Canadian Government, Tech. Rep., 2022.

[34] N. Monney, L. Kurz, S. Gillioz, and C. Nellen, "I.C. engine conversion for hydrogen combustion and near zero NOx emissions," May 2023. DOI: 10.20944/preprints202305.0834.v1.

[35] D. Mumford, D. Goudie, and J. Saunders, "Potential and challenges of HPDI," in *SAE Technical Paper Series*, ser. AVL-1CPC17, SAE International, May 2017. DOI: 10.4271/2017-01-1928.

[36] T. Miller, "Design, build, and analysis of a compressed natural gas direct injection compression ignition single cylinder research engine," Ph.D. dissertation, Michigan Technological University. DOI: 10.37099/mtu.dc.etdr/1108.

[37] S. Gleis, S. Frankl, M. Prager, and G. Wachtmeister, "Optical analysis of the combustion of potential future e-fuels with a high pressure dual fuel injection system," Jun. 2020.

[38] Y. Suzuki, T. Tsujimura, and T. Mita, "The performance of multi-cylinder hydrogen / diesel dual fuel engine," *SAE International Journal of Engines*, vol. 8, no. 5, pp. 2240–2252, Sep. 2015, ISSN: 1946-3944. DOI: 10.4271/2015-24-2458.

[39] P. Dimitriou, T. Tsujimura, and Y. Suzuki, "Low-load hydrogen-diesel dual-fuel engine operation – a combustion efficiency improvement approach," *International Journal of Hydrogen Energy*, vol. 44, no. 31, pp. 17 048–17 060, Jun. 2019, ISSN: 0360-3199. DOI: 10.1016/j.ijhydene.2019.04.203.

[40] E. Tomita, "Hydrogen combustion and exhaust emissions ignited with diesel oil in a dual fuel engine," *SAE Technical Paper Series*, 2001.

[41] J. McNally, "Hydrogen-diesel dual fuel combustion characterization for an internal combustion engine," M.S. thesis, University of Alberta, 2023.

[42] M. Talibi, P. Hellier, R. Morgan, C. Lenartowicz, and N. Ladommatos, "Hydrogen-diesel fuel co-combustion strategies in light duty and heavy duty CI engines," *International Journal of Hydrogen Energy*, vol. 43, no. 18, pp. 9046–9058, May 2018, ISSN: 0360-3199. DOI: 10.1016/j.ijhydene.2018.03.176.

[43] J. E. Dec, "A conceptual model of DI diesel combustion based on laser-sheet imaging," in *SAE Technical Paper Series*, ser. ANNUAL, SAE International, Feb. 1997. DOI: 10.4271/970873.

[44] R. Stone, *Introduction to Internal Combustion Engines*. The MacMillan Press Ltd, 1992.

[45] C. Liew *et al.*, "An experimental investigation of the combustion process of a heavy-duty diesel engine enriched with H2," *International Journal of Hydrogen Energy*, vol. 35, no. 20, pp. 11 357–11 365, Oct. 2010, ISSN: 0360-3199. DOI: 10.1016/j.ijhydene.2010.06.023.

[46] R. Farzam, M. Guan, R. Gmoser, P. Steiche, P. Kirchen, and G. McTaggart-Cowan, "Combustion characterization and heat release rate modeling of a heavy-duty hydrogen-diesel dual-fuel engine," in *SAE Technical Paper Series*, ser. ANNUAL, vol. 1, SAE International, Apr. 2025. DOI: 10.4271/2025-01-8418.

[47] A. Jamrozik, K. Grab-Rogaliński, and W. Tutak, "Hydrogen effects on combustion stability, performance and emission of diesel engine," *International Journal of Hydrogen Energy*, vol. 45, no. 38, pp. 19 936–19 947, Jul. 2020, ISSN: 0360-3199. DOI: 10.1016/j.ijhydene.2020.05.049.

[48] L. Xu, H. Dong, S. Liu, L. Shen, and Y. Bi, "Study on the combustion mechanism of diesel/hydrogen dual fuel and the influence of pilot injection and main injection," *Processes*, vol. 11, no. 7, p. 2122, Jul. 2023, ISSN: 2227-9717. DOI: 10.3390/pr11072122.

[49] A. Maghbouli, W. Yang, H. An, S. Shafee, J. Li, and S. Mohammadi, "Modeling knocking combustion in hydrogen assisted compression ignition diesel engines," *Energy*, vol. 76, pp. 768–779, Nov. 2014, ISSN: 0360-5442. DOI: 10.1016/j.energy.2014.08.074.

[50] N. Kawahara and E. Tomita, "Visualization of auto-ignition and pressure wave during knocking in a hydrogen spark-ignition engine," *International Journal of Hydrogen Energy*, vol. 34, no. 7, pp. 3156–3163, Apr. 2009, ISSN: 0360-3199. DOI: 10.1016/j.ijhydene.2009.01.091.

[51] M. U. Manzoor, M. Yosri, M. Talei, F. Poursadegh, Y. Yang, and M. Brear, "Normal and knocking combustion of hydrogen: A numerical study," *Fuel*, vol. 344, p. 128 093, Jul. 2023, ISSN: 0016-2361. DOI: 10.1016/j.fuel.2023.128093.

[52] D. Lata and A. Misra, "Analysis of ignition delay period of a dual fuel diesel engine with hydrogen and LPG as secondary fuels," *International Journal of Hydrogen Energy*, vol. 36, no. 5, pp. 3746–3756, Mar. 2011, ISSN: 0360-3199. DOI: 10.1016/j.ijhydene.2010.12.075.

[53] S. Verma, L. Das, S. Bhatti, and S. Kaushik, "A comparative exergetic performance and emission analysis of pilot diesel dual-fuel engine with biogas, CNG and hydrogen as main fuels," *Energy Conversion and Management*, vol. 151, pp. 764–777, Nov. 2017, ISSN: 0196-8904. DOI: 10.1016/j.enconman.2017.09.035.

[54] S. Verma, L. Das, S. Kaushik, and S. Tyagi, "An experimental investigation of exergetic performance and emission characteristics of hydrogen supplemented biogas-diesel dual fuel engine," *International Journal of Hydrogen Energy*, vol. 43, no. 4, pp. 2452–2468, Jan. 2018, ISSN: 0360-3199. DOI: 10.1016/j.ijhydene.2017.12.032.

[55] A. Aldawood, S. Mosbach, and M. Kraft, "HCCI combustion phasing transient control by hydrogen-rich gas: Investigation using a fast detailed-chemistry full-cycle model," in *SAE Technical Paper Series*, ser. ANNUAL, SAE International, Apr. 2009. DOI: 10.4271/2009-01-1134.

[56] T Shudo and H Yamada, "Hydrogen as an ignition-controlling agent for HCCI combustion engine by suppressing the low-temperature oxidation," *International Journal of Hydrogen Energy*, vol. 32, no. 14, pp. 3066–3072, Sep. 2007, ISSN: 0360-3199. DOI: 10.1016/j.ijhydene.2006.12.002.

[57] H.-W. Wu and Z.-Y. Wu, "Investigation on combustion characteristics and emissions of diesel/hydrogen mixtures by using energy-share method in a diesel engine," *Applied Thermal Engineering*, vol. 42, pp. 154–162, Sep. 2012, ISSN: 1359-4311. DOI: 10.1016/j.applthermaleng.2012.03.004.

[58] S. Verhelst *et al.*, "Setting a best practice for determining the EGR rate in hydrogen internal combustion engines," *International Journal of Hydrogen Energy*, vol. 38, no. 5, pp. 2490–2503, Feb. 2013, ISSN: 0360-3199. DOI: 10.1016/j.ijhydene.2012.11.138.

[59] Pat. 6 212 467, 2001.

[60] Y. Chen *et al.*, "An investigation on the H2O, unburned H2 and NO emission characteristics from a direct injection hydrogen engine," *International Journal of Hydrogen Energy*, vol. 81, pp. 1181–1191, Sep. 2024, ISSN: 0360-3199. DOI: 10.1016/j.ijhydene.2024.07.368.

[61] T. Gatts *et al.*, "An experimental investigation of H2 emissions of a 2004 heavy-duty diesel engine supplemented with H2," *International Journal of Hydrogen Energy*, vol. 35, no. 20, pp. 11 349–11 356, Oct. 2010, ISSN: 0360-3199. DOI: 10.1016/j.ijhydene.2010.06.056.

[62] T. Gatts, S. Liu, C. Liew, B. Ralston, C. Bell, and H. Li, "An experimental investigation of incomplete combustion of gaseous fuels of a heavy-duty diesel engine supplemented with hydrogen and natural gas," *International Journal of Hydrogen Energy*, vol. 37, no. 9, pp. 7848–7859, May 2012, ISSN: 0360-3199. DOI: 10.1016/j.ijhydene.2012.01.088.

[63] T. Izawa, S. Kim, M. Matsumoto, S. Hasegawa, and M. Kawase, "Development of an inferential control system of hydrogen concentration of exhaust gas in fuel cell systems," in *34th European Symposium on Computer Aided Process Engineering / 15th International Symposium on Process Systems Engineering.* Elsevier, 2024, pp. 1813–1818, ISBN: 9780443288241. DOI: 10.1016/b978-0-443-28824-1.50303-3.

[64] *Global technical regulation on hydrogen and fuel cell vehicles*, United Nations, 2013.

[65] Y. Naganuma, K. Manabe, H. Imanishi, and Y. Nonobe, "Development of system control for rapid warm-up operation of fuel cell," *SAE International Journal of Alternative Powertrains*, vol. 1, no. 1, pp. 365–373, Apr. 2012, ISSN: 2167-4205. DOI: 10.4271/2012-01-1230.

[66] D. Hao, X. Wang, Y. Zhang, R. Wang, G. Chen, and J. Li, "Experimental study on hydrogen leakage and emission of fuel cell vehicles in confined spaces," *Automotive Innovation*, vol. 3, no. 2, pp. 111–122, May 2020, ISSN: 2522-8765. DOI: 10.1007/s42154-020-00096-z.

[67] A. Talukdar *et al.*, "A review on solid oxide fuel cell technology: An efficient energy conversion system," *International Journal of Energy Research*, vol. 2024, M. Ahmed, Ed., pp. 1–20, May 2024, ISSN: 0363-907X. DOI: 10.1155/2024/6443247.

[68] P. Kuchonthara, S. Bhattacharya, and A. Tsutsumi, "Combinations of solid oxide fuel cell and several enhanced gas turbine cycles," *Journal of Power Sources*, vol. 124, no. 1, pp. 65–75, Oct. 2003, ISSN: 0378-7753. DOI: 10.1016/s0378-7753(03)00740-7.

[69] P. Liu *et al.*, "Analysis and design for hydrogen-fueled cascade solid oxide fuel cell system," *Energy Conversion and Management*, vol. 313, p. 118 433, Aug. 2024, ISSN: 0196-8904. DOI: 10.1016/j.enconman.2024.118433.

[70] R. G. Derwent, W. J. Collins, C. E. Johnson, and D. S. Stevenson, "Transient behaviour of tropospheric ozone precursors in a global 3-D CTM and their indirect greenhouse effects," *Climatic Change*, vol. 49, no. 4, pp. 463–487, 2001, ISSN: 0165-0009. DOI: 10.1023/a:1010648913655.

[71] M. Sand *et al.*, "A multi-model assessment of the global warming potential of hydrogen," *Communications Earth & Environment*, vol. 4, no. 1, Jun. 2023, ISSN: 2662-4435. DOI: 10.1038/s43247-023-00857-8.

[72] Y. M. Adzavon *et al.*, "Long-term and daily use of molecular hydrogen induces reprogramming of liver metabolism in rats by modulating NADP/NADPH redox pathways," *Scientific Reports*, vol. 12, no. 1, Mar. 2022, ISSN: 2045-2322. DOI: 10.1038/s41598-022-07710-6.

[73] S. Davis and R. Boundy, *Transportation Energy Data Book (Edition 40)*. May 2022. DOI: 10.2172/1878695.

[74] M. Al-Ghouti, Y. Al-Degs, and F. Mustafa, "Determination of hydrogen content, gross heat of combustion, and net heat of combustion of diesel fuel using FTIR spectroscopy and multivariate calibration," *Fuel*, vol. 89, no. 1, pp. 193–201, Jan. 2010, ISSN: 0016-2361. DOI: 10.1016/j.fuel.2009.08.044.

[75] A. Abu-Jrai, A. Tsolakis, and A. Megaritis, "The influence of H2 and CO on diesel engine combustion characteristics, exhaust gas emissions, and after treatment selective catalytic NOx reduction," *International Journal of Hydrogen Energy*, vol. 32, no. 15, pp. 3565–3571, Oct. 2007, ISSN: 0360-3199. DOI: 10.1016/j.ijhydene.2007.02.014.

[76] P. G. Savva and C. N. Costa, "Hydrogen lean-denoxas an alternative to the ammonia and hydrocarbon selective catalytic reduction (SCR)," *Catalysis Reviews*, vol. 53, no. 2, pp. 91–151, Apr. 2011, ISSN: 1520-5703. DOI: 10.1080/01614940.2011.557964.

[77] Z. Liu, J. Li, and S. I. Woo, "Recent advances in the selective catalytic reduction of NOx by hydrogen in the presence of oxygen," *Energy & Environmental Science*, vol. 5, no. 10, p. 8799, 2012, ISSN: 1754-5706. DOI: 10.1039/c2ee22190j.

[78] R. Morgan, P. Atkins, A. Atkins, C. Lenartowicz, and M. Heikal, "Effect of hydrogen fumigation in a dual fueled heavy duty engine," in *SAE Technical Paper Series*, ser. ICE2015, SAE International, Sep. 2015. DOI: 10.4271/2015-24-2457.

[79] E.-A. Tingas, Ed., *Hydrogen for Future Thermal Engines*. Springer International Publishing, 2023, ISBN: 9783031284120. DOI: 10.1007/978-3-031-28412-0.

[80] E. Yakupov, V. Gubernov, and A. Polezhaev, "Formation of spiral structures in rich-hydrogen air flames at elevated pressures," *International Journal of Hydrogen Energy*, vol. 49, pp. 784–795, Jan. 2024, ISSN: 0360-3199. DOI: 10.1016/j.ijhydene.2023.09.081.

[81] F. Veiga-López, M. Kuznetsov, D. Martínez-Ruiz, E. Fernández-Tarrazo, J. Grune, and M. Sánchez-Sanz, "Unexpected propagation of ultra-lean hydrogen flames in narrow gaps," *Physical Review Letters*, vol. 124, no. 17, May 2020, ISSN: 1079-7114. DOI: 10.1103/physrevlett.124.174501.

[82] M. K. Vollmer *et al.*, "Molecular hydrogen (H2) combustion emissions and their isotope (D/H) signatures from domestic heaters, diesel vehicle engines, waste incinerator plants, and biomass burning," *Atmospheric Chemistry and Physics (ACP)*, Mar. 2012. DOI: 10.5194/acpd-12-6839-2012.

[83] S. Bond, R. Alvarez, M. Vollmer, M. Steinbacher, M. Weilenmann, and S. Reimann, "Molecular hydrogen (H2) emissions from gasoline and diesel vehicles," *Science of The Total Environment*, vol. 408, no. 17, pp. 3596–3606, Aug. 2010, ISSN: 0048-9697. DOI: 10.1016/j.scitotenv.2010.04.055.

[84] S. H. Chan, "An exhaust emissions based air–fuel ratio calculation for internal combustion engines," *Proceedings of the Institution of Mechanical Engineers, Part D: Journal of Automobile Engineering*, vol. 210, no. 3, pp. 273–280, Jul. 1996, ISSN: 2041-2991. DOI: 10.1243/pime_proc_1996_210_271_02.

[85] W. Watson, “On the thermal and combustion efficiency of a four-cylinder petrol motor,” in *Proceedings of the Institution of Automobile Engineers 1908*, 1908.

[86] B. A. D’Alleva and W. G. Lovell, “Relation of exhaust gas composition to air-fuel ratio,” in *SAE Technical Paper Series*, ser. GMDMEETING, SAE International, Jan. 1936. DOI: 10.4271/360106.

[87] L. Boon-Brett, J. Bousek, and P. Moretto, “Reliability of commercially available hydrogen sensors for detection of hydrogen at critical concentrations: Part ii – selected sensor test results,” *International Journal of Hydrogen Energy*, vol. 34, no. 1, pp. 562–571, Jan. 2009, ISSN: 0360-3199. DOI: 10.1016/j.ijhydene.2008.10.033.

[88] S. Shahpouri, D. Gordon, C. Hayduk, R. Rezaei, C. R. Koch, and M. Shahbakhti, “Hybrid emission and combustion modeling of hydrogen fueled engines,” *International Journal of Hydrogen Energy*, vol. 48, no. 62, pp. 24 037–24 053, 2023.

[89] J McNally, D Gordon, E Sperling, M Shahbakti, and C. Koch, “Performance and emission investigation of hydrogen diesel dual fuel combustion,” in *Proceedings of Combustion Institute – Canadian Section, Edmonton, AB*, 2023.

[90] N. Fonseca González, J. Casanova Kindelán, and J. M. López Martí;nez, “Methodology for instantaneous average exhaust gas mass flow rate measurement,” *Flow Measurement and Instrumentation*, vol. 49, pp. 52–62, Jun. 2016, ISSN: 0955-5986. DOI: 10.1016/j.flowmeasinst.2016.04.007.

[91] *Hana H2200 injector*, Hana EMS Co Ltd.

[92] J. H. Lienesch and M. K. Krage, “Using microwaves to phase cylinder pressure to crankshaft position,” in *SAE Technical Paper Series*, ser. ANNUAL, SAE International, Feb. 1979. DOI: 10.4271/790103.

[93] K. S. Kim and S. S. Kim, “Measurement of dynamic TDC in SI engines using microwave sensor, proximity probe and pressure transducers,” in *SAE Technical Paper Series*, ser. OH, SAE International, Sep. 1989. DOI: 10.4271/891823.

[94] P. Tunestål, “Model based TDC offset estimation from motored cylinder pressure data,” *IFAC Proceedings Volumes*, vol. 42, no. 26, pp. 241–247, 2009, ISSN: 1474-6670. DOI: 10.3182/20091130-3-fr-4008.00032.

[95] R. B. K. David R. Lancaster and J. H. Lienesch, “Measurement and analysis of engine pressure data,” *SAE Transactions , 1975, Vol. 84, Section 1: 750002–750223 (1975), pp. 155-172*, 1975.

[96] E. Pipitone, A. Beccari, and S. Beccari, “The experimental validation of a new thermodynamic method for TDC determination,” in *SAE Technical Paper Series*, ser. ICE2007, SAE International, Sep. 2007. DOI: 10.4271/2007-24-0052.

[97] G. F. Hohenberg, "Advanced approaches for heat transfer calculations," in *SAE Technical Paper Series*, ser. OH, SAE International, Feb. 1979. DOI: 10.4271/790825.

[98] E. Pipitone and A. Beccari, "Determination of TDC in internal combustion engines by a newly developed thermodynamic approach," *Applied Thermal Engineering*, vol. 30, no. 14–15, pp. 1914–1926, Oct. 2010, ISSN: 1359-4311. DOI: 10.1016/j.applthermaleng.2010.04.012.

[99] V. Rocco, "Dynamic T.D.C. and thermodynamic loss angle measurement in a D. I. diesel engine," in *SAE Technical Paper Series*, ser. OH, SAE International, Sep. 1985. DOI: 10.4271/851546.

[100] Z. Bulatovic, D. Knezevic, and M. Milic, "Practical research of the angle of thermodynamic losses when indicating pressure in the cylinder diesel engine," *Scientific Technical Review*, vol. 65, no. 4, pp. 46–54, 2015, ISSN: 1820-0206. DOI: 10.5937/str1504046b.

[101] M. J. da Silva, A. de Oliveira, and J. R. Sodré, "Analysis of processing methods for combustion pressure measurement in a diesel engine," *Journal of the Brazilian Society of Mechanical Sciences and Engineering*, vol. 41, no. 7, Jun. 2019, ISSN: 1806-3691. DOI: 10.1007/s40430-019-1785-9.

[102] J. J. Carroll, J. D. Slupsky, and A. E. Mather, "The solubility of carbon dioxide in water at low pressure," *Journal of Physical and Chemical Reference Data*, vol. 20, no. 6, pp. 1201–1209, Nov. 1991, ISSN: 1529-7845. DOI: 10.1063/1.555900.

[103] E. Avallone, *Mark's Standard Handbook for Mechanical Engineers*, B. Sun and D. Fogarty, Eds. McGraw-Hill Inc, 1979.

[104] J. Demuynck, M. De Paepe, H. Huisseune, R. Sierens, J. Vancoillie, and S. Verhelst, "On the applicability of empirical heat transfer models for hydrogen combustion engines," *International Journal of Hydrogen Energy*, vol. 36, no. 1, pp. 975–984, Jan. 2011, ISSN: 0360-3199. DOI: 10.1016/j.ijhydene.2010.10.059.

[105] K. M. K. Kenneth S Kim Michael T Szedlmayer and C.-B. M. Kweon, "Optimization of in-cylinder pressure filter for engine research," *United States Army Research Laboratory*, 2017.

[106] J. I. Ghojel, "Review of the development and applications of the Wiebe function: A tribute to the contribution of Ivan Wiebe to engine research," *International Journal of Engine Research*, vol. 11, no. 4, pp. 297–312, Jun. 2010, ISSN: 2041-3149. DOI: 10.1243/14680874jer06510.

[107] E. Sperling, D. Gordon, and C. R. Koch, "Low-cost commercial hydrogen sensor for measuring unburned hydrogen in engine exhaust," in *Proceedings of the Canadian Society for Mechanical Engineering International Congress, Montreal, QC*, 2025.

[108] T. Hübert, L. Boon-Brett, G. Black, and U. Banach, "Hydrogen sensors – a review," *Sensors and Actuators B: Chemical*, vol. 157, no. 2, pp. 329–352, Oct. 2011, ISSN: 0925-4005. DOI: 10.1016/j.snb.2011.04.070.

[109] SGX, *Hydrogen sensor datasheet EC4 series*, Oct. 2009.

[110] SGX, *Hydrogen sensor datasheet PS4 series*, Feb. 2022.

[111] N. Moussa *et al.*, "Hydrogen sensing technologies for the safe and reliable decarbonization of electric power: A review," *Energies*, vol. 17, no. 18, p. 4532, Sep. 2024, ISSN: 1996-1073. DOI: 10.3390/en17184532.

[112] P. Soundarrajan and F. Schweighardt, "Hydrogen sensing and detection," in *Hydrogen Fuel*. CRC Press, Jul. 2008, pp. 495–534, ISBN: 9781420045772. DOI: 10.1201/9781420045772.ch15.

[113] M. Choudhary *et al.*, "Emerging nanomaterials for hydrogen sensing: Mechanisms and prospects," *International Journal of Hydrogen Energy*, vol. 77, pp. 557–574, Aug. 2024, ISSN: 0360-3199. DOI: 10.1016/j.ijhydene.2024.06.149.

[114] M. Yang and J. Dai, "Fiber optic hydrogen sensors: A review," *Photonic Sensors*, vol. 4, no. 4, pp. 300–324, Oct. 2014, ISSN: 2190-7439. DOI: 10.1007/s13320-014-0215-y.

[115] S. Chatterjee *et al.*, "Hydrogen gas sensing using aluminum doped ZnO metasurfaces," *Nanoscale Advances*, vol. 2, no. 8, pp. 3452–3459, 2020, ISSN: 2516-0230. DOI: 10.1039/d0na00289e.

[116] C. Shen *et al.*, "Review of the status and prospects of fiber optic hydrogen sensing technology," *Chemosensors*, vol. 11, no. 9, p. 473, Aug. 2023, ISSN: 2227-9040. DOI: 10.3390/chemosensors11090473.

[117] M. Lischka and A. Groß, *Recent Developments in Vacuum Science and Technology*, J. Dabrowski, Ed. Research Signpost, 2003.

[118] I. Lundström, S. Shivaraman, C. Svensson, and L. Lundkvist, "A hydrogen—sensitive MOS field—effect transistor," *Applied Physics Letters*, vol. 26, no. 2, pp. 55–57, Jan. 1975, ISSN: 1077-3118. DOI: 10.1063/1.88053.

[119] L. F. Aval, S. Elahi, E. Darabi, and S. Sebt, "Comparison of the MOS capacitor hydrogen sensors with different SiO2 film thicknesses and a Ni-gate film in a 4% hydrogen–nitrogen mixture," *Sensors and Actuators B: Chemical*, vol. 216, pp. 367–373, Sep. 2015, ISSN: 0925-4005. DOI: 10.1016/j.snb.2015.04.039.

[120] P. Firek *et al.*, "The preparation and properties of a hydrogen-sensing field-effect transistor with a gate of nanocomposite C-Pd film," *Energies*, vol. 17, no. 13, p. 3261, Jul. 2024, ISSN: 1996-1073. DOI: 10.3390/en17133261.

[121] K. Park and M. P. Kim, "Advancements in flexible and stretchable electronics for resistive hydrogen sensing: A comprehensive review," *Sensors*, vol. 24, no. 20, p. 6637, Oct. 2024, ISSN: 1424-8220. DOI: 10.3390/s24206637.

[122] C. A. Grimes *et al.*, "A sentinel sensor network for hydrogen sensing," *Sensors*, vol. 3, no. 3, pp. 69–82, Feb. 2003, ISSN: 1424-8220. DOI: 10.3390/s30300069.

[123] A. Katsuki and K. Fukui, "H2 selective gas sensor based on SnO2," *Sensors and Actuators B: Chemical*, vol. 52, no. 1–2, pp. 30–37, Sep. 1998, ISSN: 0925-4005. DOI: 10.1016/s0925-4005(98)00252-4.

[124] J. Vyas, V. Katti, S. Gupta, and J. Yakhmi, "A non-invasive ultrasonic gas sensor for binary gas mixtures," *Sensors and Actuators B: Chemical*, vol. 115, no. 1, pp. 28–32, May 2006, ISSN: 0925-4005. DOI: 10.1016/j.snb.2005.08.016.

[125] W. E. Katja Dettmer-Wilde, Ed., *Practical Gas Chromatography: A Comprehensive Reference*. Springer Berlin Heidelberg, 2014, ISBN: 9783642546402. DOI: 10.1007/978-3-642-54640-2.

[126] J.-B. Sanchez, A. Schmitt, F. Berger, and C. Mavon, "Silicon-micromachined gas chromatographic columns for the development of portable detection device," *Journal of Sensors*, vol. 2010, pp. 1–8, 2010, ISSN: 1687-7268. DOI: 10.1155/2010/409687.

[127] R. Ekman, Ed., *Mass Spectrometry Instrumentation, Interpretation, and Applications*. John Wiley and Sons, 2009.

[128] A. Malcolm, S. Wright, R. R. A. Syms, N. Dash, M.-A. Schwab, and A. Finlay, "Miniature mass spectrometer systems based on a microengineered quadrupole filter," *Analytical Chemistry*, vol. 82, no. 5, pp. 1751–1758, Jan. 2010, ISSN: 1520-6882. DOI: 10.1021/ac902349k.

[129] K. Peruski, B. Vestal, M. Vick, C. Cobble, K. Johnson, and J. McFarlane, *On-line Measurement of Hydrogen Gas using Raman Spectroscopy for Process Gas Systems*. Oak Ridge National Lab, Jul. 2023. DOI: 10.2172/1988350.

[130] J. R. Stetter and J. Li, "Amperometric gas sensors: A review," *Chemical Reviews*, vol. 108, no. 2, pp. 352–366, Jan. 2008, ISSN: 1520-6890. DOI: 10.1021/cr0681039.

[131] C. K. M. Aliramezani K. Ebrahimi and R. E. Hayes, "NOX sensor ammonia cross sensitivity analysis using a simplified physics based model," in *Proceedings of Combustion Institute – Canadian Section*, 2016.

[132] M. Aliramezani, C. R. Koch, and R. Patrick, "A variable-potential amperometric hydrocarbon sensor," *IEEE Sensors Journal*, vol. 19, no. 24, pp. 12 003–12 010, Dec. 2019, ISSN: 2379-9153. DOI: 10.1109/jsen.2019.2938920.

[133] M. Aliramezani, "Production engine emission sensor modeling for in-use measurement and on-board diagnostics," Ph.D. dissertation, University of Alberta, 2019.

[134] M Sakthivel, "A portable limiting current solid-state electrochemical diffusion hole type hydrogen sensor device for biomass fuel reactors: Engineering aspect," *International Journal of Hydrogen Energy*, vol. 33, no. 2, pp. 905–911, Jan. 2008, ISSN: 0360-3199. DOI: 10.1016/j.ijhydene.2007.10.048.

[135] W. J. B. Yente Chao Sheng Yao and J. R. Stetter, “Amperometric sensor for selective and stable hydrogen measurement,” *Sensors and Actuators B: Chemical*, vol. 106, no. 2, pp. 784–790, May 2005, ISSN: 0925-4005. DOI: 10.1016/j.snb.2004.09.042.

[136] V. Nikolova, I. Nikolov, P. Andreev, V. Najdenov, and T. Vitanov, “Tungsten carbide-based electrochemical sensors for hydrogen determination in gas mixtures,” *Journal of Applied Electrochemistry*, vol. 30, no. 6, pp. 705–710, 2000, ISSN: 0021-891X. DOI: 10.1023/a:1003813210270.

[137] H. Zhang *et al.*, “1ppm-detectable hydrogen gas sensors by using highly sensitive p+/n+ single-crystalline silicon thermopiles,” *Microsystems & Nanoengineering*, vol. 9, no. 1, Mar. 2023, ISSN: 2055-7434. DOI: 10.1038/s41378-023-00506-2.

[138] V. Katti, A. Debnath, S. Gadkari, S. Gupta, and V. Sahni, “Passivated thick film catalytic type H2 sensor operating at low temperature,” *Sensors and Actuators B: Chemical*, vol. 84, no. 2–3, pp. 219–225, May 2002, ISSN: 0925-4005. DOI: 10.1016/s0925-4005(02)00028-x.

[139] RKI-Instruments, *RKI instruments FSD 753 - FHD 752 datasheet.*

[140] R. Bellavance, “Private communication,” 2023.

[141] *GE50A elastomer sealed digital mass flow controller.*

[142] G. K. Lilik, H. Zhang, J. M. Herreros, D. C. Haworth, and A. L. Boehman, “Hydrogen assisted diesel combustion,” *International Journal of Hydrogen Energy*, vol. 35, no. 9, pp. 4382–4398, May 2010, ISSN: 0360-3199. DOI: 10.1016/j.ijhydene.2010.01.105.

[143] P. Dimitriou, M. Kumar, T. Tsujimura, and Y. Suzuki, “Combustion and emission characteristics of a hydrogen-diesel dual-fuel engine,” *International Journal of Hydrogen Energy*, vol. 43, no. 29, pp. 13 605–13 617, Jul. 2018, ISSN: 0360-3199. DOI: 10.1016/j.ijhydene.2018.05.062.

[144] M. Instruments, *Engines vehicles recipes R4 information*, 2016.

[145] E. Sperling, H. Mehnatkesh, J. Kheyrollahi, D. Gordon, and C. R. Koch, “Hydrogen slip measurement in a hydrogen diesel dual-fuel engine,” in *Proceedings of Combustion Institute – Canadian Section, Kingston, ON*, 2024.

[146] E. Sperling, D. Gordon, and C. R. Koch, “Heat release characteristics of a hydrogen-diesel dual fuel engine for varied hydrogen energy and pilot diesel injection timing,” in *Proceedings of Combustion Institute – Canadian Section, Calgary, AB*, 2025.

Appendix A: Combustion Metrics

A.1 Combustion Metrics for IMEP=3 bar and Varied HES

Table A.1: 3 bar Combustion Metrics (SOI=-04)

HES (%)	H2 Exh %	CO2 Total Equivalent g/kWh	CA10 CAD	CA50 CAD	CA90 CAD	Ignition Delay CAD	Burn Duration CAD	η_{th} %
82.2	0.497	193	8.2	19.5	34.7	12.2	26.5	35.2
82.3	0.496	192	8.2	19.9	34.5	12.2	26.3	35.1
82.2	0.481	191	8.2	19.7	34.3	12.2	26.1	35.0
72.9	0.765	292	7.6	14.9	28.7	11.6	21.1	36.0
70.2	0.701	299	7.5	13.6	26.7	11.5	19.2	36.2
69.3	0.663	298	7.4	13.2	26.1	11.4	18.7	36.5
57.4	1.126	475	7.6	10.6	23.2	11.6	15.6	34.1
58.9	1.207	485	7.7	10.8	23.5	11.7	15.8	33.3
55.2	0.825	417	7.4	10.2	21.6	11.4	14.2	36.5
50.0	1.230	532	7.7	10.1	20.8	11.7	13.1	34.9
50.9	1.376	565	7.7	10.2	20.1	11.7	12.4	33.7
48.7	1.048	491	7.4	9.8	19.7	11.4	12.3	36.5

Table A.2: 3 bar Combustion Metrics (SOI=-14)

HES (%)	H2 Exh %	CO2 Total Equivalent g/kWh	CA10 CAD	CA50 CAD	CA90 CAD	Ignition Delay CAD	Burn Duration CAD	η_{th} %
82.0	0.649	202	-3.1	5.0	15.5	10.9	18.6	38.6
83.6	0.632	189	-2.5	6.5	16.7	11.5	19.2	38.4
81.9	0.642	201	-3.0	5.0	14.9	11.0	17.9	38.2
71.1	0.700	284	-3.9	0.9	10.9	10.1	14.8	38.5
68.0	0.603	282	-4.3	-0.9	7.5	9.7	11.8	39.3
71.0	0.646	275	-3.9	0.4	9.9	10.1	13.8	38.3
53.9	0.659	404	-4.2	-1.5	8.9	9.8	13.1	38.0
57.4	0.796	420	-4.1	-1.2	10.0	9.9	14.1	36.4
50.9	0.566	405	-4.3	-1.9	7.3	9.7	11.6	38.3
44.5	0.630	466	-4.2	-1.8	8.6	9.8	12.8	37.9
45.8	0.661	465	-4.1	-1.8	8.6	9.9	12.7	37.6
42.0	0.478	452	-4.3	-2.1	6.7	9.7	11.0	38.6

Table A.3: 3 bar Combustion Metrics (SOI=-24)

HES (%)	H_2 Exh %	CO_2 Total Equivalent g/kWh	CA10 CAD	CA50 CAD	CA90 CAD	Ignition Delay CAD	Burn Duration CAD	η_{th} %
83.4	0.577	180	-2.8	7.8	19.5	21.2	22.3	39.8
84.2	0.596	178	-2.2	8.9	21.7	21.8	23.9	39.1
83.1	0.574	182	-2.3	7.6	19.0	21.7	21.3	39.0
71.9	0.642	266	-7.1	-0.6	7.8	16.9	14.9	40.3
72.9	0.644	255	-6.4	-0.3	7.9	17.6	14.3	40.6
69.7	0.652	280	-7.1	-1.6	6.2	16.9	13.3	40.1
53.0	0.595	385	-9.3	-5.4	1.2	14.7	10.5	40.3
51.4	0.604	392	-9.1	-5.8	-0.6	14.9	8.5	40.3
49.7	0.586	409	-9.5	-6.1	-1.2	14.5	8.3	39.3
43.8	0.532	447	-10.2	-6.7	-2.1	13.8	8.1	39.1
40.3	0.521	470	-10.1	-7.4	-4.4	13.9	5.7	38.5
41.3	0.530	466	-10.1	-7.2	-3.9	13.9	6.2	38.4

Table A.4: 3 bar Combustion Metrics (SOI=-34)

HES (%)	H_2 Exh %	CO_2 Total Equivalent g/kWh	CA10 CAD	CA50 CAD	CA90 CAD	Ignition Delay CAD	Burn Duration CAD	η_{th} %
52.7	0.714	391	-5.6	0.8	7.5	28.4	13.1	41.5
48.9	0.619	385	-5.7	-0.7	4.9	28.3	10.6	42.8
48.0	0.596	387	-5.3	-0.6	4.7	28.7	10.0	42.7
46.2	0.608	412	-7.5	-1.6	4.4	26.5	11.9	42.3
42.8	0.550	415	-6.9	-2.6	2.0	27.1	8.9	42.9
43.5	0.553	414	-6.3	-1.9	3.0	27.7	9.3	42.5

A.2 Combustion Metrics for IMEP=4 and 6 bar and Varied HES

Table A.5: 4 bar Combustion Metrics (SOI=-04)

HES (%)	H2 Exh %	CO2 Total Equivalent g/kWh	CA10 CAD	CA50 CAD	CA90 CAD	Ignition Delay CAD	Burn Duration CAD	η_{th} %
82.7	0.263	153	8.6	17.4	28.5	12.6	19.9	35.9
83.9	0.234	142	8.9	18.1	30.0	12.9	21.1	35.9
83.4	0.231	144	8.6	17.6	29.1	12.6	20.5	36.1
84.1	0.248	143	9.0	18.4	30.4	13.0	21.4	35.4
84.8	0.234	137	9.1	18.7	30.9	13.1	21.8	35.4
84.3	0.245	142	9.0	18.4	30.4	13.0	21.4	35.5
81.8	0.263	160	8.4	17.3	28.6	12.4	20.2	36.0
81.2	0.278	166	8.3	17.0	28.4	12.3	20.1	35.8
74.2	0.359	221	7.7	14.1	24.3	11.7	16.6	36.7
73.9	0.342	223	7.7	14.2	24.5	11.7	16.8	36.4
73.8	0.354	225	7.7	14.2	24.4	11.7	16.7	36.5
60.8	0.410	322	7.5	11.2	21.4	11.5	13.9	36.8
61.1	0.433	321	7.4	11.1	21.4	11.4	14.0	36.9
60.9	0.428	321	7.5	11.2	21.5	11.5	14.0	37.0
59.4	0.412	331	7.5	11.0	21.2	11.5	13.7	36.9
58.7	0.407	334	7.4	10.8	20.9	11.4	13.5	37.1
59.2	0.417	331	7.5	11.0	21.2	11.5	13.7	37.1
55.0	0.438	364	7.5	10.5	20.9	11.5	13.4	37.0
54.3	0.433	368	7.5	10.5	20.8	11.5	13.3	37.2
54.7	0.437	365	7.5	10.5	20.9	11.5	13.4	37.2

Table A.6: 4 bar Combustion Metrics (SOI=-14)

HES (%)	H2 Exh %	CO2 Total Equivalent g/kWh	CA10 CAD	CA50 CAD	CA90 CAD	Ignition Delay CAD	Burn Duration CAD	η_{th} %
84.1	0.331	142	-2.9	3.0	9.4	11.1	12.3	38.0
84.3	0.340	142	-2.8	3.2	9.9	11.2	12.7	37.8
84.2	0.344	143	-2.9	3.1	9.2	11.1	12.1	38.0
86.1	0.336	128	-2.2	4.2	11.4	11.8	13.6	38.3
86.2	0.330	127	-2.1	4.3	11.6	11.9	13.7	38.1
85.7	0.319	128	-2.5	3.8	10.4	11.5	12.9	38.4
85.6	0.338	131	-2.3	4.1	11.7	11.7	14.0	38.4
85.9	0.353	132	-2.3	4.1	11.4	11.7	13.7	38.1
84.9	0.353	138	-2.6	3.5	10.1	11.4	12.7	38.3
82.7	0.348	153	-3.2	2.4	8.5	10.8	11.7	38.1
82.8	0.380	157	-3.2	2.3	8.3	10.8	11.5	37.8
80.7	0.348	168	-3.8	1.0	6.1	10.2	9.9	37.7
75.2	0.392	213	-3.9	0.3	5.4	10.1	9.3	37.5
75.8	0.424	213	-3.9	0.4	5.8	10.1	9.7	37.2
73.8	0.412	227	-4.1	-0.3	4.5	9.9	8.6	37.0

Table A.7: 4 bar Combustion Metrics (SOI=-24)

HES (%)	H2 Exh %	CO2 Total Equivalent g/kWh	CA10 CAD	CA50 CAD	CA90 CAD	Ignition Delay CAD	Burn Duration CAD	η_{th} %
86.1	0.273	120	0.3	8.3	17.0	24.3	16.7	39.2
86.8	0.260	115	1.3	10.3	20.8	25.3	19.5	38.9
86.7	0.268	116	1.5	10.1	20.5	25.5	19.0	38.8
87.3	0.244	110	2.2	11.1	22.0	26.2	19.8	38.5
87.7	0.244	108	2.6	11.8	23.4	26.6	20.8	38.5
87.8	0.246	108	3.0	12.5	24.7	27.0	21.7	38.2
86.8	0.251	115	1.9	10.8	21.8	25.9	19.9	38.5
87.0	0.268	115	1.9	10.9	21.9	25.9	20.0	38.5
87.1	0.271	115	2.1	11.3	22.6	26.1	20.5	38.4
84.5	0.315	133	-1.5	5.6	12.1	22.5	13.6	39.5
85.1	0.318	131	-0.9	6.8	14.2	23.1	15.1	39.2
85.0	0.318	132	-0.7	6.8	14.2	23.3	14.9	39.1
76.6	0.371	197	-6.5	-2.0	2.2	17.5	8.7	38.3
76.5	0.363	195	-6.8	-2.5	1.6	17.2	8.4	38.6
76.4	0.376	197	-6.8	-2.4	1.7	17.2	8.5	38.6
63.4	0.439	304	-8.9	-6.3	-3.3	15.1	5.6	36.9
63.3	0.490	313	-9.3	-6.6	-3.5	14.7	5.8	36.6
61.2	0.478	326	-9.2	-6.7	-3.8	14.8	5.4	36.6

Table A.8: 4 bar Combustion Metrics (SOI=-34)

HES (%)	H2 Exh %	CO2 Total Equivalent g/kWh	CA10 CAD	CA50 CAD	CA90 CAD	Ignition Delay CAD	Burn Duration CAD	η_{th} %
60.1	0.626	320	-2.7	1.9	6.3	31.3	9.0	40.6
60.4	0.639	318	-3.1	1.5	5.9	30.9	9.0	40.7
59.9	0.642	322	-3.4	1.1	5.3	30.6	8.7	40.6
54.6	0.626	360	-4.5	-0.5	3.5	29.5	8.0	40.2
54.6	0.607	360	-4.7	-0.7	3.1	29.3	7.8	40.1
54.3	0.593	362	-4.9	-0.9	2.8	29.1	7.7	39.9
51.0	0.584	386	-6.4	-3.1	-0.1	27.6	6.3	39.3
51.3	0.605	385	-6.3	-2.9	0.2	27.7	6.5	39.5
51.4	0.608	385	-6.5	-3.1	0.0	27.5	6.5	39.5

Table A.9: 6 bar Combustion Metrics (SOI=-01)

HES (%)	H2 Exh %	CO2 Total Equivalent g/kWh	CA10 CAD	CA50 CAD	CA90 CAD	Ignition Delay CAD	Burn Duration CAD	η_{th} %
81.9	0.140	142	14.1	19.1	25.8	15.1	11.7	36.0
82.5	0.097	135	14.5	19.7	26.5	15.5	12.0	36.0
82.1	0.074	136	14.6	19.9	27.0	15.6	12.4	36.1
73.2	0.144	206	13.5	17.4	23.4	14.5	9.9	36.1
73.4	0.090	201	14.0	18.1	24.8	15.0	10.8	36.1
73.6	0.097	200	14.3	18.6	25.4	15.3	11.1	36.1
71.1	0.147	222	13.3	17.1	23.4	14.3	10.1	36.1
71.2	0.084	217	14.1	18.2	25.1	15.1	11.0	36.1
70.7	0.107	221	14.2	18.3	25.3	15.2	11.1	36.3
65.6	0.150	261	13.5	16.9	23.6	14.5	10.1	36.3
65.9	0.091	254	14.7	18.6	26.2	15.7	11.5	36.5
65.9	0.118	255	14.7	18.6	26.5	15.7	11.8	36.6
40.0	0.200	430	13.8	16.7	26.3	14.8	12.5	38.1
40.8	0.196	425	14.3	17.2	26.7	15.3	12.4	38.1
41.4	0.201	426	14.7	17.8	27.2	15.7	12.5	37.6

A.3 Combustion Metrics for Maximum HES Testing

Table A.10: Combustion Metrics, Minimum-Pilot Runs

IMEP (bar)	SOI (CAD)	HES (%)	H2exh (Vol%)	CA10 (CAD)	CA50 (CAD)	CA90 (CAD)	Ignition Delay (CAD)	Burn Duration (CAD)	η_{th}
2.082	-4.0	79.2	1.356	8.3	20.0	38.0	12.3	29.7	27.5
2.307	-4.0	78.8	1.151	8.3	20.1	37.4	12.3	29.1	29.4
1.885	-4.0	78.9	1.581	8.1	19.2	37.6	12.1	29.5	26.1
1.997	-9.0	79.1	1.536	1.0	9.4	23.7	10.0	22.7	29.2
2.424	-9.0	79.3	1.085	1.2	10.1	23.9	10.2	22.7	33.0
2.066	-9.0	79.2	1.513	1.0	9.6	23.9	10.0	22.9	30.3
1.986	-14.0	78.0	1.383	-3.4	4.9	16.7	10.6	20.1	30.8
2.253	-14.0	78.6	1.095	-3.1	5.6	16.9	10.9	20.0	33.1
2.196	-14.0	78.3	1.211	-3.3	5.3	16.8	10.7	20.1	33.2
1.939	-19.0	78.1	1.227	-6.3	3.8	15.1	12.7	21.4	31.1
2.219	-19.0	78.1	1.008	-5.4	4.3	15.4	13.6	20.8	33.8
2.239	-19.0	78.7	0.997	-5.4	4.4	15.2	13.6	20.6	34.3
1.993	-24.0	80.8	1.263	-4.9	7.5	21.0	19.1	25.9	31.1
2.325	-24.0	81.4	1.017	-2.8	9.2	23.3	21.2	26.1	33.9
2.332	-24.0	81.3	1.001	-3.6	8.3	21.9	20.4	25.5	34.5
2.070	-29.0	85.6	1.155	4.4	20.0	43.7	33.4	39.3	28.4
1.847	-29.0	87.3	1.383	6.6	24.6	52.6	35.6	46.0	25.6
2.078	-29.0	86.0	1.211	4.6	20.8	43.9	33.6	39.3	28.8
3.152	-4.0	80.2	0.495	8.5	19.4	33.9	12.5	25.4	35.0
3.094	-4.0	81.1	0.484	8.5	20.1	35.1	12.5	26.6	34.7

3.133	-4.0	80.7	0.496	8.6	19.8	34.5	12.6	25.9	35.2
3.098	-9.0	80.5	0.630	1.3	9.7	22.5	10.3	21.2	37.2
3.036	-9.0	81.7	0.652	1.4	10.3	22.9	10.4	21.5	37.0
3.064	-9.0	80.6	0.626	1.3	9.8	21.6	10.3	20.3	37.1
3.006	-14.0	80.4	0.641	-2.8	5.2	15.2	11.2	18.0	37.8
2.952	-14.0	81.8	0.674	-2.6	6.0	16.2	11.4	18.8	37.8
2.975	-14.0	81.3	0.651	-2.5	5.9	15.8	11.5	18.3	38.0
2.932	-19.0	80.9	0.618	-4.2	4.7	14.2	14.8	18.4	38.2
2.912	-19.0	81.7	0.638	-4.0	5.4	15.4	15.0	19.4	38.4
2.882	-19.0	81.6	0.615	-3.4	6.3	17.2	15.6	20.6	38.1
2.965	-24.0	82.9	0.641	-0.9	10.0	23.3	23.1	24.2	37.9
2.981	-24.0	82.9	0.596	-0.8	10.3	24.1	23.2	24.9	37.9
2.752	-24.0	84.0	0.694	1.9	14.2	30.5	25.9	28.6	35.8
3.979	-4.0	83.8	0.214	9.2	18.5	30.2	13.2	21.0	36.6
4.029	-4.0	84.2	0.196	9.2	18.3	29.9	13.2	20.7	36.9
4.017	-4.0	84.0	0.216	9.2	18.4	30.2	13.2	21.0	37.2
3.933	-9.0	84.2	0.308	1.7	9.1	20.7	10.7	19.0	38.6
3.986	-9.0	84.4	0.277	1.7	9.0	20.7	10.7	19.0	39.0
4.018	-9.0	83.9	0.300	1.6	8.9	20.2	10.6	18.6	39.3
3.900	-14.0	84.3	0.359	-2.5	4.1	13.4	11.5	15.9	39.1
3.943	-14.0	84.4	0.343	-2.5	4.0	12.8	11.5	15.3	39.3
3.979	-14.0	83.8	0.341	-2.6	3.8	12.1	11.4	14.7	39.7
3.919	-19.0	84.7	0.368	-3.9	2.8	10.0	15.1	13.9	39.9
3.933	-19.0	84.8	0.346	-4.0	2.5	9.5	15.0	13.5	39.9
3.953	-19.0	84.5	0.348	-4.0	2.5	9.3	15.0	13.3	40.4
3.972	-24.0	86.3	0.257	0.5	9.5	19.9	24.5	19.4	40.0
3.940	-24.0	86.2	0.263	0.4	9.3	19.5	24.4	19.1	39.9
3.947	-24.0	86.1	0.251	0.9	10.1	21.2	24.9	20.3	40.4
6.022	-4.0	88.9	0.124	7.1	10.9	16.9	11.1	9.8	38.7

6.006	-4.0	89.1	0.126	7.0	10.7	16.6	11.0	9.6	38.6
6.051	-4.0	88.8	0.090	7.0	10.8	16.5	11.0	9.5	39.3

Appendix B: Details of Test Points

B.1 Experimental Data for IMEP=3 bar and Varied HES

Test points for Section 4.5 are presented in the following Tables B.1, B.2, B.3, and B.4.

Table B.1: Experimental Data for Constant IMEP=3 and Varying HES Tests (SOI=-04)

DOI (ms)	Diesel (mg)	DOI H2 (ms)	HES (%)	IMEP (bar)	MPRR (bar/CAD)	η_{th} (%)	CO2exh (vol%)	H2int (vol%)	H2exh (vol%)	CO2eq Total(g/kWh)	H2 Slip Contribution (%)
0.170	4.1	3.050	82.2	3.108	1.489	35.2	0.595	7.394	0.497	193	30
0.170	4.1	3.050	82.3	3.140	1.482	35.1	0.599	7.518	0.496	192	30
0.170	4.2	3.050	82.2	3.156	1.481	35.0	0.608	7.548	0.481	191	29
0.250	6.0	2.630	72.9	3.061	3.094	36.0	0.872	6.316	0.765	292	31
0.250	6.9	2.630	70.2	3.219	3.958	36.2	1.002	6.353	0.701	299	27
0.250	7.2	2.630	69.3	3.271	4.391	36.5	1.038	6.334	0.663	298	25
0.280	9.4	2.450	57.4	2.883	6.213	34.1	1.354	4.951	1.126	475	30
0.280	9.1	2.450	58.9	2.830	5.775	33.3	1.316	5.104	1.207	485	32
0.280	10.7	2.450	55.2	3.340	8.006	36.5	1.548	5.159	0.825	417	22
0.350	11.2	2.350	50.0	2.983	8.104	34.9	1.605	4.354	1.230	532	29
0.350	10.9	2.350	50.9	2.848	7.519	33.7	1.564	4.384	1.376	565	31

0.350	12.1	2.350	48.7	3.278	9.258	36.5	1.737	4.456	1.048	491	24

Table B.2: Experimental Data for Constant IMEP=3 and Varying HES Tests (SOI=-14)

DOI (ms)	Diesel (mg)	DOI H2 (ms)	HES (%)	IMEP (bar)	MPRR (bar/CAD)	η_{th} (%)	CO2exh (vol%)	H2int (vol%)	H2exh (vol%)	CO2eq Total(g/kWh)	H2 Slip Contribution (%)
0.170	3.7	2.850	82.0	3.068	4.067	38.6	0.543	6.639	0.649	202	39
0.170	3.4	2.850	83.6	3.068	2.929	38.4	0.495	6.812	0.632	189	40
0.170	3.9	2.850	81.9	3.128	4.127	38.2	0.563	6.841	0.642	201	38
0.250	6.0	2.550	71.1	3.047	7.781	38.5	0.866	5.735	0.700	284	30
0.250	7.2	2.550	68.0	3.386	11.359	39.3	1.046	5.980	0.603	282	23
0.250	6.4	2.550	71.0	3.221	8.648	38.3	0.925	6.077	0.646	275	27
0.280	9.4	2.340	53.9	2.957	12.567	38.0	1.355	4.278	0.659	404	20
0.280	8.3	2.340	57.4	2.694	10.696	36.4	1.194	4.332	0.796	420	26
0.280	10.8	2.340	50.9	3.220	15.224	38.3	1.564	4.363	0.566	405	16
0.350	11.5	2.100	44.5	3.001	15.048	37.9	1.662	3.590	0.630	466	17
0.350	11.3	2.100	45.8	2.985	14.948	37.6	1.630	3.711	0.661	465	18
0.350	13.1	2.100	42.0	3.341	17.044	38.6	1.902	3.706	0.478	452	12

Table B.3: Experimental Data for Constant IMEP=3 and Varying HES Tests (SOI=-24)

DOI (ms)	Diesel (mg)	DOI H2 (ms)	HES (%)	IMEP (bar)	MPRR (bar/CAD)	η_{th} (%)	CO2exh (vol%)	H2int (vol%)	H2exh (vol%)	CO2eq Total(g/kWh)	H2 Slip Contribution (%)
0.170	3.4	2.850	83.4	3.087	1.518	39.8	0.480	6.594	0.577	180	38
0.170	3.3	2.850	84.2	3.085	1.480	39.1	0.461	6.767	0.596	178	40
0.170	3.6	2.850	83.1	3.158	1.518	39.0	0.513	6.856	0.574	182	37
0.250	5.3	2.500	71.9	2.914	3.690	40.3	0.764	5.297	0.642	266	30
0.250	5.3	2.500	72.9	3.053	3.760	40.6	0.767	5.588	0.644	255	30
0.250	6.0	2.500	69.7	3.023	4.400	40.1	0.860	5.357	0.652	280	28
0.280	8.9	2.250	53.0	2.908	8.077	40.3	1.276	3.902	0.595	385	20
0.280	9.8	2.250	51.4	3.097	9.785	40.3	1.410	4.030	0.604	392	18
0.280	10.3	2.250	49.7	3.088	10.373	39.3	1.494	3.978	0.586	409	17
0.350	11.2	1.950	43.8	2.981	11.693	39.1	1.616	3.406	0.532	447	15
0.350	13.3	1.950	40.3	3.285	15.402	38.5	1.930	3.500	0.521	470	12
0.350	12.8	1.950	41.3	3.206	14.734	38.4	1.856	3.517	0.530	466	13

Table B.4: Experimental Data for Constant IMEP=3 and Varying HES Tests (SOI=-34)

DOI (ms)	Diesel (mg)	DOI H2 (ms)	HES (%)	IMEP (bar)	MPRR (bar/CAD)	η_{th} (%)	CO2exh (vol%)	H2int (vol%)	H2exh (vol%)	CO2eq Total(g/kWh)	H2 Slip Contribution (%)
0.280	8.9	2.220	52.7	2.967	3.505	41.5	1.246	3.842	0.714	391	23
0.280	10.4	2.220	48.9	3.325	5.416	42.8	1.476	3.874	0.619	385	18
0.280	11.0	2.220	48.0	3.441	5.835	42.7	1.564	3.941	0.596	387	16
0.300	10.1	1.900	46.2	3.022	5.095	42.3	1.423	3.359	0.608	412	18
0.300	11.7	1.900	42.8	3.348	7.264	42.9	1.669	3.405	0.550	415	15
0.300	11.6	1.900	43.5	3.344	6.839	42.5	1.661	3.487	0.553	414	15

B.2 Experimental Data for IMEP=4 and 6 bar and Varied HES

Test points for Section 4.4, and as referenced in Subsection 4.4.1, are presented in the following Tables B.5, B.5, B.7, B.8, and B.9.

Table B.5: Experimental Data for Constant IMEP=4 and Varying HES Tests (SOI=-04)

DOI (ms)	Diesel (mg)	DOI H2 (ms)	HES (%)	IMEP (bar)	MPRR (bar/CAD)	η_{th} (%)	CO2exh (vol%)	H2int (vol%)	H2exh (vol%)	CO2eq Total(g/kWh)	H2 Slip Contribution (%)
0.170	4.9	3.600	82.7	3.896	1.630	35.9	0.714	9.150	0.263	153	16
0.170	4.5	3.600	83.9	3.828	1.491	35.9	0.652	9.135	0.234	142	16
0.170	4.7	3.600	83.4	3.881	1.592	36.1	0.678	9.134	0.231	144	15
0.210	4.5	3.600	84.1	3.792	1.454	35.4	0.647	9.181	0.248	143	17
0.210	4.2	3.600	84.8	3.750	1.435	35.4	0.613	9.146	0.234	137	17
0.210	4.4	3.600	84.3	3.780	1.443	35.5	0.636	9.152	0.245	142	17
0.230	5.1	3.500	81.8	3.806	1.774	36.0	0.732	8.814	0.263	160	16
0.230	5.2	3.500	81.2	3.802	1.842	35.8	0.757	8.795	0.278	166	16
0.250	7.1	3.200	74.2	3.836	4.055	36.7	1.023	7.917	0.359	221	16
0.250	7.2	3.200	73.9	3.818	3.878	36.4	1.038	7.895	0.342	223	15
0.250	7.2	3.200	73.8	3.827	3.956	36.5	1.041	7.892	0.354	225	15
0.280	10.8	2.750	60.8	3.872	8.278	36.8	1.562	6.533	0.410	322	12
0.280	10.7	2.750	61.1	3.864	8.098	36.9	1.541	6.514	0.433	321	13
0.280	10.7	2.750	60.9	3.882	7.859	37.0	1.552	6.511	0.428	321	13
0.300	11.2	2.700	59.4	3.907	8.397	36.9	1.625	6.412	0.412	331	12
0.300	11.6	2.700	58.7	3.963	8.608	37.1	1.670	6.393	0.407	334	11

0.300	11.3	2.700	59.2	3.932	8.461	37.1	1.634	6.391	0.417	331	12
0.350	12.4	2.500	55.0	3.896	9.354	37.0	1.790	5.906	0.438	364	11
0.350	12.7	2.500	54.3	3.935	9.590	37.2	1.832	5.859	0.433	368	11
0.350	12.5	2.500	54.7	3.920	9.296	37.2	1.808	5.879	0.437	365	11

Table B.6: Experimental Data for Constant IMEP=4 and Varying HES Tests (SOI=-14)

DOI (ms)	Diesel (mg)	DOI H2 (ms)	HES (%)	IMEP (bar)	MPRR (bar/CAD)	η_{th} (%)	CO2exh (vol%)	H2int (vol%)	H2exh (vol%)	CO2eq Total(g/kWh)	H2 Slip Contribution (%)
0.170	4.3	3.500	84.1	3.920	5.077	38.0	0.622	8.836	0.331	142	22
0.170	4.3	3.500	84.3	3.914	4.815	37.8	0.618	8.889	0.340	142	22
0.170	4.3	3.500	84.2	3.908	4.855	38.0	0.618	8.814	0.344	143	23
0.190	3.8	3.550	86.1	3.946	3.950	38.3	0.544	9.035	0.336	128	25
0.190	3.7	3.550	86.2	3.936	3.852	38.1	0.541	9.083	0.330	127	24
0.190	3.8	3.550	85.7	3.954	4.258	38.4	0.559	9.003	0.319	128	23
0.210	3.8	3.500	85.6	3.894	4.010	38.4	0.553	8.849	0.338	131	24
0.210	3.8	3.500	85.9	3.882	4.010	38.1	0.547	8.914	0.353	132	25
0.210	4.0	3.500	84.9	3.901	4.476	38.3	0.582	8.817	0.353	138	24
0.230	4.7	3.450	82.7	3.920	5.756	38.1	0.676	8.676	0.348	153	21
0.230	4.7	3.450	82.8	3.909	5.802	37.8	0.676	8.735	0.380	157	23
0.230	5.3	3.450	80.7	3.952	7.023	37.7	0.766	8.624	0.348	168	19
0.250	6.7	3.200	75.2	3.879	8.883	37.5	0.971	7.941	0.392	213	17
0.250	6.5	3.200	75.8	3.838	8.723	37.2	0.946	7.970	0.424	213	19
0.250	7.1	3.200	73.8	3.855	9.624	37.0	1.036	7.835	0.412	227	17

Table B.7: Experimental Data for Constant IMEP=4 and Varying HES Tests (SOI=-24)

DOI (ms)	Diesel (mg)	DOI H2 (ms)	HES (%)	IMEP (bar)	MPRR (bar/CAD)	η_{th} (%)	CO2exh (vol%)	H2int (vol%)	H2exh (vol%)	CO2eq Total(g/kWh)	H2 Slip Contribution (%)
0.170	3.7	3.500	86.1	3.949	1.608	39.2	0.530	8.855	0.273	120	21
0.170	3.5	3.500	86.8	3.907	1.461	38.9	0.503	8.881	0.260	115	21
0.170	3.5	3.500	86.7	3.903	1.461	38.8	0.504	8.891	0.268	116	22
0.190	3.4	3.550	87.3	3.912	1.441	38.5	0.488	9.039	0.244	110	21
0.190	3.3	3.550	87.7	3.903	1.427	38.5	0.471	9.073	0.244	108	21
0.190	3.2	3.550	87.8	3.867	1.423	38.2	0.468	9.062	0.246	108	22
0.210	3.5	3.500	86.8	3.867	1.443	38.5	0.501	8.889	0.251	115	21
0.210	3.4	3.500	87.0	3.862	1.429	38.5	0.493	8.887	0.268	115	22
0.210	3.4	3.500	87.1	3.850	1.429	38.4	0.490	8.894	0.271	115	22
0.230	4.1	3.450	84.5	3.997	2.292	39.5	0.591	8.718	0.315	133	22
0.230	3.9	3.450	85.1	3.943	1.875	39.2	0.567	8.718	0.318	131	23
0.230	4.0	3.450	85.0	3.943	1.859	39.1	0.572	8.726	0.318	132	23
0.250	6.3	3.200	76.6	3.940	6.146	38.3	0.909	8.035	0.371	197	18
0.250	6.3	3.200	76.5	3.965	6.470	38.6	0.912	8.005	0.363	195	17
0.250	6.3	3.200	76.4	3.957	6.428	38.6	0.916	7.997	0.376	197	18
0.280	10.3	2.850	63.4	3.980	11.952	36.9	1.500	6.977	0.439	304	13
0.280	10.1	2.850	63.3	3.845	12.237	36.6	1.465	6.782	0.490	313	15
0.280	11.1	2.850	61.2	3.981	12.951	36.6	1.603	6.781	0.478	326	14

Table B.8: Experimental Data for Constant IMEP=4 and Varying HES Tests (SOI=-34)

DOI (ms)	Diesel (mg)	DOI H2 (ms)	HES (%)	IMEP (bar)	MPRR (bar/CAD)	η_{th} (%)	CO2exh (vol%)	H2int (vol%)	H2exh (vol%)	CO2eq Total(g/kWh)	H2 Slip Contribution (%)
0.280	10.1	2.500	60.1	3.920	5.458	40.6	1.452	5.920	0.626	320	18
0.280	10.1	2.500	60.4	3.954	5.659	40.7	1.452	5.980	0.639	318	19
0.280	10.2	2.500	59.9	3.958	6.094	40.6	1.476	5.959	0.642	322	19
0.300	11.2	2.420	54.6	3.789	6.958	40.2	1.611	5.249	0.626	360	17
0.300	11.2	2.420	54.6	3.788	7.154	40.1	1.620	5.256	0.607	360	16
0.300	11.4	2.420	54.3	3.793	7.352	39.9	1.639	5.256	0.593	362	16
0.350	12.5	2.400	51.0	3.849	9.715	39.3	1.807	5.092	0.584	386	14
0.350	12.4	2.400	51.3	3.835	9.408	39.5	1.785	5.086	0.605	385	15
0.350	12.4	2.400	51.4	3.838	9.586	39.5	1.784	5.090	0.608	385	15

Table B.9: Experimental Data for Constant IMEP=6 and Varying HES Tests (SOI=-01)

DOI (ms)	Diesel (mg)	DOI H2 (ms)	HES (%)	IMEP (bar)	MPRR (bar/CAD)	η_{th} (%)	CO2exh (vol%)	H2int (vol%)	H2exh (vol%)	CO2eq Total(g/kWh)	H2 Slip Contribution (%)
0.250	7.5	4.750	81.9	5.739	2.783	36.0	1.095	13.301	0.140	142	6
0.250	7.3	4.750	82.5	5.714	2.538	36.0	1.056	13.339	0.097	135	5
0.250	7.5	4.750	82.1	5.754	2.497	36.1	1.083	13.347	0.074	136	3
0.280	11.6	4.450	73.2	5.975	5.334	36.1	1.682	12.336	0.144	206	4
0.280	11.5	4.450	73.4	5.959	4.637	36.1	1.664	12.368	0.090	201	3
0.280	11.4	4.450	73.6	5.967	4.324	36.1	1.655	12.380	0.097	200	3
0.300	12.4	4.350	71.1	5.910	5.887	36.1	1.794	11.870	0.147	222	4
0.300	12.3	4.350	71.2	5.890	4.722	36.1	1.780	11.857	0.084	217	2
0.300	12.6	4.350	70.7	5.969	4.900	36.3	1.825	11.864	0.107	221	3
0.370	14.7	4.150	65.6	5.917	7.121	36.3	2.122	10.897	0.150	261	4
0.370	14.5	4.150	65.9	5.918	5.220	36.5	2.093	10.877	0.091	254	2
0.370	14.5	4.150	65.9	5.925	5.243	36.6	2.092	10.881	0.118	255	3
0.500	24.5	2.700	40.0	5.951	11.044	38.1	3.529	6.371	0.200	430	3
0.500	23.7	2.700	40.8	5.837	9.751	38.1	3.413	6.367	0.196	425	3
0.500	24.4	2.700	41.4	5.972	9.798	37.6	3.506	6.707	0.201	426	3

B.3 Experimental Data for Maximum HES Testing

The test points for Section 4.6 are detailed in Table B.10.

Table B.10: Experimental Data for Minimum Pilot and Maximum HES Tests

IMEP (bar)	SOI (CAD)	DOI (ms)	Diesel (mg)	DOI H2 (ms)	η_{th} (%)	CO2 exh (vol%)	MPRR (bar/CAD)	H2int (vol%)	H2exh (vol%)	CO2eq of H2 Slip (g/kWh)
2.082	-4.0	0.170	4.1	2.570	27.5	0.592	1.437	6.106	1.356	239.659
2.307	-4.0	0.170	4.3	2.570	29.4	0.625	1.452	6.295	1.151	183.596
1.885	-4.0	0.170	4.0	2.570	26.1	0.572	1.424	5.803	1.581	308.636
1.997	-9.0	0.170	3.7	2.520	29.2	0.539	2.855	5.513	1.536	282.852
2.424	-9.0	0.170	4.0	2.520	33.0	0.576	3.095	5.940	1.085	164.684
2.066	-9.0	0.170	3.7	2.520	30.3	0.538	2.925	5.500	1.513	269.433
1.986	-14.0	0.170	3.7	2.480	30.8	0.534	3.506	5.124	1.383	256.309
2.253	-14.0	0.170	3.8	2.480	33.1	0.548	3.333	5.450	1.095	178.773
2.196	-14.0	0.170	3.8	2.480	33.2	0.544	3.546	5.279	1.211	202.892
1.939	-19.0	0.170	3.6	2.460	31.1	0.503	2.490	4.962	1.227	232.848
2.219	-19.0	0.170	3.8	2.460	33.8	0.535	2.411	5.232	1.008	167.067
2.239	-19.0	0.170	3.6	2.460	34.3	0.519	2.468	5.240	0.997	163.864
1.993	-24.0	0.170	3.2	2.500	31.1	0.434	1.470	5.284	1.263	233.264
2.325	-24.0	0.170	3.3	2.500	33.9	0.455	1.461	5.701	1.017	161.045
2.332	-24.0	0.170	3.3	2.500	34.5	0.455	1.467	5.606	1.001	157.924
2.070	-29.0	0.170	2.7	2.700	28.4	0.346	1.434	6.352	1.155	205.347
1.847	-29.0	0.170	2.4	2.700	25.6	0.292	1.431	6.405	1.383	275.591

2.078	-29.0	0.170	2.7	2.700	28.8	0.334	1.429	6.328	1.211	214.435
3.152	-4.0	0.170	4.6	3.000	35.0	0.674	1.552	7.358	0.495	57.739
3.094	-4.0	0.170	4.4	3.000	34.7	0.639	1.475	7.370	0.484	57.493
3.133	-4.0	0.170	4.5	3.000	35.2	0.651	1.508	7.335	0.496	58.284
3.098	-9.0	0.170	4.2	2.850	37.2	0.617	3.509	6.826	0.630	74.853
3.036	-9.0	0.170	3.9	2.850	37.0	0.572	3.051	6.836	0.652	78.977
3.064	-9.0	0.170	4.2	2.850	37.1	0.610	3.276	6.782	0.626	75.232
3.006	-14.0	0.170	4.1	2.770	37.8	0.590	3.830	6.514	0.641	78.465
2.952	-14.0	0.170	3.7	2.770	37.8	0.541	3.242	6.501	0.674	84.005
2.975	-14.0	0.170	3.8	2.770	38.0	0.558	3.296	6.489	0.651	80.545
2.932	-19.0	0.170	3.8	2.700	38.2	0.554	2.505	6.331	0.618	77.537
2.912	-19.0	0.170	3.6	2.700	38.4	0.524	2.290	6.321	0.638	80.559
2.882	-19.0	0.170	3.7	2.700	38.1	0.526	1.922	6.290	0.615	78.540
2.965	-24.0	0.170	3.5	2.800	37.9	0.490	1.453	6.607	0.641	79.503
2.981	-24.0	0.170	3.5	2.800	37.9	0.492	1.454	6.643	0.596	73.550
2.752	-24.0	0.170	3.2	2.800	35.8	0.437	1.444	6.588	0.694	92.829
3.979	-4.0	0.170	4.6	3.630	36.6	0.669	1.493	9.293	0.214	19.751
4.029	-4.0	0.170	4.5	3.630	36.9	0.658	1.471	9.375	0.196	17.928
4.017	-4.0	0.170	4.5	3.630	37.2	0.658	1.478	9.264	0.216	19.777
3.933	-9.0	0.170	4.2	3.480	38.6	0.611	3.548	8.742	0.308	28.831
3.986	-9.0	0.170	4.2	3.480	39.0	0.606	3.674	8.804	0.277	25.546
4.018	-9.0	0.170	4.3	3.480	39.3	0.626	3.725	8.743	0.300	27.514
3.900	-14.0	0.170	4.1	3.430	39.1	0.595	4.333	8.562	0.359	33.860
3.943	-14.0	0.170	4.1	3.430	39.3	0.595	4.387	8.644	0.343	32.035
3.979	-14.0	0.170	4.3	3.430	39.7	0.619	4.708	8.556	0.341	31.525
3.919	-19.0	0.170	3.9	3.400	39.9	0.570	3.512	8.497	0.368	34.528
3.933	-19.0	0.170	3.9	3.400	39.9	0.570	3.682	8.517	0.346	32.357
3.953	-19.0	0.170	4.0	3.400	40.4	0.578	3.681	8.430	0.348	32.358
3.972	-24.0	0.170	3.6	3.450	40.0	0.516	1.503	8.728	0.257	23.810

3.940	-24.0	0.170	3.6	3.450	39.9	0.517	1.490	8.667	0.263	24.520
3.947	-24.0	0.170	3.6	3.450	40.4	0.516	1.470	8.587	0.251	23.415
6.022	-4.0	0.170	4.5	4.900	38.7	0.657	6.924	14.102	0.124	7.547
6.006	-4.0	0.170	4.4	4.900	38.6	0.646	7.151	14.136	0.126	7.741
6.051	-4.0	0.170	4.5	4.900	39.3	0.658	7.291	13.944	0.090	5.496